DISSOLUTION OF FLUORIDE UPCONVERTING NANOPARTICLES IN AQUEOUS SUSPENSIONS AND THEIR PROTECTION WITH AMPHIPHILIC COATINGS

Olivija Plohl

Doctoral Dissertation
Jožef Stefan International Postgraduate School
Ljubljana, Slovenia

Supervisor: Assoc. Prof. Dr. Darja Lisjak, Jožef Stefan Institute, Ljubljana, Slovenia

Evaluation Board:
Prof. Dr. Darko Makovec, Chair, Jožef Stefan Institute, Ljubljana, Slovenia
Assoc. Prof. Dr. Maja Ponikvar-Svet, Member, Jožef Stefan Institute, Ljubljana, Slovenia
Prof. Dr. Boris Majaron, Member, Jožef Stefan Institute, Ljubljana, Slovenia

MEDNARODNA PODIPLOMSKA ŠOLA JOŽEFA STEFANA
JOŽEF STEFAN INTERNATIONAL POSTGRADUATE SCHOOL



Olivija Plohl

DISSOLUTION OF FLUORIDE UPCONVERTING NANOPARTICLES IN AQUEOUS SUSPENSIONS AND THEIR PROTECTION WITH AMPHIPHILIC COATINGS

Doctoral Dissertation

RAZTAPLJANJE FLUORIDNIH NANODELCEV Z ENERGIJSKO PRETVORBO NAVZGOR V VODNIH SUSPENZIJAH TER NJIHOVA ZAŠČITA Z AMFIFILNIMI PREVLEKAMI

Doktorska disertacija

Supervisor: Assoc. Prof. Dr. Darja Lisjak

Ljubljana, Slovenia, September 2016

To all my family and friends, especially to my dear Robert, who stood by my side and encouraged me to go my own way…

Acknowledgments

This work would not have been possible without the support of many people, who helped me over these years of the PhD period.

First I would like to thank Assoc. Prof. Dr. Darja Lisjak for her guidance, patience, support, and for numerous suggestions and scientific discussions, and most of all, for giving me the opportunity to work as a young researcher.

I would also like to acknowledge Prof. Dr. Darko Makovec for giving me precious advice and fruitful discussions.

Special thanks go to Prof. Dr. Boris Majaron for giving me the opportunity to work in the laboratory of the F7 department and allowing me to use the equipment for optical measurements. Moreover, thanks for all the discussions and advice regarding the optical part of my thesis.

I would also like to thank Assoc. Prof. Dr. Maja Ponikvar-Svet for the analyses of the fluoride ion, and for the kindness and useful discussions.

Thanks goes also to Prof. Dr. Janez Kovač for performing the XPS surface analyses and including their interpretation, and to Asst. Prof. Dr. Marjeta Maček Kržmanc for performing the TGA analyses.

My special thanks goes to all my co-workers at the Department for Materials Synthesis, especially to Bernarda Anželak for teaching me the laboratory skills and for the help during the experiments. Nevertheless, I would like to say that she is a wonderful person and I am happy to know her. I would also like to acknowledge Slavko Kralj for useful advices and discussions regarding the functionalization part, and to Sašo Gyergyek for scientific discussions. Thanks goes also to Blaž Belec for performing some TEM analyses, and to Tanja Goršak for useful advices in the laboratory.

Although she was my co-worker, she was also my special friend during these years. Therefore, special thanks goes to you, Klementina Pušnik, for being the person you are. I will never forget our conversations and your support during hard times.

Nevertheless, I would like to acknowledge Prof. Dr. Ute Resch-Genger and Marco Kraft for their guidance and very useful scientific discussions during my stay in Berlin.

In addition, very special persons in my life are my best friends. Alja, Tanja, Ana and Ajda, thanks for listening to me in hard times, for all the nice moments we spent together and for encouraging me to go further☺.

I am also taking this opportunity to express my gratitude to the Slovenian Research Agency for funding and to the CENN Nanocenter for enabling the use of research equipment. Also thanks to the project COST CM1403 that enabled my stay in Berlin.

Most importantly, I would like to thank my family, especially my mother, father, brother Tadej, sister Tjaša and my dearest grandmothers for their unconditional support over these years.

Last, but not least, I would like to express special gratitude to my boyfriend Robert, for all his love, support, for his patience during my PhD. Thanks for the long conversations, for encouraging me and for all the unforgettable moments that we spent together.

Abstract

The present work is a dissolution study of fluoride upconverting nanoparticles (UCNPs), all co-doped with Yb^{3+} and Tm^{3+}, in aqueous suspensions and their possible protection against the dissolution with amphiphilic coatings. The work is thematically divided into two parts. The first part comprises various parameters influencing the dissolution of fluoride UCNPs in aqueous systems, including the effect of the dissolution on the optical properties of UCNPs. In the second part, two potentially protective amphiphilic coatings were tested in order to prevent or minimize the dissolution of fluoride UCNPs in aqueous systems.

Binary fluoride UCNPs, based on LaF_3 and GdF_3, were synthesized hydrothermally and solvothermally. $NaYF_4$ UCNPs with a cubic crystal structure were synthesized hydrothermally, solvothermally and with coprecipitation. On the other hand, $NaYF_4$ UCNPs with a hexagonal crystal structure were synthesized in organic solvents with a modified thermal decomposition synthesis. All the studied UCNPs showed UC fluorescence emission, which is typical for Tm^{3+}. UCNPs were aged in weakly acidic water or in phosphate buffer saline (PBS) with pH of 7.4 at room temperature (RT), 37 °C and 50 °C. Their dissolution was analyzed from the fraction of dissolved fluoride ion, which was determined potenciometrically.

The dissolution degree of the UCNPs increased significantly with the increasing temperature and with the decreasing particle size. The influence of the crystal structure was evaluated by comparing $NaYF_4$ UCNPs with a cubic and hexagonal crystal structure. The difference in their dissolution was correlated to the different thermodynamic stabilities of their structures. Unexpectedly, the media composition also had a significant effect on the degree of dissolution. The UCNPs dissolved much more significantly in PBS than in the weakly acidic water. The high dissolution degree in the PBS was explained with the simultaneous formation of more stable and insoluble Ln-phosphate compounds. On the other hand, the dissolution in weakly acidic water was lower and attributed to the hydrolysis of the UCNPs' surfaces. It was also shown that polyvynilpyrrolidone (PVP), used as a stabilizing surface ligand, promoted the dissolution, while the silica coating slowed down the dissolution of UCNPs.

Optical properties between the unaged and aged UCNPs were compared. We observed variations in the intensity of the Tm^{3+} emission bands and in the Yb^{3+} lifetimes. At the same time the surface chemistry of UCNPs, which affects their optical properties, changed with aging.

Two amphiphilic coatings, i.e. poly(maleic anhydride-alt-1-octadecene), cross-linked with bis(hexamethylene)triamine (PMAO-BHMT), and D-α-Tocopheryl polyethylene glycol 1000 succinate (TPGS) were tested for their effectiveness against the dissolution of UCNPs. While the latter was not found suitable, the PMAO-BHMT coating showed some promising results. Finally, the potential cytotoxicity related to the dissolved fluoride and lanthanide ions and instability of optical properties due to the dissolution are discussed.

Povzetek

Predstavljeno delo je študija raztapljanja fluorescenčnih fluoridnih nanodelcev z energijsko pretvorbo navzgor, dopiranih z Yb^{3+} in Tm^{3+}, v vodnih suspenzijah. Za uporabo morebitne zaščite teh nanodelcev pred raztapljanjem v vodnih sistemih so bile testirane amfifilne prevleke. Pričujoče delo je tematsko razdeljeno na dva dela. Prvi del obsega vpliv različnih parametrov na raztapljanje teh nanodelcev v vodnih sistemih ter študijo učinka raztapljanja na optične lastnosti. V drugem delu sta bili testirani dve potencialno zaščitni amfifilni prevleki z namenom preprečitve oziroma zmanjšanja raztapljanja teh nanodelcev v vodnih suspenzijah.

Nanodelci binarnih fluoridov na osnovi LaF_3 in GdF_3 so bili sintetizirani hidrotermalno in solvotermalno. Nanodelci $NaYF_4$ s kubično kristalno strukturo so bili sintetizirani hidrotermalno, solvotermalno ter s soobarjanjem. Nanodelci $NaYF_4$ s heksagonalno kristalno strukturo pa so bili sintetizirani v organskih topilih z modificirano sintezo termičnega razklopa. Vsi študirani nanodelci fluoridov z energijsko pretvorbo navzgor so izkazovali fluorescenčno emisijo z energijsko pretvorbo navzgor (ang. upconversion), značilno za Tm^{3+}. Sintetizirani nanodelci fluoridov so bili starani v rahlo kislem vodnem mediju oziroma v fosfatnem pufru s pH = 7,4 pri sobni temperaturi, 37 °C in 50 °C. Stopnjo raztapljanja nanodelcev smo analizirali iz deleža raztopljenega fluoridnega iona. Slednji je bil določen s potenciometrično metodo.

Stopnja raztapljanja študiranih nanodelcev fluoridov se je bistveno povečevala z naraščajočo temperaturo in z manjšanjem velikosti nanodelcev. Vpliv kristalne strukture smo ocenili s primerjavo nanodelcev $NaYF_4$ s kubično in heksagonalno kristalno strukturo. Razliko v stopnji raztapljanja obeh kristalnih struktur smo povezali z njuno različno termodinamsko stabilnostjo. Nepričakovano je sestava medija pri staranju nanodelcev imela velik vpliv na stopnjo raztapljanja. Nanodelci fluorida so se bistveno bolj raztapljali v fosfatnem pufru kot v rahlo kislem vodnem mediju. Visoka stopnja raztapljanja v fosfatnem pufru je bila pojasnjena s hkratnim nastankom slabo topnih in bolj stabilnih lantanidno-fosfatnih spojin. Raztapljanje v rahlo kislem vodnem mediju pa je bilo pripisano hidrolizi površine nanodelcev. Pokazalo se je tudi, da se z uporabo površinskega liganda polivinilpirolidona (PVP) z namenom stabilizacije raztapljanje pospeši, medtem ko pa prevleka iz amorfnega silicijevega dioksida raztapljanje upočasni.

Primerjava optičnih lastnosti fluoridnih nanodelcev pred in po staranju je pokazala razliko med njimi. Ne le, da se opazi razlika v intenziteti emisijskih vrhov Tm^{3+}, temveč tudi v življenjskem času Yb^{3+}. Prav tako se je kemijska sestava površine spreminjala s staranjem, kar se je odražalo tudi v spremenjenih optičnih lastnostih po staranju.

Dve amfifilni prevleki na osnovi amfifilnega polimera poli anhidrida maleinske kisline-alt-1-oktadeken, zamreženega z bis heksametilentriamin (PMAO-BHMT), ter amfifilni polimer D-α-tokoferil polietilenglikol 1000 sukcinat (TPGS) sta bili testirani za omejitev raztapljanja nanodelcev. Amfifilna prevleka iz TPGS se je izkazala za neprimerno, medtem ko pa se je amfifilna prevleka PMAO-BHMT izkazala za učinkovito. Tezo zaključim z razpravo o morebitni citotoksičnosti, povezani z raztopljenimi fluoridnimi in lantanidnimi ioni, ter o vplivu raztapljanja na spreminjanje optičnih lastnosti.

Contents

List of Figures **xv**

List of Tables **xix**

Abbreviations **xxi**

Symbols **xxiii**

1 Introduction **1**
1.1 Upconverting Fluorescent Nanoparticles ... 1
1.1.1 Upconversion Process ... 2
1.1.2 Matrices and Dopants of the UCNPs ... 3
1.1.3 Effect of the Surface on the Optical Properties of UCNPs ... 4
1.1.4 Typical Synthesis Methods for UCNPs ... 4
1.1.4.1 Synthesis with Coprecipitation ... 4
1.1.4.2 Hydrothermal/Solvothermal Synthesis ... 5
1.1.4.3 Thermal Decomposition Synthesis ... 7
1.2 UCNPs in Biomedicine ... 9
1.2.1 Colloidal Stabilization in Aqueous Systems ... 9
1.2.2 Surface Functionalization of UCNPs ... 12
1.2.3 Amphiphilic Coatings ... 14
1.2.3.1 Amphiphilic Co-Polymer PMAO-BHMT ... 15
1.2.3.2 Amphiphilic Polymer TPGS ... 16
1.2.4 Biological Applications ... 16
1.3 Dissolution and Possible (Cyto)Toxicity of UCNPs ... 18
1.3.1 Dissolution of NPs ... 18
1.3.1.1 Dissolution of Ln-fluoride Compounds in Water ... 21
1.3.2 Effect of Dissolution on Possible (Cyto)Toxicity ... 21
1.3.2.1 General Toxicity of NPs ... 21
1.3.2.2 Adverse Effects of F^- ... 22
1.3.2.3 Adverse Effects of Ln^{3+} and (Cyto)Toxicity Studies of Ln-based NPs ... 23

2 Aims and Hypothesis **25**
2.1 Aims ... 25
2.2 Hypothesis ... 25

3 Materials and Methods **27**
3.1 Materials ... 27
3.2 Methods ... 27
3.2.1 Synthesis of UCNPs ... 27

3.2.2 Coating of NaY-TS UCNPs with Amphiphilic Polymers and Preparation of Their Stable Suspensions in Water 30
3.2.3 Dissolution Study 31
3.2.4 Characterization Techniques 32
3.2.4.1 UCNPs Characterization 32
3.2.4.2 Suspension Characterization 33
3.2.4.3 Optical Properties 33

4 Results **35**
4.1 Fluoride UCNPs and Their Dissolution in Aqueous Systems 35
4.1.1 Dissolution of Binary Fluoride UCNPs in Water 35
4.1.2 The Dissolution of $NaYF_4$ UCNPs in Water 39
4.1.3 Dissolution of $NaYF_4$ UCNPs at Simulated Physiological Conditions 44
4.1.3.1 α-$NaYF_4$ UCNPs 45
4.1.3.2 β-$NaYF_4$ UCNPs 51
4.1.3.3 Effect of the Dissolution of β-$NaYF_4$ UCNPs on their Optical Properties 52
4.2 Effects of Amphiphilic Coatings on the Dissolution of Fluoride UCNPs in Aqueous Systems 56
4.2.1 Formation of the PMAO-BHMT Coating 56
4.2.2 Formation of the TPGS Coating 60
4.2.3 Dissolution Study 63

5 Discussion **65**
5.1 Dissolution of Fluoride UCNPs in Aqueous Media 65
5.2 Effect of Amphiphilic Coatings on the Dissolution of β-$NaYF_4$ UCNPs in Aqueous Media 71
5.3 Effect of the Dissolution of UCNPs on the Potential Use in Biomedicine 72

6 Conclusions **75**

References **77**

Bibliography **91**

Biography **93**

List of Figures

Figure 1.1: UC processes in Tm^{3+} and Yb^{3+} co-doped UCNPs. 2

Figure 1.2:Schematic presentation of α-$NaYF_4$ (a) and β-$NaYF_4$ (b) structures. Modified from [11]. 3

Figure 1.3: (a) TEM images of the transformation of α-$NaYF_4$ UCNPs into β-$NaYF_4$ UCNPs as a function of the reaction time under hydrothermal conditions: (A) 0h, (B) 6h, (C) 12 h and (D) 24 h. (b) Schematic representation of possible formation mechanism of β- $NaYF_4$ microparticles [43]. 7

Figure 1.4: (a) Diagrams illustrating the correlation between the evolution of UC intensity and temperature as a function of reaction time with four reaction stages, which are schematically presented in (b) together with a high-resolution TEM images of the evolving UCNPs. Modified from [53]. 8

Figure 1.5:Different synthetic pathways to achieve biomedically applicable NPs. Modified from [58]. 9

Figure 1.6: Schematic presentation of electrostatic (a) and steric stabilization (b) [61]. ...9

Figure 1.7: Schematic presentation of an electrostatic double layer (a) and the decay of surface potential with the distance from the surface (b) [59]....11

Figure 1.8: Schematic presentation of total interaction energy versus distance between two particles. Modified from [60]. 12

Figure 1.9: Illustrative presentation of different strategies for functionalization [31].....13

Figure 1.10:Schematic illustration of the formation of the silica coating via PVP onto $NaYF_4$: Yb^{3+},Er^{3+}@PVP UCNPs. Modified from [31]. 14

Figure 1.11:Scheme of amphiphilic polymer. 14

Figure 1.12:Illustration of cross-linked co-polymers stabilized-UCNPs. Modified from [19]. 15

Figure 1.13:Chemical structure of TPGS [77]....16

Figure 1.14:Simplified representation of the dissolution process....18

Figure 1.15:The solubility of a surface with positive curvature ($r > 0$) exceeds the solubility of a flat surface ($r = \infty$) and, even more, of a surface with negative curvature ($r < 0$). After [110]....19

Figure 1.16:Simplified illustration of NPs interactions with a cell, resulting in various damage effects [127]. 22

Figure 3.1: Schematic presentation of synthesis of NaY-R and NaY-R@PVP UCNPs followed by coating with silica. 30

Figure 3.2: Schematic presentation of the coating process. 31

Figure 4.1: XRD patterns of the as-synthesized binary fluoride UCNPs. 36

Figure 4.2: TEM images of La-HS (a), La-SS (b), Gd-HS (c) and Gd-SS (d) UCNPs. ...38

Figure 4.3: UC spectra of La-HS UCNPs suspension in water with c = 13.6 mg/ml..... 38
Figure 4.4: XRD patterns of the as-synthesized UCNPs. 40
Figure 4.5: TEM images of the as-synthesized UCNPs [155]. 42
Figure 4.6: SEM image of NaY-HS-20 UCNPs [155]. 42
Figure 4.7: UC emission spectra of UCNPs in aqueous suspensions. 43
Figure 4.8:NaY-HS-1 and NaY-TS UCNPs with their respective surface composition given in at.%..... 44
Figure 4.9: XRD patterns of NaY-R UCNPs. 45
Figure 4.10:TEM image of the as-synthesized NaY-R UCNPs (a) with particle-size distribution (b), where red line represents a Gauss fit of relative frequency..... 46
Figure 4.11:TEM images of NaY-R@SiO_2 UCNPs at lower (a) and higher magnification (b). 46
Figure 4.12:Zeta potential values versus pH for NaY-R, NaY-R@PVP and NaY-R@SiO_2 UCNPs dispersed in water. 47
Figure 4.13:UC emission spectra of NaY-R UCNPs (c = 1 mg/ml) in water. 48
Figure 4.14:NaY-R UCNPs with their respective surface composition given in at.%. 49
Figure 4.15:Dissolution of NaY-R, NaY-R@PVP and NaY-R@SiO_2 UCNPs..... 50
Figure 4.16:Dissolution of NaY-R, NaY-R@PVP, NaY-R@SiO_2 UCNPs at shorter aging times. 50
Figure 4.17:TEM image of the as-synthesized NaY-TS-B UCNPs (a) and particle size distribution (b)..... 51
Figure 4.18:UC emission spectra (a) with normalized emission intensities (b) of unaged and aged NaY-TS samples A and B..... 53
Figure 4.19:Emission intensity of Yb^{3+} lifetimes for unaged and aged NaY-TS samples. 54
Figure 4.20:XPS survey spectra of the unaged and aged NaY-TS-XPS UCNPs (a) with respective atomic fractions (b). The relative error in concentration in (b) was estimated to be about 20 %. The normalized surface compositions with respect to Y are compared in (c). 55
Figure 4.21:Schematic representation of cross-linking of PMAO with BHMT (a,b). (b) was modified from [19]. 56
Figure 4.22:ATR-FTIR spectra of PMAO, BHMT and NaY-TS@PMAO-BHMT UCNPs. 57
Figure 4.23:Zeta potential versus pH of NaY-TS and NaY-TS@PMAO-BHMT UCNPs in water. 58
Figure 4.24:Number-weighted distribution of the hydrodynamic diameter of NaY-TS@PMAO-BHMT UCNPs in water (a) and the size of NaY-TS UCNPs (b)..... 58
Figure 4.25:TGA (red line) and DTA (blue line) curves of the PMAO-BHMT-coated NaY-TS-1 UCNPs. For the comparison the TGA curve (black line) of bare NaY-TS-1 UCNPs in also included. 59
Figure 4.26:Comparison of emission intensities of bare NaY-TS-1 and coated NaY-TS-1@PMAO-BHMT UCNPs in aqueous suspension. 60
Figure 4.27:ATR-FTIR curves before and after the coating of UCNPs with TPGS..... 61
Figure 4.28:Zeta potential versus pH of NaY-TS UCNPs and NaY-TS@TPGS UCNPs in water. 61

Figure 4.29:TGA (red line) and DTA (blue line) curves of the TPGS-coated NaY-TS-2 UCNPs. For the comparison the TGA curve (black line) of bare UCNPs is also included. 62

Figure 4.30:UC emission spectra of the bare NaY-TS-2 UCNPs and coated NaY-TS-2@TPGS (28 nm). 63

Figure 4.31:Amorphous side product after the aging of NaY-TS@TPGS UCNPs in PBS (a), with the corresponding EDXS spectrum (b), and few remaining UCNPs after the aging (c). The UC emission spectra of the unaged and aged TPGS-coated UCNPs are shown in (d).....64

Figure 5.1: Fraction of dissolved F^- versus β-$NaYF_4$ (NaY-TS) UCNPs' size, aged in PBS at pH = 7.4 for 2 days at 37 °C. The dotted line represents an exponential fit. 67

Figure 5.2:Fraction of dissolved F^- of α-$NaYF_4$ (NaY-R) UCNPs, aged in PBS for 2 days at pH = 7.4, versus aging temperature. The dotted red line represents an exponential fit. 68

Figure 5.3: TEM image of a solid side product from the aged NaY-TS-XPS sample (a) with the corresponding EDXS spectrum (b). Y-L and P-K overlap (at around 2 keV), which can be seen in an inset in (c). Additional Y-K peaks at around 15 and 17 keV confirm the presence of Y, while the presence of Yb is confirmed by the Yb-M and Yb-L peaks. The Cu and C peaks originate from the TEM supporting grid. 69

List of Tables

Table 1.1: Calculated dissolution half-time $t_{1/2}$ for some NPs [105]. 20
Table 1.2: K_{sp} values for some Ln-fluorides powders in water at 25 °C [121]. 21
Table 1.3: Some cytotoxicity effects associated to F^- exposure [128]. 23
Table 1.4: Some cytotoxicity studies of different UCNPs [126]. 24
Table 3.1: Synthesis parameters for binary fluoride UCNPs. 28
Table 3.2: Synthesis parameters for ternary fluoride UCNPs. 29
Table 3.3:Parameters of the dissolution study. RT denotes room temperature (20–25 °C). 32
Table 4.1: Structural and morphological properties of binary fluoride UCNPs and the pH values of the aged suspensions with the fraction of dissolved F^-. 36
Table 4.2: Crystal cell parameters for undoped NPs and doped UCNPs. 37
Table 4.3: Structural and morphological properties of fluoride UCNPs, and pH values of the aged suspensions with the fraction of dissolved ions [155]. 41
Table 4.4: Particle size, aging temperature and the fraction of dissolved F^- of NaY-TS and NaY-R UCNPs. All samples were aged for two days in PBS at pH = 7.4. 52
Table 4.5: Fraction of the dissolved F^- from the bare and coated NaY-TS UCNPs after the aging for two days in PBS at pH = 7.4 and T = 37 °C. 64
Table 5.1: Summary of UCNPs and their dissolution study. Note that binary fluoride UCNPs were excluded from the discussion. 66

Abbreviations

APS ... aminopropyltriethoxysilane
ATP ... adenine-tri-phosphate
ATR ... attenuated total reflectance
BHMT ... bis(hexamethylene)triamine
CT ... computed tomography
CT CAs ... computed tomography contrast agents
CTAB ... cetyltrimethylammonium bromide
DC ... downconversion
DE ... diethyl ether
DLS ... dynamic light scattering
DLVO ... theory of suspension stability by Derjaguin, Landau, Verwey and Overbeek
DNA ... deoxyribonucleic acid
EDTA ... ethylendiaminetetraacetic acid
EDXS ... energy dispersive X-ray spectroscopy
EG ... ethylene glycol
ESA ... excited state absorption
ETU ... energy transfer upconversion
FA ... folic acid
FRET ... Förster Resonance Energy Transfer
HS ... hydrothermal synthesis
IBU ... ibuprofen
ICP-OES ... optical emission spectrometer with inductively coupled plasma
IEP ... isoelectric point
ISE ... ion selective electrode
Ln^{3+} ... lanthanide ions
MRI ... magnetic resonance imaging
mRNA ... messenger of ribonucleic acid
NAD^+ ... oxidized form of nikotinamide adenine dinucleotide
NADH ... reduced form of nicotinamide adenine dinucleotide
NaY ... sodium yttrium fluoride
NIR ... near-infrared
OA ... oleic acid
ODE ... octadecene
OM ... oleylamin
PA ... photon avalanche
PAA ... poly(acrylic) acid
PBS ... phosphate buffer saline
PDT ... photodynamic therapy
PEG ... poly(ethylene glycol)
PEI ... polyethyleneimine
PMAO ... poly(maleic anhydride-alt-1-octadecene)

PTT ... photothermal therapy
PVP ... polyvinylpirrolidone
R ... reflux
RNA ... ribonucleic acid
ROS ... reactive oxygen species
RT ... room temperature
SAED ... selected area electron diffraction
SDS ... sodium dodecyl sulfate
SEM ... scanning electron microscope
SS ... solvothermal synthesis
TEM ... transmission electron microscope
TEOS ... tetraethoxysilane
TGA ... thermogravimetric analysis
TPGS ... D-α-tocopheryl polyethylene glycol succinate
TS ... thermal decomposition synthesis
UC ... upconversion
UCNPs ... upconverting nanoparticles
US FDA ... food and drug administration
UV ... ultraviolet
XPS ... X-ray photoelectron spectroscopy
XRD ... X-ray diffraction

Symbols

$1/\kappa$	...	thickness of the diffuse double layer (Debye length)
c	...	concentration
c_L	...	precursor concentration in suspension
c_S	...	solubility of the solid phase
d	...	diameter of the particle
ε	...	solvent permittivity
γ	...	surface tension
h	...	minimum separation between the particle surface
κ	...	inverse Debye length
k	...	the slope of the linear fit
k_{dis}	...	dissolution rate constant
K_{sp}	...	solubility product constant
M	...	concentration of dissolved ions
r	...	radius of the particle
s	...	solubility
S	...	supersaturation
s_0	...	equilibrium solubility
T	...	temperature
T_1	...	temperature of dissolution zone
$t_{1/2}$	...	half-times of dissolution
T_2	...	temperature of the growth zone
V	...	volume
V_A	...	potential energy of attractive forces
V_m	...	molar volume
V_R	...	repulsive, electrostatic potential energy
V_T	...	total energy of interaction
z	...	distance from the particles' surface to the surface of the shear
α-$NaYF_4$	...	cubic crystal modification of $NaYF_4$
β-$NaYF_4$	...	hexagonal crystal modification of $NaYF_4$
ΔT	...	temperature gradient between the dissolution and growth zones
ζ	...	zeta potential
$\lambda_{CuK\alpha 1}$	...	X-ray wavelength radiation
ψ_0	...	surface potential
ψ_d	...	the Stern potential

Chapter 1

Introduction

1.1 Upconverting Fluorescent Nanoparticles

There is a growing interest for the development of fast, cheap, sensitive and multiplexed techniques that enable analysis of biocomponents in a single step. Most of these options are based on bioimaging using biolabels [1], [2].

Inorganic lanthanide (Ln^{3+}) doped upconverting nanoparticles (UCNPs) have been recognized as promising fluorescent biolabels. Ln^{3+} are known to exhibit not only downconversion (DC) fluorescence (i.e., conventional Stokes type), but also efficient upconversion (UC) (i.e., antiStokes type) fluorescence. The term UC denotes the effect, where a low energy (e.g., near-infrared (NIR) excitation) is converted to a higher energy (e.g., visible or NIR emission) light. The phenomenon was first exploited when the laser emission from Nd^{3+}-doped $Y_3Al_5O_{12}$ (YAG) was discovered and applied in optical devices in 1960s. A potential usage of the UCNPs for bioanalytical assays and fluorescent imaging was recognized in the late 1990s, when the research of NPs intensified [2], [3].

Although conventional biolabels demonstrate useful features in bioimaging, they also have some disadvantages. Most of them have to be excited by ultraviolet light (UV), which can be potentially harmful, while the absorption and strong scattering in tissue and/or by biomolecules is limiting the penetration depth of this excitation light. Most of the organic fluorescent molecules have broad absorption and emission spectra that overlap between each other. Therefore they are difficult to be distinguished between each other [2].

Ln-doped UCNPs are a promising alternative to conventional biolabels. UCNPs have an advantage of being photoexcitable in the NIR. The absorption of any biological matter in the NIR is weak, therefore background absorption and fluorescence are reduced. The large anti-Stokes shift enables easier separation of the emission peaks from the excitation source, moreover emission bands are narrow. UCNPs supposed to be chemically stable, they do not bleach or blink. The emission wavelengths of the UCNPs are not dependent on the UCNPs size (like in the case of quantum dots and surface plasmonics, i.e., Au NPs) and emission with different colours can be achieved by varying the host crystal and Ln^{3+} dopants [2]. Particular interest is dedicated to UCNPs with both NIR excitation and NIR emission, specifically to the biological transmission window (700–1000 nm), because of deeper tissue penetration depth and diminished light scattering for *in vivo* imaging [4].

1.1.1 Upconversion Process

Fluorescent emission is typically a DC process, where higher energy photons are absorbed while lower energy photons are emitted. In contrast to this, the UC is a process that results in the emission of higher energy photons through a sequential absorption of lower energy photons. The UC process is described by three mechanisms, i.e., excited state absorption (ESA), energy transfer upconversion (ETU), and photon avalanche (PA). ETU, as the UC mechanism with the highest quantum yield, has been widely studied [5]. The ETU mechanism is, usually, the most efficient in Ln-doped UCNPs, with Yb^{3+} ion as a sensitizer, from which the absorbed energy is transferred to emitting ions, Tm^{3+}, Er^{3+} or Ho^{3+} [6].

An example of the UC process in the Yb^{3+} and Tm^{3+} co-doped UCNPs is schematically shown in Figure 1.1. The first step is the absorption of NIR photons by Yb^{3+} ions, exciting it from the $^2F_{7/2}$ ground state to the $^2F_{5/2}$ excited state. This is followed by energy transfer from the excited Yb^{3+} ion to Tm^{3+} in the close proximity, exciting Tm^{3+} from the $^3H_6$ ground state to the $^3H_5$ state (denoted as 1 in Figure 1.1). The following relaxation of Tm^{3+} to $^3F_4$ is a non-radiative process (denoted with green dotted arrow in Figure 1.1). Another energy transfer process from Yb^{3+} ion excites the Tm^{3+} ion from the $^3F_4$ state to the $^3F_2$ state (denoted as 2 in Figure 1.1). The $^3F_2$ excited state non-radiatively decays to the $^3H_4$ state. One of the energy transfer process from Yb^{3+} to Tm^{3+} then excites Tm^{3+} ion to $^1G_4$ (denoted as 3 in Figure 1.1) and another energy transfer from Yb^{3+} to Tm^{3+} excites Tm^{3+} to $^1D_4$ state (denoted as 4 in Figure 1.1). The following relaxation from the $^1D_2$ state to $^3F_4$ state and from the $^1G_4$ state to the Tm^{3+} ground state both result in a blue emission, at 450 and 475 nm, respectively (blue arrows in Figure 1.1). The relaxation of Tm^{3+} from $^1G_4$ to the $^3F_4$ state results in red emission (red arrow in Figure 1.1). Direct relaxation from the intermediate state $^3F_3$ to the ground state results in emission at 700 nm (yellow arrow in Figure 1.1) while the relaxation from the $^3H_4$ state to the ground state $^3H_6$ results in NIR emission at 800 nm (violet arrow in Figure 1.1).

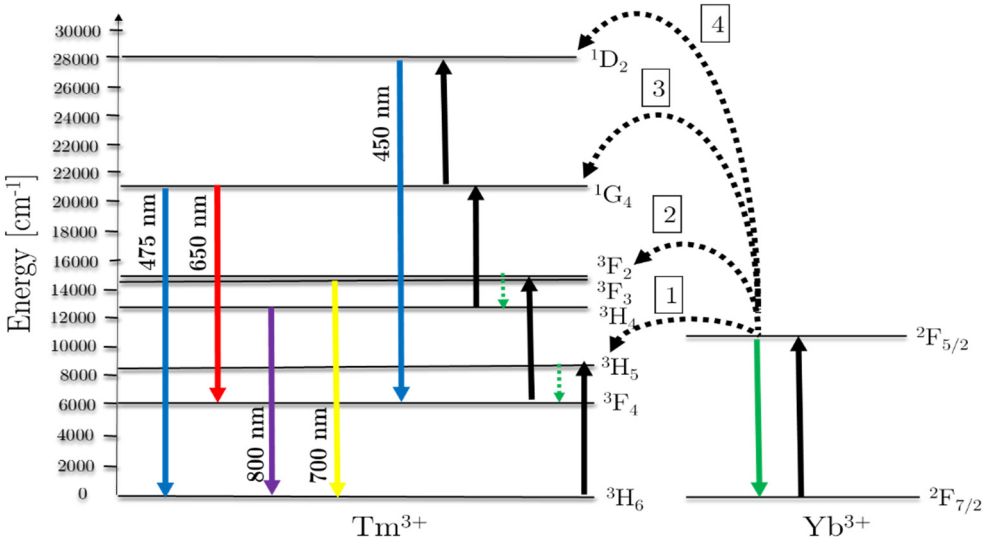


Figure 1.1: UC processes in Tm^{3+} and Yb^{3+} co-doped UCNPs. Modified from [7]. Solid black arrow represents photon absorption while solid coloured arrows represent emission. The black dotted arows represent the non-radiative energy transfer while green dotted arrows represents non-radiative relaxation processes. The green arrow represents multiphoton relaxation of Yb^{3+}.

1.1.2 Matrices and Dopants of the UCNPs

Ln-doped UCNPs are composed of three components: a host matrix, absorber (i.e., sensitizer) and emitter (i.e., activator). The latter two are dopants and are incorporated into inorganic crystalline host matrix in the form of localized fluorescent centers [4].

The selection of an appropriate host matrix is essential. General requirements for host matrices are close lattice matches to dopant ions, low phonon energy and chemical stability. All Ln^{3+} ions exhibit similar ionic size and chemical properties thus their inorganic compounds represent suitable host matrices. Low lattice phonon energy minimizes non-radiative losses and maximizes the emission. Chlorides, bromides and iodides generally exhibit low phonon energy (< 300 cm^{-1}), but they are very hygroscopic. Similarly, fluorides exhibit low phonon energies (~ 350 cm^{-1}) while they are chemically stable. Therefore they are often used as host matrices for the UC process [8]. One of the most often used fluoride matrices for the UC process is $NaYF_4$. It crystallizes in two modifications: cubic (α-$NaYF_4$) and hexagonal (β-$NaYF_4$) (Figure 1.2). Non-radiative relaxations in $NaYF_4$ are supressed and due to the lower crystal symmetry and consequently different lattice sites for emitter ions, the efficiency of β-$NaYF_4$ phase is about several magnitudes more intense than the efficiency of the α-$NaYF_4$ [2], [9]. Furthermore, the denser β-structure allows for more efficient energy transfer between the Ln^{3+} ions, and typically the β-phase crystallizes with an (almost) perfect structure, with lower fraction of crystalline defects in comparison to the α-phase [10].

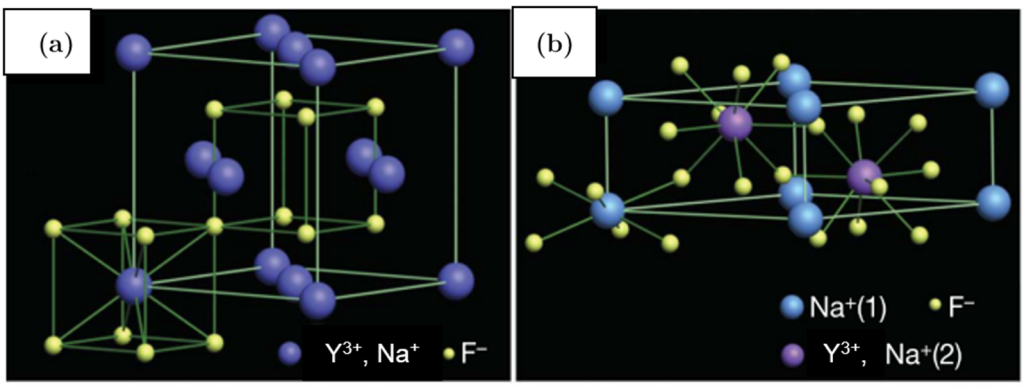


Figure 1.2: Schematic presentation of α-$NaYF_4$ (a) and β-$NaYF_4$ (b) structures. Modified from [11].

Yb^{3+} is used as an absorber in the UC process due to its simple energy diagram with only one excited 4f level, $^2F_{5/2}$ (Figure 1.1). Absorption band of Yb^{3+} is located around 980 nm and has a larger cross-section than any other Ln^{3+} ions. The transition $^2F_{7/2} \rightarrow {}^2F_{5/2}$ in Yb^{3+} is resonant with specific f-f transitions of Ln^{3+} ions (i.e., Er^{3+}, Tm^{3+}, Ho^{3+}), which enables efficient energy transfer from Yb^{3+} to the emitter. In order to enable the UC process the absorber content is kept high (~ 20 mol.%), while the emitter content is relatively low (< 2 mol.%) [8].

UC process requires multiple metastable levels and Ln^{3+} ions are well-suited for this process. Ln ions mostly exist in trivalent state (Ln^{3+}) since this is their most stable oxidation state. The 4f electrons of Ln^{3+} are shielded by the filled $5s^2$ and $5p^6$ shells. This results in weak electron-photon coupling that is responsible for sharp f-f absorption/emission bands. One of the important factors that determine the efficiency of the UC process is the population of the intermediate and emitting levels i.e. non-radiative multiphonon relaxation rate. The multiphonon relaxation rate decreases exponentially with

increasing the energy gap. High doping levels of emitter ions can lead to cross-relaxation, further resulting in quenching of excitation energy. Thus the concentration of emitter ions should be kept low and precisely adjusted to avoid the quenching effect [8]. Er^{3+}, Ho^{3+} and Tm^{3+} have large energy gaps and thus low probability of non-radiative transitions and are therefore known as the most efficient emitters in visible or NIR range. Co-doping of suitable matrices with Yb^{3+} and Tm^{3+} results in NIR-to-NIR UC process.

1.1.3 Effect of the Surface on the Optical Properties of UCNPs

The UC fluorescence efficiency is known to be size dependent. Due to increased surface- to- volume ratio there is a larger number of Ln^{3+} ions on the surface of UCNPs than on the surface of coarse-grained material. The major reason for the decrease of Ln^{3+} lifetimes in UCNPs is because of the large surface with a high concentration of crystalline defects, which also leads to stronger surface quenching effects in UCNPs, which further results in lower UC emission intensity [12], [13], [14]. The reduced UC emission efficiency in the UCNPs was also explained with high energy vibrations of the surface ligands or from the solvent [7], [15]. When UCNPs are dispersed in water, OH^- groups (3200–3600 cm^{-1}) absorb the excitation energy, which results in the decreased Yb^{3+} lifetime and, consequently, in the decreased UC fluorescence efficiency [7]. Namely, the absorptivity of the water at 980 nm is 0.485 cm^{-1} [16]. For example, the transmission of excitation light through 1-cm thick water layer is 62 %, which significantly attenuates the excitation light and decreases the UC emission efficiency [7], [16]. In general, functional groups like OH^-, NH and CH are known quenchers of Ln^{3+} ions [17]. Other surface ligands can also affect the UC fluorescence efficiency [15], [18]–[20].

One of the possibilities to enhance fluorescence efficiency of UCNPs is using a core-shell structure. The shell of material with a similar crystal lattice as the core is grown around the core. The shell can be undoped or differently doped than the core [21]–[27]. In this way the shell protects the dopant ions, especially those near the surface of the core, against the quenching effect. For example, core $NaGdF_4$:Yb^{3+},Er^{3+} UCNPs coated with a shell of $NaGdF_4$ showed a more intense fluorescence efficiency (for a factor of approximately 13 and 20 for the green and red emission, respectively) than the uncoated UCNPs [24]. Another way to enhance the UC emission is co-doping the UCNPs with passive or active impurities. Passive impurities do not participate in energy transfer of the UC process, but they cause distortions around the activator or can dilute the Ln clusters in the UCNPs. This can consequently lead to superior UC efficiency, which can also be increased by optimizing the impurity concentrations [2].

1.1.4 Typical Synthesis Methods for UCNPs

Different chemical synthesis methods, including coprecipitation, thermal decomposition, hydrothermal/solvothermal, sol-gel and combustion synthesis, are suitable for the synthesis of Ln-doped UCNPs [28]. Here we introduce only synthesis methods, which were used in this study.

1.1.4.1 Synthesis with Coprecipitation

Precipitation is a process, where particles precipitate from the solution when critical supersaturation is reached due to chemical reactions or other changes that may influence the solubility of the product. Coprecipitation is referred to the simultaneous precipitation of more than one ion (e.g., Y^{3+} and Yb^{3+}). Supersaturation (S), the driving force for the precipitation, is described as a ratio between precursor concentration in suspension c_L and the solubility of the solid phase c_S [29], [30]:

$$S = {}^{c_L}/_{c_S} \tag{1.1}$$

New particles formation with precipitation includes 4 kinetic stages:

1. formation of the zero-charge precursor,
2. nucleation,
3. growth,
4. aging.

The formation of a zero-charge precursor followed by condensation results in the nucleation of a new solid. Nuclei are formed when critical size is reached with homogeneous or heterogeneous nucleation. The main difference between both is that during the homogeneous nucleation three-dimensional nuclei are formed, on the other hand, during the heterogeneous nucleation two dimensional nuclei are formed on the surface of foreign phases. Because the surface energy in solid-solid system is smaller in comparison to the solid-liquid system, heterogeneous nucleation occurs more easily. After nucleation, nuclei grow with the addition of precursors that are still being formed after the nucleation. Growth of nuclei and later of particles can be described as a sequence of five processes: 1) transport of precursor molecules through the solution, 2) adsorption at the solid/solution interface, 3) surface diffusion, 4) reactions at the interface and 5) incorporation of the products into the crystal lattice. Growth of new particles can be limited by the diffusion of the precursor molecules towards the surface of nuclei or with surface reaction (incorporation of the precursor on the surface of the nuclei and a new nucleation). The last stage in the particle formation is aging and this step determines the characteristics of the particles. The aging stage enables the system to reach its thermodynamic stability with increasing the particle's size, changes of their morphology and crystal modification. The latter occurs for allotropes, where the least stable and, at the same time, the most soluble phase usually precipitates first. Because of the high solubility and metastable nature this phase recrystallizes during the aging into a more stable phase, mainly through heterogeneous nucleation [29], [30].

Coprecipitation synthesis is simple, not time consuming, does not require expensive setup [5], [31]. UCNPs can be synthesized with coprecipitation from aqueous solutions [32], [33] or from non-aqueous solutions [34], [35]. UCNPs growth can be controlled with the addition of capping ligands, such as polyvinylpyrrolidone (PVP) [35] and ethylendiaminetetraacetic acid (EDTA) [33], which are added into the reaction mixture. Coprecipitation in the case of $NaYF_4$ UCNPs typically yields α-$NaYF_4$ UCNPs [33], [35]. As opposed to β-$NaYF_4$ UCNPs, α-$NaYF_4$ UCNPs are metastable and more soluble at room temperature. They also exhibit inferior efficiency of the UC emission than β-$NaYF_4$ UCNPs. Therefore, the annealing at higher temperatures is required for a phase transformation into β-$NaYF_4$ UCNPs [33]. However, annealing causes aggregation and growth of the UCNPs. Moreover, capping ligands decompose during the annealing and further surface functionalization is required. Hence, the use of these UCNPs synthesized by coprecipitation synthesis in bioapplications is limited [31].

1.1.4.2 Hydrothermal/Solvothermal Synthesis

Hydrothermal synthesis (HS) refers to synthesis of substances at elevated temperature and pressure in aqueous solutions in a high-pressure autoclave. When another solvent is used instead of water we talk about solvothermal synthesis (SS). Reaction medium under these conditions has special properties. For example, the density, viscosity and surface tension of the water are low, but on the other hand, the vapour pressure and ion product are higher

[36], [37]. Most hydrothermal crystal growth is carried under temperature gradient and can be carried out in two ways [37]:

- Recrystallization of the solid substance that includes its dissolution in the liquid phase and then transfer of the dissolved part of the substance to the growth zone,
- dissolution of a mixture of the components' nutrient, convective mass transport into the growth zone and then reaction between the dissolved components.

In hydrothermal synthesis supersaturation is determined by the temperature gradient (ΔT) between the dissolution (T_1) and growth zones (T_2) and $T_1 > T_2$. If the solubility changes linearly with the temperature, the growth rate is also linear [37]. The crystallization of a new compound starts with nucleation, which is followed by a crystal growth. Both processes are temperature dependent. When the viscosity of the aqueous solution is low, nucleation and growth will be large. However, when temperature decreases, viscosity of the aqueous solution will decrease and stop the crystal growth [37], [38].

Facile and environmentally friendly HS was used for the synthesis of fluoride UCNPs with different crystal structures and morphologies [39]–[42]. Surface ligands, which can also be used during hydrothermal synthesis, affect the morphology and, to some degree, on the formation mechanism of the products [39], [43], [44]. A mechanism of transformation of α- $NaYF_4$ to β-$NaYF_4$ UCNPs and their morphology evolution under hydrothermal conditions has been the subject of some papers [44], [43], [45]. The mechanism was proposed as follows: when reaction temperature is reached, the reaction starts with a slow release of Ln^{3+} reagents into the solution. Afterwards, Na^+ and F^- react with the Ln^{3+} and a large number of $NaYF_4$ nuclei are formed. $NaYF_4$ nuclei aggregate and crystallize as α-$NaYF_4$ in a short time. However, α-$NaYF_4$ crystals are unstable and transform into β-$NaYF_4$ crystals through dissolution and renucleation during long reaction times and high enough temperatures (Figure 1.3) [43]. Consequently, only microparticles of β-$NaYF_4$ can be synthesized hydrothermally.

Several groups used solvothermal synthesis for the synthesis of UCNPs [46]–[48]. Typical solvothermal synthesis includes mixing fluoride precursors with Ln salts in a solvent with high boiling point, such as ethylene glycol (EG) [8]. Also in this case, β-$NaYF_4$ form only as microparticles.

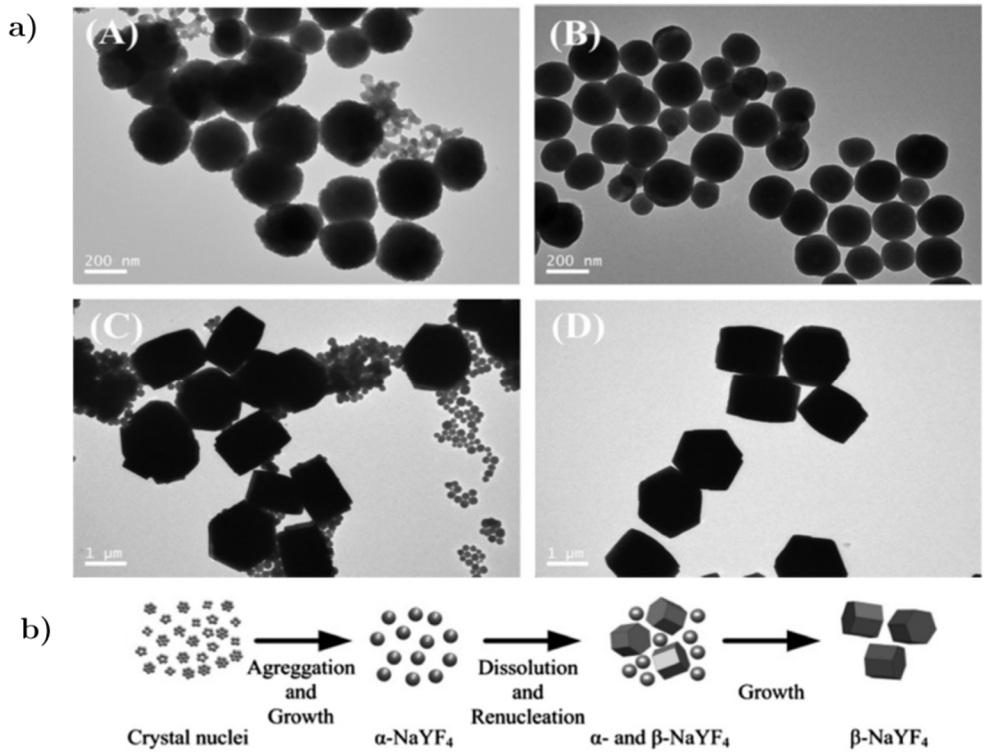


Figure 1.3: (a) TEM images of the transformation of α-$NaYF_4$ UCNPs into β-$NaYF_4$ UCNPs as a function of the reaction time under hydrothermal conditions: (A) 0h, (B) 6h, (C) 12 h and (D) 24 h. (b) Schematic representation of possible formation mechanism of β- $NaYF_4$ microparticles [43].

1.1.4.3 Thermal Decomposition Synthesis

Thermal decomposition is a waterless and oxygen-free process that involves dissolution of reactants in a high-boiling solvent, e.g., octadecene (ODE), in the presence of a stabilizing agent, e.g., oleic acid (OA) and decomposition of these reactants takes place at high temperatures, ≥ 300 °C [1]. First report on thermal decomposition synthesis of UCNPs was related to binary LaF_3 UCNPs [49]. In 2006 Boyer and Capobianco with co-workers [50] reported the synthesis of α-$NaYF_4$ UCNPs co-doped with Yb^{3+},Er^{3+} or Yb^{3+},Tm^{3+} via the thermal decomposition of metallic trifluoroacetates in ODE in the presence of OA. In the same year, Mai *et al.* published an article about thermal decomposition synthesis of high quality β-$NaLnF_4$ UCNPs, including β-$NaYF_4$ UCNPs in OA/Oleylamin(OM)/ODE system [51]. The latter process has been modified and the report of synthesis of β- $NaYF_4$ in OA/ODE was by Lie *et al.* [52]. Nowadays, a modified thermal decomposition synthesis (no generic name for this synthesis has been established) with decomposition of Ln-oleates [53], [54] is mainly used for the synthesis of high quality UCNPs of $NaYF_4$ with β crystal structure. Alternatively, organometallic reagents can be replaced with Ln- chlorides using stoichiometric amount of F^- in order to avoid high toxic co-products formed during synthesis [23], [52]. Small β-$NaYF_4$ UCNPs with narrow size distribution can be synthesized with this synthesis procedure.

Some studies revealed that the formation of β-$NaYF_4$ UCNPs during thermal decomposition synthesis starts with the crystallization of α-$NaYF_4$ UCNPs, which is followed by the transformation of α-$NaYF_4$ to β-$NaYF_4$ UCNPs and finished with the

formation of pure β-$NaYF_4$ phase [51], [55], [56]. From [53], [55] mechanism in ODE/OA from Ln-oleate reagents was proposed as follows (Figure 1.4): at the initial stage amorphous precipitates from the reagents are formed. During the heating, small α-$NaYF_4$ UCNPs with polyhedral shape form and grow until they reach the size, at which the β-phase of $NaYF_4$ is thermodynamically more favourable. Consequently α-$NaYF_4$ UCNPs transform into the β phase in a form of hexagonal nanoplates. Due to the lower solubility of β-phase, β-$NaYF_4$ UCNPs grow on the expense of dissolving α-$NaYF_4$ UCNPs. Eventually, all α-$NaYF_4$ UCNPs are consumed and phase pure β-$NaYF_4$ UCNPs are obtained. The transformation from α-$NaYF_4$ into β-$NaYF_4$ is a typical disorder–to-order transformation. Namely, in the α-$NaYF_4$ crystal structure cations are randomly distributed in one sublattice, while in the β-$NaYF_4$ structure, there are three different cation sites (Figure 1.2) [51], [55]. The formation of β-$NaYF_4$ UCNPs can be followed from optical properties. A weak emission at the beginning of the reaction corresponds to the presence of the intermediate α-$NaYF_4$ UCNPs. A rapid increase in the UC emission intensity corresponds to the transformation from α-$NaYF_4$ to β-$NaYF_4$ UCNPs and high UC emission at the end of reaction is due to the strong emitting β-phase (Figure 1.4a) [53].

The size, morphology and crystal structure of synthesized UCNPs can be tuned with the ratio between the reactants (Ln^{3+}:Na), solvent and ligands (OA:OM:ODE), reaction time and temperature [57].

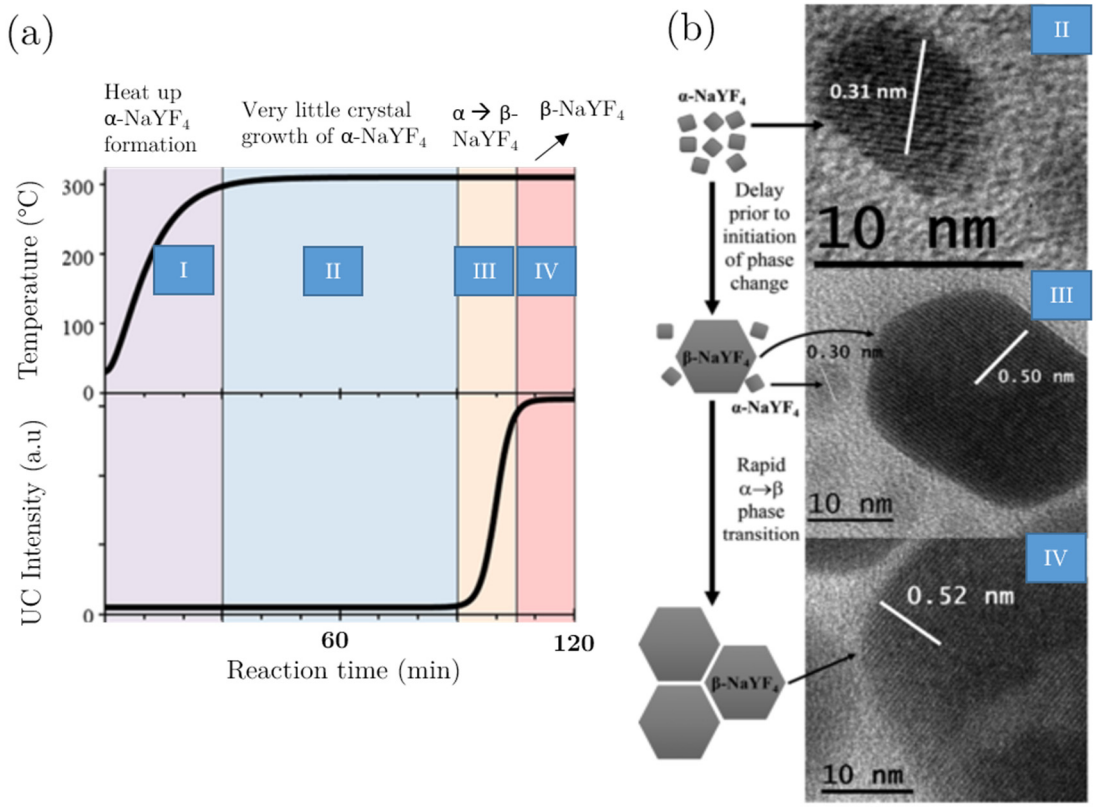


Figure 1.4: (a) Diagrams illustrating the correlation between the evolution of UC intensity and temperature as a function of reaction time with four reaction stages, which are schematically presented in (b) together with a high-resolution TEM images of the evolving UCNPs. Modified from [53].

1.2 UCNPs in Biomedicine

Any application of UCNPs in biomedicine requires their colloidal stability in different biological fluids and biocompatibility. The latter means that UCNPs are non-toxic, have no effect on the immune system and can perform its function without causing any side effects on cells during their short and long term usage. Biocompatibility can be achieved either by surface functionalization or with biocompatible coatings [2] (Figure 1.5).

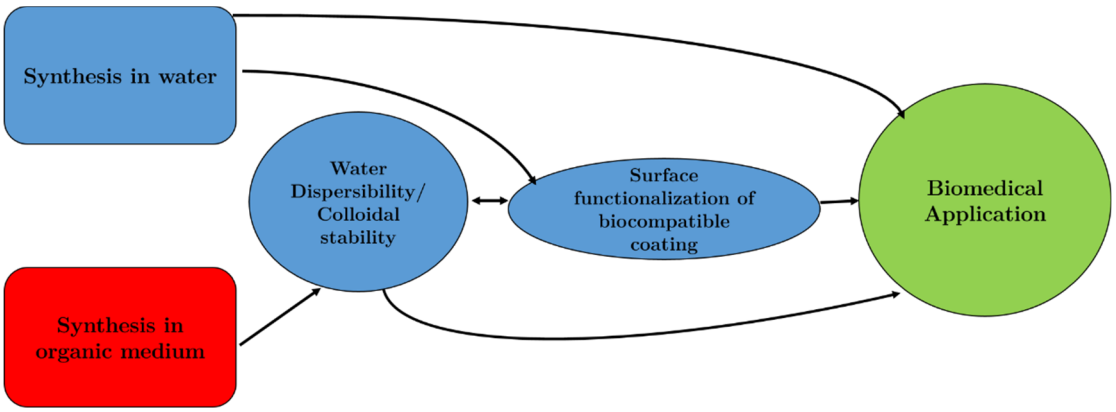


Figure 1.5: Different synthetic pathways to achieve biomedically applicable NPs. Modified from [58].

1.2.1 Colloidal Stabilization in Aqueous Systems

For the usage of UCNPs in medicine they have to be in the form of colloidal suspensions. Colloidal suspension is a system, in which one phase is homogeneously dispersed in another phase. There are several parameters that influence the colloidal stability and these are surface properties of particles, particles' size and shape, interactions between particles and between particles and solvent [59]. In order to stabilize particles in aqueous media attractive Van der Waals forces have to be overcome with repulsive forces, being electrostatic, steric forces or a combination of both types [59]–[61] (Figure 1.6).

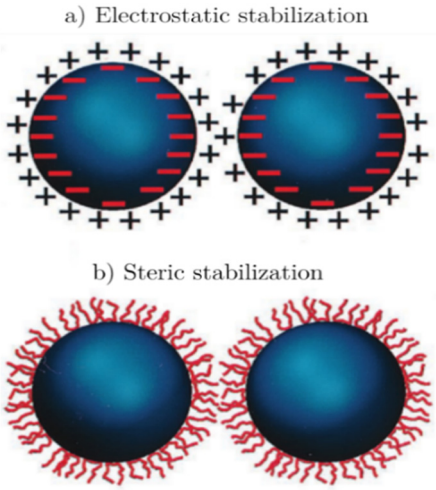


Figure 1.6: Schematic presentation of electrostatic (a) and steric stabilization (b) [61].

When particles are immersed in aqueous media, the charging of their surfaces can be a consequence of several processes:

- dissociation or ionization of groups on the particles' surfaces,
- adsorption of ions from aqueous media onto particles' surfaces.

When brought into a contact with an aqueous medium, most particles acquire a surface charge due to processes, mentioned above. This surface charge influences the distribution of nearby ions in the aqueous medium. Ions having the opposite charge (counter-ions) are attracted towards the surface and ions of the same charge (co-ions) are repelled away from the surface. All these, together with thermal motion of particles, result in the formation of an electric double layer (Figure 1.7a). The electric double layer theory deals with the distribution of before mentioned ions and therefore with the magnitude of the electric potentials in the vicinity of the charged surface. Stern (1924) proposed a model, where the electric double layer is divided into two parts: Stern layer and diffuse layer, and he also considered the possibility of specific ion adsorption. These two parts are separated by a plane – the Stern plane. Specifically, adsorbed ions are those that are attached by electrostatic and/or van der Waals forces to the surface and are located in the Stern layer – i.e., between the surface and the Stern plane. Ions located beyond the Stern plane form the diffuse part of the electrical double layer (Figure 1.7a). The distribution of ions in the diffuse part is influenced by electrostatic forces and random thermal motion. Within the diffuse layer there is a notional boundary, called slipping plane or surface of shear, inside which the ions and particle form a stable entity. When the particle moves, ions inside this boundary move with the particle, but ions beyond the boundary do not move with the particle. The potential at this boundary is called zeta (ζ)-potential. Although, surface potential (ψ_0) is not directly measurable it can be correlated with the ζ-potential. The latter can be measured electrokinetically and is proportional to the surface potential [59], [60].

$$\psi_0 = \zeta \, (1 + {}^{z}/_{r}) \exp(\kappa z) \tag{1.2}$$

Where z is the distance from the particle's surface to the surface of shear, r is the radius of the particle and ${}^{1}/_{\kappa}$ is the thickness of the electric double layer or Debye length.

The potential in electric double layer changes from ψ_0 (the surface potential) to ψ_d (the Stern potential) in the Stern layer, and decays from ψ_d to zero in the diffuse layer (Figure 1.7b).

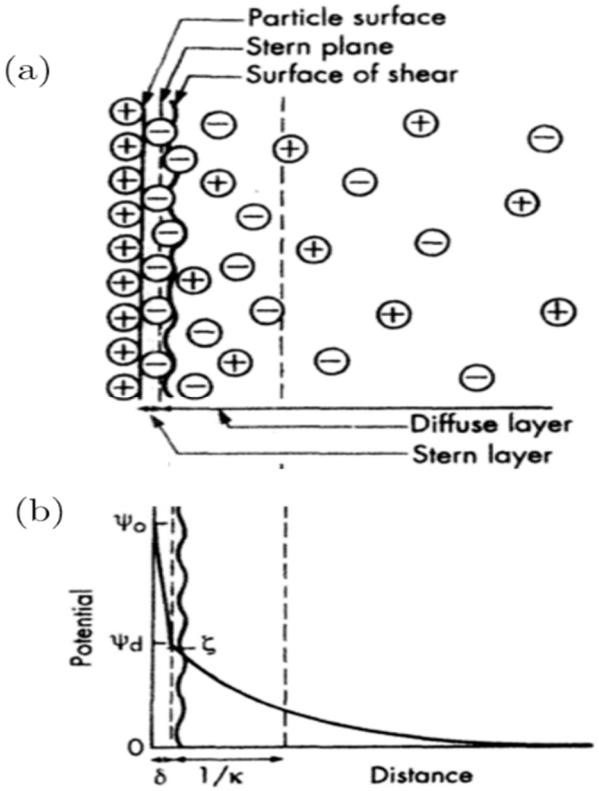


Figure 1.7: Schematic presentation of an electrostatic double layer (a) and the decay of surface potential with the distance from the surface (b) [59].

The DLVO theory was developed in 1940s by Derjaguin and Landau (1941) in Russia and by Verwey and Overbeek (1948) in Holland. This theory proposed that the stability of the suspension of particles depends on the total energy of interaction V_T between the particles. V_T is the sum of the two components, i.e. repulsive, electrostatic potential energy V_R and the attractive forces V_A (Equation (1.3)) [59], [60]:

$$V_T = V_R + V_A \tag{1.3}$$

Attractive forces arise from the Van der Waals forces while the repulsive forces depend on the electric double layer potential and thickness, particle radius and the dielectric constant of the medium [59], [60]:

$$V_R = 2\ \pi\ r\ \varepsilon\ \psi_0^2\ \exp(-\kappa h) \tag{1.4}$$

Where ε is solvent permittivity, κ is inverse Debye length, ψ_0 is the surface electric potential and h is the minimum separation between the particle surface.

When two particles with the same sign of a surface charge are brought together, they repeal each other. The total potential energy versus interparticle distance shows three features (Figure 1.8): two minima and an energy barrier. The shape of the curve (the height of the barrier and the depth of the minima) depends on the magnitude of the interacting forces. The magnitude of the repulsive forces, which define the height of the energy barrier, depends on several factors. The thicker the electric double layer, the repulsion between particles will be greater and so will be the suspension stability. The thickness of an electric double layer depends on ionic strength and decreases with increasing the ionic strength, consequently reducing the height of the potential energy barrier. With additional increasing

of ionic strength, energy barrier decreases further resulting in a secondary minimum (Figure 1.8). Particles are reversibly flocculated and suspension remains 'kinetically' stable. Following this, when repulsive forces are weak and the total interaction potential approaches the Van der Waals potential, particles are in the primary minimum where they are irreversibly agglomerated [29], [59], [60].

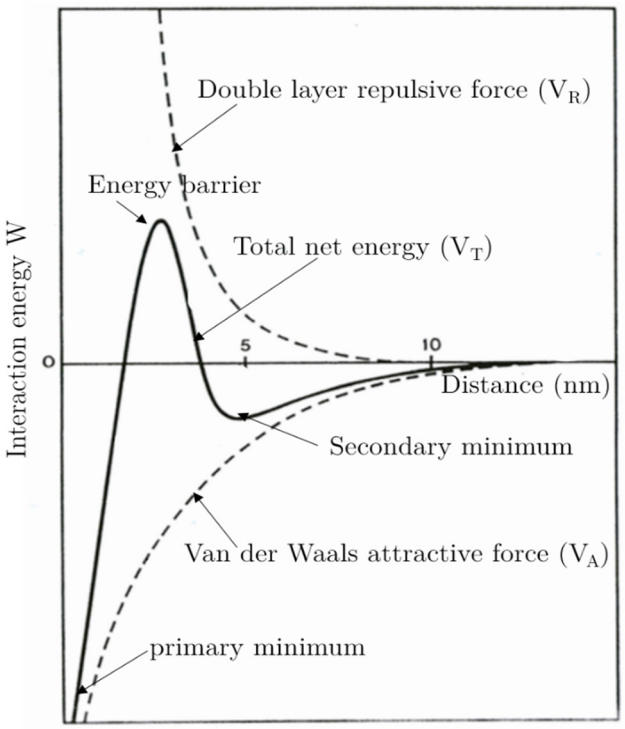


Figure 1.8: Schematic presentation of total interaction energy versus distance between two particles. Modified from [60].

1.2.2 Surface Functionalization of UCNPs

It is important to optimize strategies for the surface functionalization of UCNPs so that they can be used in biomedicine. UCNPs have to be dispersed in aqueous media and properly functionalized to achieve their biocompatibility.

There are numerous possibilities of surface functionalization of UCNPs and can be divided into ligand attraction, ligand exchange, ligand oxidation, layer-by-layer assembly (Figure 1.9) and silanization. Ligand attraction refers to the adsorption of an (additional) amphiphilic polymer via attractive hydrophobic interactions (Figure 1.9(a)) and will be further discussed in details. Another strategy of the surface functionalization is ligand exchange (Figure 1.9 (b)), which is based on the substitution of a hydrophobic ligand with the hydrophilic one that also provides surface groups for further bioconjugation. Ligand oxidation involves oxidation of C-C bond by Lemieux-von Rudloff reagent (i.e., mixture of $NaIO_4$ and $KMnO_4$) (Figure 1.9(c)). Layer-by-layer assembly involves sequential electrostatic adsorption of oppositely charged polyelectrolites (Figure 1.9(d)) [2], [31].

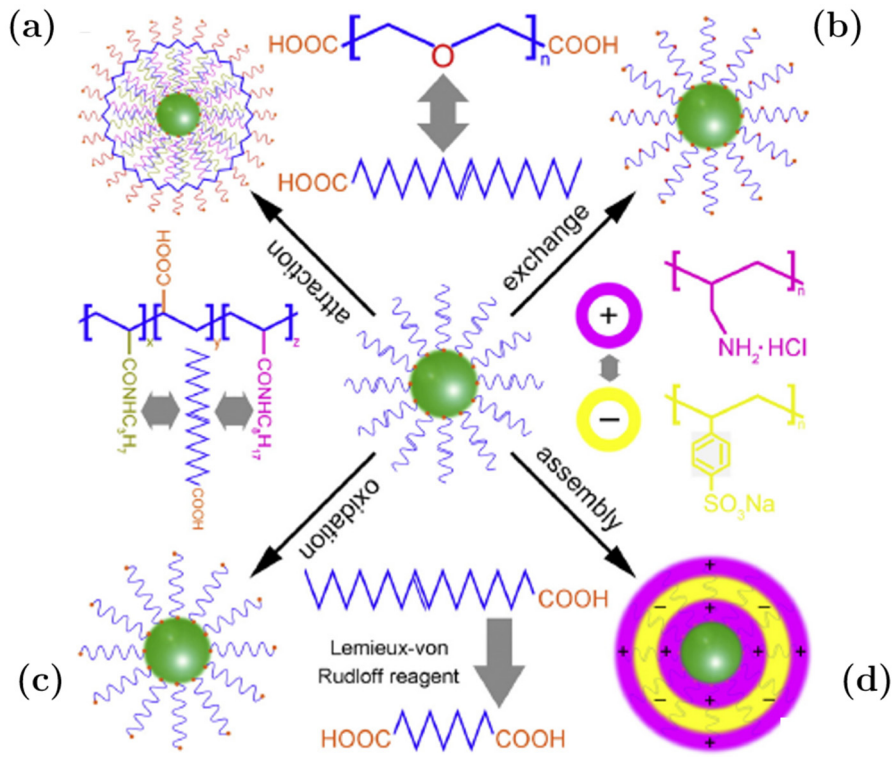


Figure 1.9: Illustrative presentation of different strategies for functionalization [31].

In addition to the above, silanization offers the possibility to covalently bond specific functional groups to the NPs via an amorphous silica coating. Silica coating is formed by heterogeneous nucleation of silica on the UCNPs surfaces. It starts with hydrolysis of siloxane monomers and it is followed by a condensation of siloxane precursors. Stöber method [62] with its modifications [63] is the most used method. Here, silica layer is formed in the presence of water, ethanol, tetraethoxysilane (TEOS) and ammonia as a catalizator. Silica is considered biocompatible [64]. Chemical procedures for the coating of UCNPs with silica are well established for hydrophilic and hydrophobic UCNPs [31], [64] [35], [65], [66], [67]. It was found out that the uniformity of silica coating can be improved when polyvinylpyrrolidone (PVP) was used as a capping ligand [31], [35], [67] (Figure 1.10). PVP enables aqueous dispersion of UCNPs [68], and pyrrolidone groups can coordinate with Ln^{3+} [31], [35], [68]. The silica coating allows for a subsequent silanization in order to enable conjugation with biological molecules. For instance, silanization with aminopropyltriethoxysilane (APS) provides amino surface groups for conjugation with folic acid (FA) that are targeted to folate receptors in cells [69], [70].

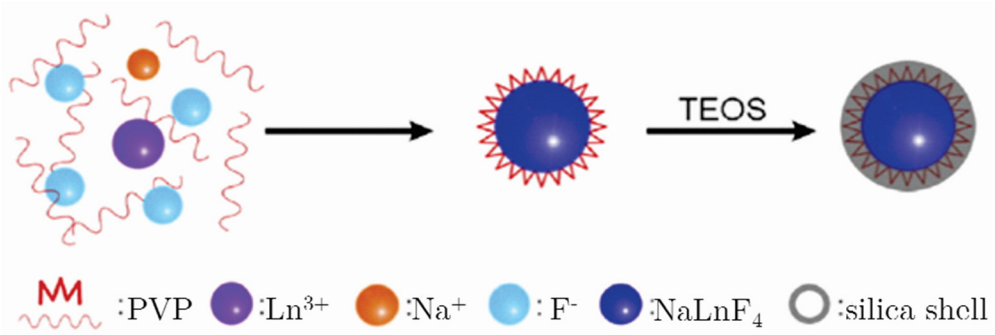


Figure 1.10: Schematic illustration of the formation of the silica coating via PVP onto $NaYF_4$: Yb^{3+},Er^{3+}@PVP UCNPs. Modified from [31].

1.2.3 Amphiphilic Coatings

β-$NaYF_4$ UCNPs synthesized with (modified) thermal decomposition are hydrophobic due to hydrophobic surface ligands (e.g., OA) and further surface functionalization is needed to disperse UCNPs into aqueous media and to enable their biocompatibility.

The word *amphiphile* originates from the Greek word *amphi* (meaning "two" or "both" or "on both sides") and the term means that amphiphile polymers consist of two parts. One part is soluble in polar media (the hydrophilic part) and another one is soluble in nonpolar media (hydrophobic part) (Figure 1.11). The hydrophilic part forms a head group of the amphiphilic polymer and the hydrophobic part of the amphiphilic polymer is a tail. The hydrophobic part (i.e., tail) of the surfactant may be linear or branched and of different lengths. The head group can be charged or not and is usually attached at one end of the hydrophobic part. When the head group is uncharged, this refers to non-ionic surfactant (i.e., D-α-Tocopheryl polyethylene glycol succinate (TPGS)), on the other hand the charged head groups can be divided into anionic (i.e., sodium dodecyl sulfate (SDS)), cationic (i.e., cetyltrimethylammonium bromide (CTAB)) or zwitterionic (amino acids) surfactants. Physicochemical properties of surfactants are affected by the length of a tail and the degree of branching, and the nature, size and position of the polar group [71]. The most common used amphiphilic polymers are based on poly(ethylene glycol) (PEG) and carbohydrates (i.e., dextran, chitosan). PEG as a ligand is especially suitable for providing a long circulation time and long-term stability in solutions with high salt concentrations and pH [58].

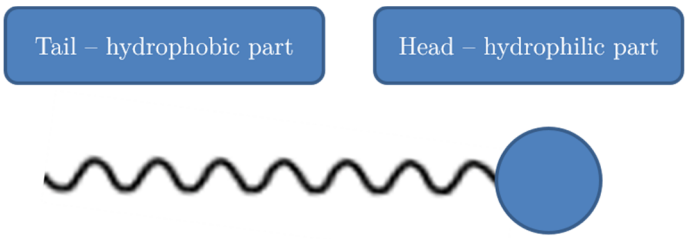


Figure 1.11: Scheme of amphiphilic polymer.

Ligand attraction is one of the possibilities of surface functionalization and involves adsorption of an amphiphilic polymer onto the NPs' surface through the hydrophobic attraction between the original hydrophobic ligand (e.g., OA) and the hydrophobic part of

an amphiphilic polymer. The latter intercalates with the hydrophobic ligand on the NPs' surfaces. The hydrophilic part (head) sticks out into water or other polar solvent, enabling colloidal stability and subsequent bioconjugation of UCNP [2].

The coating of NPs with amphiphilic polymers results in an increase of their hydrodynamic radius. This may in fact be an advantage for *in vivo* bioapplications, where long circulation times are required and are achieved by large enough particles [72], [73], [74]. Amphiphilic polymers could also prevent the contact between the NPs' surfaces and solvent when interaction between the two is not desirable. In our study we aimed to protect UCNPs against the dissolution in aqueous media by coating them with amphiphilic coatings: poly(maleic anhydride-alt-1-octadecene) (PMAO) crosslinked with bis(hexamethylene)triamine (BHMT) [19] and with D-α-Tocopheryl polyethylene glycol succinate (TPGS) [20].

1.2.3.1 Amphiphilic Co-Polymer PMAO-BHMT

PMAO is an amphiphilic polymer ($C_{22}H_{38}O_3$), composed of the hydrophobic part that consists of carbon atoms in each monomer unit and of the hydrophilic part of polymaleic anhydride, known to be biocompatible with combination with PEG [75], [76]. This combination allows for transferring hydrophobic $NaYF_4$ UCNPs via polymer cross-linking into different buffers for biolabeling applications and was reported by Guicheng Jiang and coworkers [19]. Octadecene chain of the PMAO intercalates with oleate ligand on the surface of the UCNPs due to the attractive hydrophobic interactions between the two. This is followed by cross-linking the anhydride rings of the PMAO with BHMT (Figure 1.12). There are several advantages of choosing the co-polymer PMAO-BHMT:

- The anhydride groups of the PMAO can be cross-linked with amine groups of BHMT forming amide bonds between two polymers,
- the cross-linked UCNPs with copolymers PMAO and BHMT show very high colloidal stability at different pH values and in physiological buffers [19],
- when functionalization with other copolymer is done (e.g. PEG-amine), makes NPs biocompatible [19], [75].

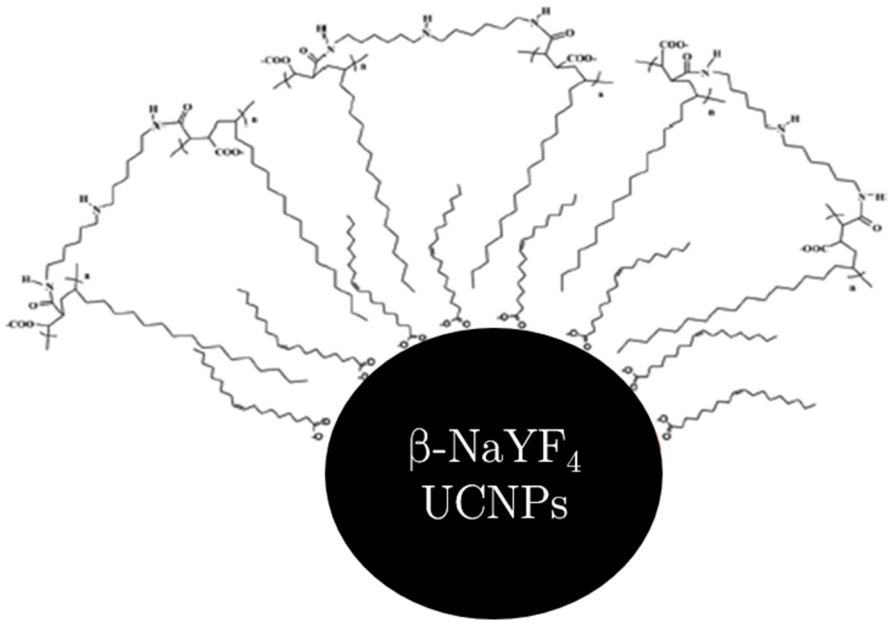


Figure 1.12: Illustration of cross-linked co-polymers stabilized-UCNPs. Modified from [19].

1.2.3.2 Amphiphilic Polymer TPGS

D-α-Tocopheryl polyethylene glycol succinate (Vitamin E TPGS or just TPGS) is a water-soluble non-ionic amphiphilic polymer (Figure 1.13). It is formed by esterification of Vitamin E succinate (hydrophobic part) and polyethylene glycol (PEG) (hydrophilic part). FDA has approved TPGS as a safe pharmaceutical adjuvant used in drug formulation [77]. TPGS is proposed for the usage in developing drug delivery systems and has been used as emulsifier, solubilizer, stabilizer, adsorption enhancer, resulting in high drug encapsulation efficiency, high cellular uptake *in vitro* and high therapeutic effects *in vivo* [77]–[79].

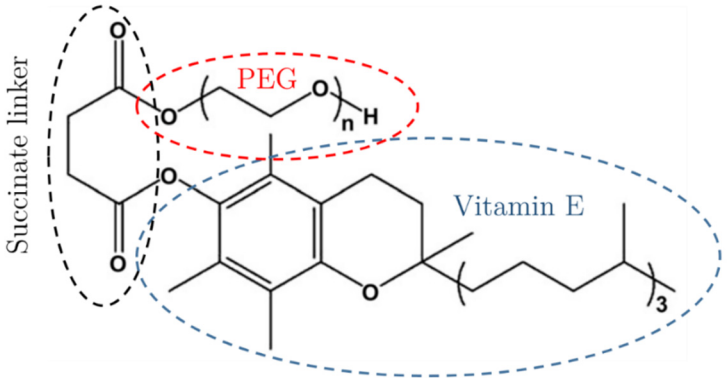


Figure 1.13: Chemical structure of TPGS [77].

TPGS can be potentially used for overcoming multi-drug resistance that is a major failure in cancer chemotherapy. It was used as a surface modifier to functionalize UCNPs enabling excellent water solubility [20]. TPGS was also used for clustering of iron oxide NPs for *in vivo* magnetic resonance (MR) imaging [80].

1.2.4 Biological Applications

UCNPs were suggested for a range of applications in medical diagnostics and also in nanotheranostics:

I. *Fluorescence imaging application*, where UCNPs can be used for cellular or *in vivo* imaging [16], [18], [81], [82]. Cellular imaging means that UCNPs are targeted to subcellular components and their spatial and temporal distribution of the resulting fluorescence is imaged [28]. For example, efficient fluorescence from a single Ln-doped UCNP was investigated and demonstrated that β-$NaYF_4$ UCNPs emit bright anti-Stokes fluorescence with superior photostability, without blinking, being suitable for single-molecule imaging [83]. Polyethyleneimine (PEI) coated UCNPs, functionalized with folic acid (FA) showed great potential *in vitro* imaging of cancer cells [84]. Excellent fluorescence efficiency in the "biological window" of CaF_2: Tm^{3+}, Yb^{3+} UCNPs with 2 mm of the penetration depth was reported [85].

II. *Magnetic resonance imaging (MRI)* [86], [87], where Gd-based UCNPs are used as a contrast agent with its relatively long electronic relaxation times [1]; *computed tomography (CT) imaging* [20], [72], [88], as excellent candidates for contrasting agents due to their large atomic numbers and, consequently, large X-ray attenuation coefficient values [1] and *multi-modal imaging* (i.e., fluorescence/MRI/CT imaging) where two or more imaging modalities are combined into UCNPs [89]–[91].

III. For *drug delivery systems* [92]–[94], *photothermal therapy (PTT)* [1],[95] or in *photodynamic therapy (PDT)* [2], [96]. One of the possible drug delivery systems is mesoporous silica shell, where drugs are concentrated in the pores of the shell that is coated on the surface of UCNPs. For instance, $NaYF_4$: Yb^{3+},Er^{3+}/$n$$SiO_2$/$m$$SiO_2$ nanospheres, where ibuprofen (IBU) was loaded into mesoporous silica shell and the controlled drug release of IBU was demonstrated [92]. During the PTT therapy emission produced by UCNPs is converted into heat by absorption of i.e., Au NPs that causes local hyperthermia to kill cancer cells [95]. PDT is the treatment that uses cytotoxic reactive oxygen species (ROS) generated with light. PDT includes three components, i.e. photosensitizer, light source and the oxygen. Photosensitizer is excited under appropriate wavelength and reacts with an oxygen molecule producing highly cytotoxic ROS. The latter can kill cancer cells. NIR-excitable UCNPs are energy donors and carriers for photosensitizers [4].

IV. For *bioassays* [97] and *Förster Resonance Energy Transfer (FRET)* [98], [99], [100]. FRET is a process between fluorescent donor (i.e. UCNPs) and acceptor molecules [2]. Wang *et al.* [99] used biotinylated UCNPs as energy donors and biotin-gold NPs as energy acceptor for the detection of avidin. Gold NPs have strong absorption at 520 nm and this matches well with the fluorescence of $NaYF_4$:Yb^{3+},Er^{3+} UCNPs. Biotin-gold NPs were conjugated to biotinylated UCNPs through the sensitive and selective interaction between avidin and biotin. In this way the donor and the acceptor are brought in close proximity due to avidin. Based on decrease of fluorescence intensity of UCNPs when energy transfer occurs this can be used as a biosensor for detection of avidin.

V. Fluorescent *nanothermometer biosensors* are capable of determining the temperature in biological systems [101]. Their temperature sensitivity is based on the intensity ratio of the green fluorescence of the Er^{3+} dopant ($^2H_{11/2}$ → $^4I_{15/2}$ and $^4S_{3/2}$ → $^4I_{15/2}$) that changes with the temperature.

1.3 Dissolution and Possible (Cyto)Toxicity of UCNPs

1.3.1 Dissolution of NPs

The dissolution of solid particles in liquids involves the dissociation of solute molecules on the solid surface through surface reaction and subsequent diffusion of the disintegrated solute molecules towards the bulk liquid phase. Dissolution can be controlled either by surface reactions or by diffusion [102], [103]. When NPs dissolve its constituent ions migrate from the surface to the bulk solution, forming a diffusion layer (Figure 1.14). The driving force for the dissolution is the concentration gradient between the NPs surface and bulk solution phase. When the concentration in the bulk phase reaches equilibrium solubility, the dissolution process stops [103], [104], [105], [106]. Solubility expresses the maximum concentration of a compound (the solute) that can dissolve in a specific solvent at defined temperature and pressure [107]. The dissolution of a compound continues until the solution is saturated. Saturation is the state with the undissolved solute in equilibrium with the dissolved solute [108]. The solubility of a material in a specific solvent is determined with a solubility product constant (K_{sp}). K_{sp} is the equilibrium constant for the dissolution of salts into its constituent ions [107].

The dissolution process is dependent on system properties (concentration of NPs, pH, ionic strength, solvent-media composition etc.). The dissolution of NPs is also significantly affected by their small size, as NPs dissolve faster and to a greater extent than the bulk material of the same composition [103], [109]. This is the reason why the potential dissolution of NPs has to be evaluated when considering them for biomedical applications.

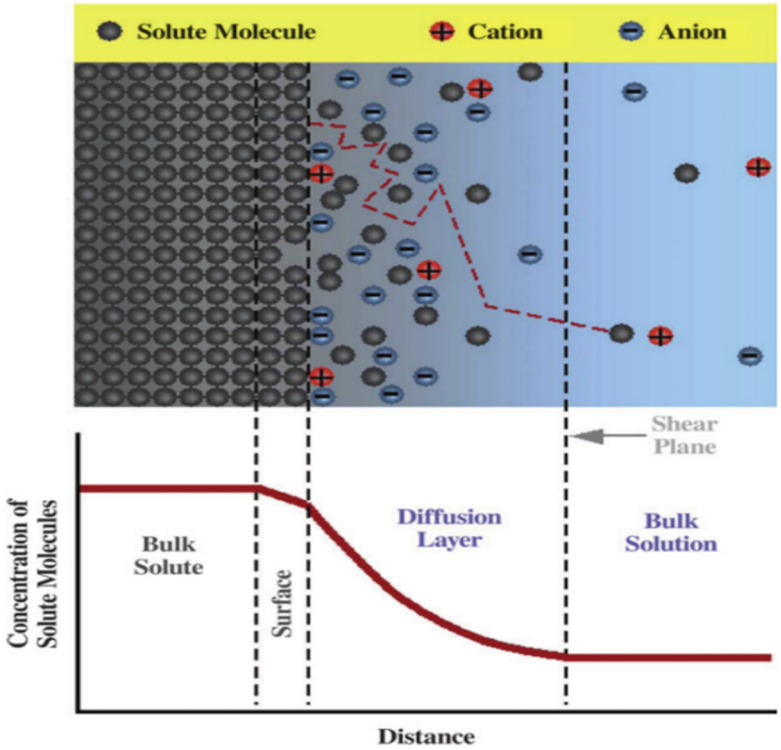


Figure 1.14: Simplified representation of the dissolution process (top) and the concentration of solute molecules as a function of distance from particle's surface (bottom) [104].

Role of the surface morphology and size

Differently shaped NPs of the same material, considering having equivalent surface area, will undergo dissolution at different rates. Convex surface structures ($r > 0$) have a greater equilibrium solubility than the concave surface structures ($r < 0$) (Figure 1.15).

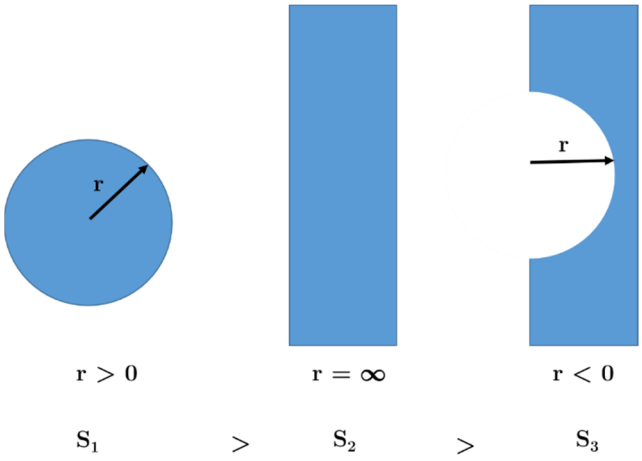


Figure 1.15: The solubility of a surface with positive curvature ($r > 0$) exceeds the solubility of a flat surface ($r = \infty$) and, even more, of a surface with negative curvature ($r < 0$). After [110].

The Ostwald-Freundlich equation [111] for the solubility of spherical particles in solutions predicts that NPs with smaller radius of positive curvature (i.e., convex) are energetically unfavorable (have higher surface free energies) and their equilibrium solubility is larger than that of coarser particles [104], [110].

$$s = s_0 \, exp\left[\frac{\gamma V_m}{RT} \times \frac{2}{r}\right] \tag{1.5}$$

Here s is the solubility at given conditions, s_0 is the equilibrium solubility, γ is the surface tension, V_m is the molar volume and r is the radius.

Effect of agglomeration

Due to attractive van der Waals forces NPs have the tendency to agglomerate. This can hinder the dissolution by slowing down the diffusion process. When agglomerates are formed, some parts of the NPs' surfaces are no longer directly exposed to the bulk solvent, thus slowing down the diffusion of the solute ions into bulk solution. At the same time the area of negative surface curvature is (apparently) enlarged. As mentioned previously, the solubility is the lowest for surfaces with negative curvature (i.e., concave) (Equation (1.5), Figure 1.15) [104].

Effect of adsorbed species (surface chemistry effect)

The absorption of ions from the solution can have an effect on the dissolution. They can promote or reduce it by changing the diffusion layer properties [112]. When ions are adsorbed on the solid surface, this results in lower interfacial tension and in the increased diffusion barrier, hindering the dissolution. Some classes of ligands, e.g., chelating agents, can change the dissolution with complexation of the solute ions. Consequently, the concentration of dissolved ions decreases and promotes further dissolution [103], [104]. The effect of surface chemistry on the degree of dissolution has been extensively studied for

different NPs, i.e., Ag NPs [113] and ZnO NPs [114], and for calcite particle dissolution [115]. For example, PVP-stabilized Ag NPs showed higher dissolution degree than the citrate-stabilized Ag NPs at the same aging conditions [113].

Moreover, imperfections, like structural defects, contaminants, and surface properties (i.e., roughness, dominant crystal orientation) can affect (promote or hinder) the dissolution [103], [110].

Effect of the solvent media

Properties of the solvent media (i.e., pH, ionic strength, etc.) and the presence of inorganic and (natural) organic components (i.e., proteins, etc.) can influence the NPs' solubility and also the suspension colloidal stability, which indirectly affects the dissolution via agglomeration/aggregation of NPs [103], [106], [116], [117]. For example, CuO NPs dissolved completely in amino-acid-rich but not in pure water [118]. The interaction of NPs with the media components can also cause precipitation and complexation of dissolved ions from NPs, influencing their further bioavailability [106].

Kinetics of the dissolution

The dissolution of NPs usually follows the first-order kinetics, which depends on the concentration of, at least one of the dissolved ions [105].

$$-\frac{dM}{dt} = k_{dis} \times M, \tag{1.6}$$

where M is the concentration of the dissolved ion and k_{dis} is the dissolution rate constant in units per time (s^{-1}, h^{-1}, day^{-1}). Therefore, the dissolution rate is proportional to the concentration of the dissolved ion. By following the variation of the ion's concentration, it is possible to estimate the half-times of the dissolved ions as a measure of their dissolution [105]:

$$t_{1/2} = ln2/k_{dis}\ , \tag{1.7}$$

where $t_{1/2}$ is the half time (in units of time) and k_{dis} is the dissolution rate constant [105]. Dissolution half-times of selected NPs calculated from k_{dis} following the first order dissolution kinetics are given in Table 1.1. In addition, the effect of the size and different conditions on the degree of NPs dissolution is also shown.

Table 1.1: Calculated dissolution half-time $t_{1/2}$ for some NPs [105].

NPs and their size (nm)	Conditions	Rate of dissolution	Calculated half-time $t_{1/2}$ (h)	Obtained from the literature
Ag; 4.8	Citrate stabilized	4.1 day^{-1}	4	[119]
Ag; 60	Citrate stabilized	0.74 day^{-1}	22.5	[119]
Ag; 4.8	Citrate stabilized, deionized water, at 0.05 mg/l total silver	0.88 day^{-1}	18.9	[119]
TiO_2; 1–24.4	In aqueous NaCl solutions at temperatures of 25 and 37 °C, pH ~ 3.3	3.3×10^{-2} h^{-1}	21	[120]

1.3.1.1 Dissolution of Ln-fluoride Compounds in Water

In the subsequent text Ln denotes lanthanide ions, including Y^{3+} and Sc^{3+}. The solubility of the Ln-fluorides powders is increasing with the increasing atomic number of Ln. Ln-fluoride should dissolve in water as below [121]:

$$LnF_3\ (s) \rightarrow\ Ln^{3+}\ (aq) + 3F^{-}\ (aq) \tag{1.8}$$

If there are no other ions in the solution, the solubility product K_{sp} of LnF_3 is given as [121]:

$$K_{sp} =\ [Ln^{3+}]\ [F^{-}]^3 \tag{1.9}$$

Table 1.2: K_{sp} values for some Ln-fluorides powders in water at 25 °C [121].

Ln-fluorides powders	K_{sp}	pK_{sp}
LaF_3	3.26×10^{-21}	20.5
GdF_3	2.36×10^{-19}	18.6
ErF_3	1.52×10^{-18}	17.8
TmF_3	2.55×10^{-18}	17.6
YbF_3	6.43×10^{-18}	17.2
YF_3	4.41×10^{-19}	18.4
ScF_3	2.98×10^{-12}	11.5

Based on the K_{sp} values (Table 1.2), binary fluorides could be considered as (almost) insoluble in water. Unfortunately, there is a lack of information about K_{sp} of ternary fluorides. The value reported for NH_4ScF_4 ($K_{sp} = 2.55 \times 10^{-12}$) [122] is comparable to that of the ScF_3 (Table 1.2). One could speculate that the K_{sp} values of other Ln-based ternary fluorides might be in the range of the K_{sp} values of related binary fluorides (Table 1.2). The low solubility of LnF_3, and consequently their chemical stability, enables their synthesis in the form of NPs from solutions [123].

The particle-size dependence of the solubility of LnF_3 was suggested from larger solubilities of the LnF_3 powders in comparison to the respective single crystals [123]. The solubility of Ln-fluorides is pH dependent and can also be altered by the presence of specific ligands, which complex Ln^{3+} ions [124], [125].

1.3.2 Effect of Dissolution on Possible (Cyto)Toxicity

1.3.2.1 General Toxicity of NPs

NPs possess different chemical and physical properties than the bulk material of the same composition due to their small size and large surface-to-volume ratio. Majority of the atoms in NPs are located at their surfaces, which are also rich in structural and chemical defects. All these result in a high surface energy. To reduce this high surface energy, NPs tend to agglomerate, and adsorb or react with surrounding species [126].

Up to date, most of the toxicity studies are performed taking into account only chemical composition and substance dose, which is suitable for classic drugs but not adequate for NPs. For the latter, there are additional parameters that have to be taken into account, i.e. surface composition of the NPs, hydrodynamic size, redox properties, colloidal stability, expected retention time and dissolution in relevant media [126].

NPs can be internalized in cells in different ways. Endocytosis is a process, during which cells actively participate in the transport of NPs into cell, whereas passive transport is a process of direct diffusion of NPs through a cell membrane. During this process NPs can disrupt the membrane lipid bilayer integrity, which could be a reason for the cytotoxicity [126].

Cytotoxicity is observed on a molecular level (i.e., DNA damage, mRNA degradation) or subcellular level (i.e., membrane permeability changes or its disruption, mitochondrial activity perturbations leading to apoptosis) [126].

Some illustrative interactions of NPs with a cell and possible damage is schematically shown in Figure 1.16.

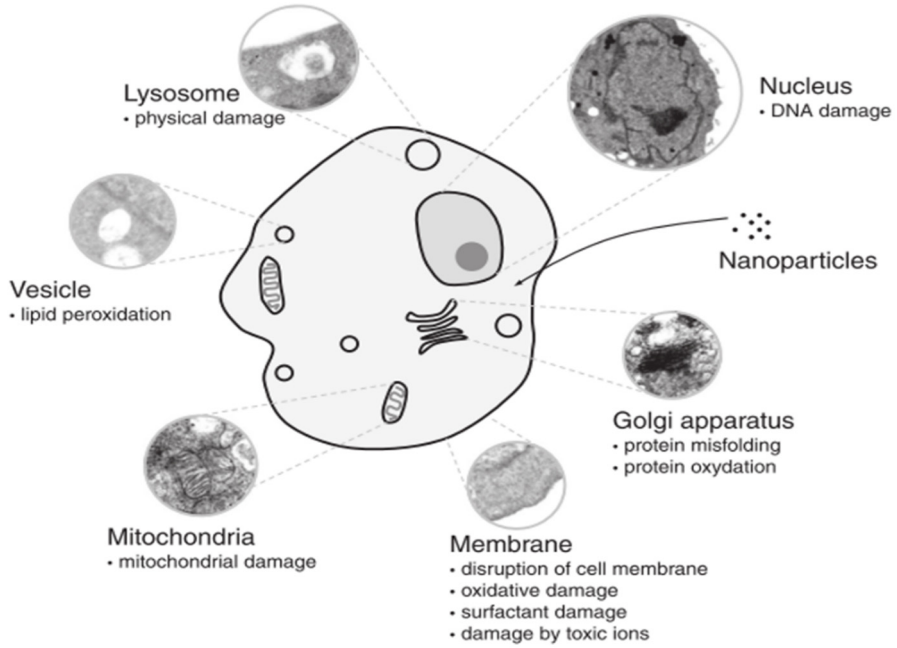


Figure 1.16: Simplified illustration of NPs interactions with a cell, resulting in various damage effects [127].

1.3.2.2 Adverse Effects of F^-

Toxicity of F^- is related to its high biological and chemical activity. F^- diffuses fast through cell membranes, often in the form of HF and its permeability is several orders of magnitude greater than that of F^-. The main source of F^- for humans is drinking water. The F^- has been proven to be beneficial in low concentrations, for example for teeth and bone development [128], [129]. Because of the beneficial effect of dietary fluoride on the prevention of caries the adequate intake (AI) of fluoride has been set to 0.05 mg/kg body weight per day. The AI covers fluoride intake from all sources, including non-dietary sources such as toothpaste and other dental hygiene products [130]. Fluorosis, a consequence of an excessive F^- consumption, is a slow degenerative disease, mostly influencing teeth and bone tissues, but also causing mental retardation and neurological defects [128], [129]. Some cytotoxic effects associated to F^- exposure are listed in Table 1.3.

Recent studies revealed the toxicity of F^- *in vitro* and *in vivo* for cells in different tissues. It was shown that high concentrations of F^- can induce apoptosis (cell death) by oxidative stress or ATP depletion, and can negatively influence the functional, metabolic and structural functions in cells. The F^- also affects the cell cycle progression, oxidative

stress, DNA damage, inhibition of protein synthesis in sufficiently large concentration (few mM) [128], [129]. Due to this systematic dissolution studies of fluoride Ln-doped UCNPs need to be performed for understanding their potential cytotoxic threat.

Table 1.3: Some cytotoxicity effects associated to F^- exposure [128].

Type of the studied cells	Concentration of F^- exposure (mM)	Time of F^- exposure (h)	Cytotoxic effect	Reference
Primary rat hippocampal neurons	1.05–4.2	24	Increased generation of ROS and increased lipid peroxidation	[131]
Hepatocellular carcinoma cells	3	for 6 and 24	Increase of gene expression of Mn-SOD	[132]
Neuroblastoma cells	0.05–5	24	Increase of protein oxidation and lipid peroxidation	[133]

1.3.2.3 Adverse Effects of Ln^{3+} and (Cyto)Toxicity Studies of Ln-based NPs

Ln^{3+} ions are toxic and they can interact with biological molecules in cells, causing some side effects, for instance lipid peroxidation [127]. It was also observed that RNA polymerase II activity decreased when exposed to Sm^{3+}, Nd^{3+} and Pr^{3+}, but increased for Gd^{3+}, Er^{3+} and Dy^{3+} nitrates. Influence on blood content (decreasing the content of cholesterol, collagen, elastin, *etc.*) and decreasing the activity of some enzymes, e.g., NADH dehydrogenase was caused by Ln chlorides [126]. Gd^{3+} was reported to cause nephrogenic systemic fibrosis [134], [135] and exposure to the La^{3+} and Yb^{3+} ions might be involved in the neurological adverse effects [136], [137]. Recent studies showed that from Ln_2O_3 NPs Ln^{3+} was released and interacted with cellular phosphates [126], [138].

To the best of our knowledge, the dissolution of fluoride UCNPs has not been investigated yet. However, there were some studies related to the dissolution of Ln^{3+} from Ln-based NPs. For instance, Ln-doped Gd_2O_3 UCNPs showed a cytotoxic effect on macrophages, which was attributed to poor chemical stability of Gd_2O_3 [82]. This was improved by coating the UCNPs with PEG-PAA. Alternatively, Wang and co-workers [89] used a protecting shell of CaF_2 for the core from UCNPs to prevent the Ln^{3+} leakage in buffers, suitable for bioapplications. Dissolution of Yb^{3+} from Yb_2O_3 NPs showed on the precipitation of the dissolved Yb^{3+} into $YbPO_4$ [139]. Moreover, phytotoxicity of La_2O_3 NPs was investigated in cucumber roots and dissolution of NPs at the surface of the root was induced by organic acids that were extruded from root cells. After the dissolution of the La_2O_3 NPs free La^{3+} interacted with phosphates. The needle-like clusters of $LaPO_4$ were accumulated at the intercellular spaces [140].

Most of the studies on fluoride UCNPs reported limited or no cytotoxic effect *in vitro* or *in vivo* [69], [89], [141]–[143]. As reported in a review of Assessing the toxicity of UCNPs' [126], cytotoxicity of UCNPs was investigated in different cells (Table 1.4). UCNPs had no significant toxicity, however their health risk is still under question and more detailed studies are required for further evaluation. Very small UCNPs can accumulate in different cells and in the worst scenario, they may even penetrate into nuclei. Following this, some articles already pointed out possible adverse effect of UCNPs [82], [144], [145]. It was suggested that UCNPs partially decomposed or were damaged inside macrophage cells since UCNPs were not extracted and absence of their fluorescence was observed [144]. UCNPs cytotoxicity was also tested on zebrafish embryos and at a higher dose of UCNPs

(200 µg/ml) abnormalities were observed [145]. The cytotoxic behavior in macrophages that were incubated with bare UCNPs was also observed [82].

Table 1.4: Some cytotoxicity studies of different UCNPs [126].

UCNPs	Size (nm)	Surface composition	Cells for testing	UCNPs concentration [µg/ml)	UCNPs incubation time (h)	Cell viability (%)	Reference
$NaYF_4$:Yb^{3+},Er^{3+}	21.0±0.5	Silica	Skeletal myoblasts	100	24	87.8	[64]
				100	48	68.2	
$NaYF_4$:Yb^{3+},Tm^{3+}	~11.5	Poly(acrylic acid) PAA	KB	6–480	24	> 94	[146]
				480	48	> 80	
$KGdF_4$:Yb^{3+},Er^{3+}	~14	PEI	HeLa	0–5000	20	60	[147]
LaF_3:Yb^{3+},Ho^{3+}	~15	PEG	KB	500	4	> 78	[143]
LaF_3:Yb^{3+},Er^{3+}	~15	PEG	KB	500	12	> 78	[143]
Gd_2O_3:Yb^{3+},Er^{3+}	NA	Bare	B-cell hybridoma	1–100	48	< 60	[82]
	NA	PEG-PAA		1–100	48	90	

Chapter 2

Aims and Hypothesis

2.1 Aims

The purpose of the dissertation was to obtain basic knowledge on the dissolution of fluoride UCNPs in aqueous media. This is related to their potential application in medical diagnostics, for which any release of (potentially) toxic Ln^{3+} and F^- ions should be prevented or minimized below the toxicity level. Considering the time frame of diagnostic procedure, the dissolution of fluoride UCNPs was studied in details and correlated to their chemical stability in biological environment. The additional purpose of the dissertation was to apply a specifically designed surface coating to significantly decrease the dissolution degree and rate of fluoride UCNPs.

The selected UCNPs were binary fluorides of LnF_3 (Ln = La or Gd) and a ternary fluoride $NaYF_4$, all codoped with Yb^{3+} and Tm^{3+}. Hydrothermal/solvothermal synthesis often leads to α-$NaYF_4$ UCNPs, with a metastable structure and inferior optical properties to those of the thermodynamically stable β-$NaYF_4$:Yb^{3+},Tm^{3+}, which can be synthesized only at high temperature, typically in organic media using thermal decomposition synthesis. The synthesis route also influences the size of NPs and on the formation of structural and surface defects, which can further influence on their solubility rate. In general, the solubility (rate) of a specific compound increases with the temperature, and for the fluorides, it additionally increases with a decreasing pH value. Finally, protective coatings were designed and tested for their effect on the dissolution rate of fluoride UCNPs.

In addition to this, the dissolution may also affect optical properties of the studied UCNPs due to the changes in their surface chemistry and/or in the crystal field of the Ln^{3+} ions. The intensity ratio of different fluorescence bands as well as the fluorescence lifetimes of the different bands may reveal changes in the immediate microenvironment of the sensitizer and emitter ions with respect to the as-synthesized fluoride UCNPs and can, at the same time, provide a simple tool for a control of the long-term stability of fluoride UCNPs. The results of these measurements are expected to be very important for the future use of UCNPs e.g., for fluorescence microscopy diagnostics.

2.2 Hypothesis

Our first hypothesis is that fluoride UCNPs dissolve in aqueous media and that this may result in a cytotoxic effect. This is based on the fact that the dissolution rate of NPs is significantly higher than that of larger particles or bulk of the same composition. We also presume that materials properties (composition, structure, surface chemistry, size of NPs) and external parameters (temperature, pH, composition of the media) significantly affect the dissolution rate of fluoride UCNPs.

The second hypothesis is that an amphiphilic coating can decrease (or prevent) the dissolution degree and rate of fluoride UCNPs. The inner surface layer(s) should be hydrophobic to prevent the contact of the surface of UCNPs with water and, with it, the diffusion of the ions from the surface into surrounding aqueous environment and water molecules to the surface of UCNPs. The outer surface layer(s) should be hydrophilic in order to enable biocompatibility of the UCNPs.

We also assume that the dissolution can have an effect on the surface chemistry or crystal field of fluoride UCNPs, which can further result in a decreased intensity of different fluorescence bands, as well as in different lifetimes or quantum yields. Therefore, our third hypothesis is that the correlation between structural defects and specific optical properties can form a basis of advanced analysis of the dissolution of UCNPs.

Chapter 3

Materials and Methods

3.1 Materials

List of chemicals used in experimental work:

NaCl (min. 99 %), $LnCl_3{\times}(nH_2O)$ (Ln = Y (99.99 %), Gd (99.9 %), Yb (99.9 %), Tm (99.9 %), La (99.99 %)), $Ln(NO_3)_3{\times}(nH_2O)$ (Ln = Y (99.9 %), Gd (99.9 %), Yb (99.9 %), Tm (99.9 %), La (99 %)), NaF (99 %), NH_4F (98 %), oleic acid (OA, 90 %), 1-octadecene (ODE, 90 %), ethylene glycol (EG, 99 %), tetraethoxysilane (TEOS, 99.9 %), polyvynilpyrrolidone (PVP, M. W. 40000) and citric acid (CA, 99 %) were all purchased from Alfa Aesar. NaOH ($\geq$ 99 %), $NaBF_4$ ($\geq$ 97 %), NH_4OH (25 %), chloroform and methanol were purchased from Merck. Ethanol ($\geq$ 99.9 %), acetone (99.8 %), cyclohexane ($>$ 95 %) and hexane ($>$ 95 %) were purchased from CarloErba Reagents. HNO_3, HCl and diethyl ether (DE) (99.5 %) were purchased from Applichem. Bis(hexamethylene)triamine (BHMT, high purity), poly(maleic anhydride-alt-1-octadecene) (PMAO, Mn 30000–50000) and D-α-Tocopherol polyethylene glycol 1000 succinate (TPGS) were purchased from Sigma Aldrich. Phosphate buffer saline (0.1 M PBS, 10X, pH = 6.8) was purchased from Alfa Aesar. The as-received PBS was additionally diluted for 8.5-times to adjust the pH to 7.4 ($\sim$ 0.01 M PBS, 1X PBS) for dissolution studies. Deionized water was used in all the experiments. All reagents were used as received without any additional purification. To ensure a proper stoichiometry of the products, the Ln^{3+} content in the reagents was determined using an optical fluorescence spectrometer with inductively coupled plasma (ICP-OES, Agilent 720).

3.2 Methods

3.2.1 Synthesis of UCNPs

Synthesis of binary fluoride UCNPs

Hydrothermal synthesis (HS) of binary fluoride UCNPs, LaF_3 and GdF_3 UCNPs, all codoped with 5 at.% Yb^{3+} and 0.5 at.% Tm^{3+} (La-HS and Gd-HS) (Table 3.1) was carried out from Ln nitrates at 180 °C for 6 h [39]. $NaBF_4$ was used as a fluorine source. In short, 5 ml of stoichiometric amounts of Ln nitrates (total of 1 mmol) was added to 10 ml of aqueous solution of sodium citrate (Na_3Cit) (2 mmol, the molar ratio of Cit: Ln^{3+} = 4:1) to form Ln-Cit complex. Na_3-Cit was prepared by dissolving a stoichiometric ratio of NaOH and CA in water. After stirring, 15 ml of aqueous solution of $NaBF_4$ (25 mmol) was introduced into the nitrate solution. pH of the mixture was adjusted to pH $\sim$ 1 with HNO_3 (c = 1 M). After agitation for 15 minutes, the mixture was transferred into a 70 ml Teflon vessel tightly sealed in a stainless steel autoclave and heated with 3 °C/min to 180 °C with

a holding time of 6 h. As the autoclave cooled to room temperature naturally, the precipitates were separated by centrifugation at 5000 rpm for 5 min, washed with deionized water and ethanol, and finally dried in air at 80 °C for 6 h.

The solvothermal synthesis (SS) of the LaF_3 and GdF_3 UCNPs, all co-doped with 5 at.% Yb^{3+} and 0.5 at.% Tm^{3+} (La-SS and Gd-SS) was carried out in EG at 180 °C for 6 h using a slightly modified procedure from ref. [46]. $NaBF_4$ (8 mmol) was dissolved in 20 ml of EG and afterwards, a solution of 2 mmol of Ln chlorides in a stoichiometric ratio in 20 ml of EG was added under vigorous stirring. After 20 min, the mixed solution was transferred into a 70 ml autoclave, as described above, and maintained at 180 °C for 6 h. The precipitates were separated by centrifugation, washed with deionized water and ethanol in sequence several times and then dried in air at 80 °C for 6 h. La-SS-nitrates were prepared under the same procedure as La-SS with exception that Ln nitrates were used as reagents (Table 3.1).

A series of undoped binary fluorides were synthesized without dopants (i.e., Yb^{3+}, Tm^{3+}) with HS and SS using the same procedure as for the doped ones (Table 3.1).

Table 3.1: Synthesis parameters for binary fluoride UCNPs.

Binary fluoride UCNPs	Sample name	Solvent	Reagents
LaF_3:20%Yb^{3+},2%Tm^{3+}	La-HS	water	Ln nitrates
GdF_3:20%Yb^{3+},2%Tm^{3+}	Gd-HS	water	Ln nitrates
LaF_3:20%Yb^{3+},2%Tm^{3+}	La-SS-nitrates	EG	Ln nitrates
LaF_3.20%Yb^{3+},2%Tm^{3+}	La-SS	EG	Ln chlorides
GdF_3:20%Yb^{3+},2%Tm^{3+}	Gd-SS	EG	Ln chlorides
LaF_3	La-HS-1	water	La nitrates
GdF_3	Gd-HS-1	water	Gd nitrates
LaF_3	La-SS-nitrates-1	EG	La nitrates
LaF_3	La-SS-1	EG	La chlorides
GdF_3	Gd-SS-1	EG	Gd chlorides

Synthesis of ternary fluoride UCNPs

The HS of the $NaYF_4$ UCNPs, codoped with 3.33 at.% Yb^{3+} and 0.33 at.% Tm^{3+} (NaY-HS samples, Table 3.2) was carried out as described in detail elsewhere [148]. In short, 2 mmol of Ln nitrates in a stoichiometric ratio were dissolved in 9 ml of deionized water. This solution was admixed to an 18 ml aqueous solution containing 8 mmol Na_3Cit (the molar ratio of Cit:Ln^{3+} was 4:1). The Na_3Cit was prepared by dissolving a stoichiometric ratio of NaOH and CA in deionized water. After vigorous stirring for 30 min, 27 ml of aqueous solution containing 25 mmol of NaF was admixed to the above solution and transferred into a 70-ml-Teflon vessel in a stainless-steel autoclave, and heated at 3 °C/min to 180 °C with a soaking time of 1–20 hours (Table 3.2). As the autoclave was cooled to room temperature naturally, the precipitates were separated by centrifugation at 5000 rpm for 5 min, washed with ethanol and deionized water and then dried in air or kept in a water suspension.

Modified thermal decomposition synthesis (TS) of β-$NaYF_4$ UCNPs, co-doped with 3.33 at.% $Yb^{3+}$and 0.33 at.% Tm^{3+} (NaY-TS) was based on ref. [23] using some

modifications (Table 3.2). 12 ml of OA and 30 ml of ODE were added to 2 mmol of stoichiometric amounts of Ln chlorides in a 100 ml flask. The solution was heated to 156 °C for 30 min to form yellow transparent solution and then cooled to ~70 °C. A solution of NH_4F (8 mmol) and NaOH (5 mmol) in 10 ml of methanol was added slowly to the above. Reaction mixture became turbid and was stirred at 50 °C for 40 min. After the evaporation of methanol, the solution was heated to 300 °C in an Ar atmosphere for 1.5 h and then cooled naturally to room temperature. The as-synthesized NaY-TS UCNPs were precipitated with the addition of acetone, collected after centrifugation (at 5000 rpm for 5 min), washed with ethanol to remove the excess of OA and with deionized water to remove NaCl. Finally, they were dispersed in a non-polar solvent (cyclohexane or chloroform). Oleate-capped as-synthesized NaY-TS UCNPs were transferred from cyclohexane/chloroform into water through a modified ligand-free protocol using some modifications [149]. The dried OA-coated NaY-TS UCNPs were immersed in 0.1 M HCl (10 mL, pH = 1). The mixture was sonificated in ultrasound bath for about 3 h while maintaining the pH value of 1 by adding 0.1 M HCl every 30 min. After the completion of this process, the aqueous solution was mixed with DE to extract OA. The procedure was repeated several times until the solution became almost transparent. The bare NaY-TS UCNPs in water were recovered by centrifugation at 5000 rpm for 5 min after precipitation with acetone and additionally washed with water. Bare NaY-TS UCNPs were collected from water by a sedimentation using an ultracentrifuge (10000 rpm, 5 min), followed by a decantation, and were dried at 70 °C for 3 h.

Synthesis with coprecipitation under reflux (R) of α-$NaYF_4$ UCNPs co-doped with 3.33 at.% $Yb^{3+}$and 0.33 at.% Tm^{3+} (NaY-R) was applied similar as in ref. [35]. 1 mmol of stoichiometric amounts of Ln nitrates were added to 30 ml of EG to dissolve the obtained precursors. NaCl (1 mmol) was subsequently added and the solution was heated to 80 °C until a homogeneous solution was formed. NH_4F (4 mmol) was dissolved in 20 ml of EG at 80 °C and added dropwise to the previous solution, which was maintained at 80 °C for 10 min under stirring. The mixed solution was heated to 160 °C under reflux for 2 h and then cooled to room temperature naturally. The product was isolated by centrifugation and washed twice with absolute ethanol and twice with deionized water. NaY-R@PVP UCNPs were synthesized in the same way as NaY-R UCNPs, only PVP was added during synthesis. NaY-R@PVP UCNPs were further coated with silica coating, as described below.

Table 3.2: Synthesis parameters for ternary fluoride UCNPs.

Ternary fluoride UCNPs	T (°C)	t (h)
NaY-HS-20	180	20
NaY-HS-10	180	10
NaY-HS-1	180	1
NaY-TS	300	1.5
NaY-R	160	2
NaY-R@PVP	160	2

A typical procedure [35] for the coating of silica onto the NaY-R@PVP UCNPs was applied (Figure 3.1). As-synthesized NaY-R@PVP UCNPs were dispersed in ethanol

(20 ml) and mixed with water (4 ml) and ammonia solution (0.6 ml, 25 %). Tetraethoxysilane (TEOS, 0.2 ml) dissolved in 10 ml of ethanol was then added slowly to the solution with continuous stirring. The product NaY-R@SiO_2 UCNPs were isolated by centrifugation and washed twice with ethanol and water.

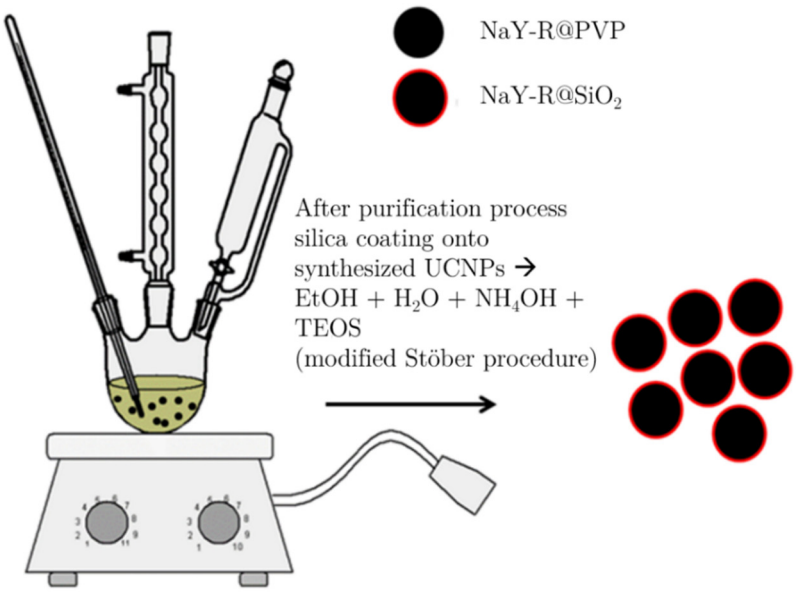


Figure 3.1: Schematic presentation of synthesis of NaY-R and NaY-R@PVP UCNPs followed by coating with silica.

3.2.2 Coating of NaY-TS UCNPs with Amphiphilic Polymers and Preparation of Their Stable Suspensions in Water

Amphiphilic co-polymers PMAO-BMHT

The transfer of hydrophobic OA-coated NaY-TS UCNPs into water, using co-polymers PMAO and BHMT, was based on refs. [19] and [150] using some modifications (Figure 3.2). Stable suspension of OA-coated as-synthesized NaY-TS UCNPs in chloroform (~12 mg/ml) was diluted to 0.12 mg/ml NaY-TS UCNPs. Afterwards, a solution of polymer PMAO in chloroform (c = 0.137 M) was added to the diluted suspension of OA-coated NaY-TS UCNPs with a ratio between the monomer units per nm^2 of UCNPs' surface equal to 300. After 2 h of agitation, a cross-linker BHMT in chloroform was added (c = 0.02 M). The ratio between BHMT molecules per nm^2 of UCNPs surface was equal to 10. The solution was mixed additionally for 0.5 h. After mixing, chloroform was evaporated and thin film of NaY-TS@PMAO-BHMT UCNPs, formed on the walls of the beaker, suggested on the total removal of chloroform. To this thin film 20 ml of deionized water was added together with 0.5–1 ml 1 M NaOH and the mixture was sonificated for 2 h. At first, large aggregates were eliminated from the mixture and the suspension with excess of co-polymer BHMT-PMAO and smaller aggregates was centrifuged at 5000 rpm for 5 min. Supernatant was carefully removed and centrifuged until the supernatant was transparent. This indicated a stable suspension of NaY-TS@PMAO-BMHT UCNPs.

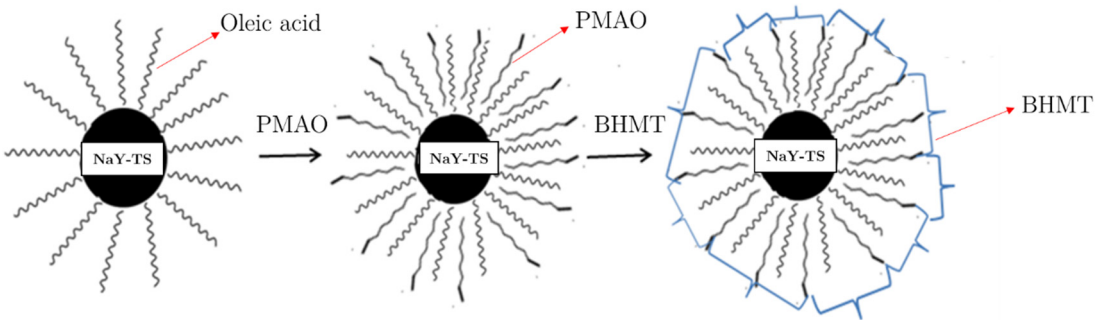


Figure 3.2: Schematic presentation of the coating process. As-synthesized NaY-TS UCNPs are coated with an amphiphilic polymer PMAO and a cross-linker BHMT.

Amphiphilic polymer TPGS

Surface modification of OA-coated as-synthesized NaY-TS UCNPs, stable in cyclohexane, was performed similar as in references [20], [80] but using some modifications. 20–30 mg of OA-coated NaY-TS UCNPs was added to excessive amount of polymer TPGS (~ 100 mg), which was dispersed in 10 ml of cyclohexane. TPGS was dispersed in cyclohexane by stirring for 1 h, forming a milky emulsion. After adding the OA-coated NaY-TS UCNPs in cyclohexane, the mixture was additionally stirred for 0.5 h, and then sonificated for 20 min to form a clear solution. To this solution, 20 ml of deionized water was added, which was sonificated again for 20 min to form a white water-in-oil emulsion. The water and oil phase were separated by a centrifugation at 5000 rpm for 5 min. The water phase was carefully separated from the oil phase and centrifuged again. The supernatant with NaY-TS@TPGS UCNPs (optically transparent) was transferred to a flask and dried at 70 °C for 15 min to remove the residual cyclohexane.

3.2.3 Dissolution Study

The dissolution analyses of binary UCNPs and ternary fluoride UCNPs (samples NaY-HS and NaY-TS) were performed from three-days old aqueous suspensions. UCNPs were aged in deionized water at room temperature (RT). Other samples were aged in the PBS at pH = 7.4 with a defined concentration of UCNPs at different temperatures from 15 min to 2 days (Table 3.3). The suspensions were kept in closed vials for the RT experiments while for aging at higher temperatures (i.e., 37 or 50 °C) they were maintained in a water bath. Three parallel samples were analysed for the statistics. The solutions for the dissolution analyses were prepared by a centrifugation of the suspensions at 5000 rpm for 5 min to remove the majority of the UCNPs, followed by an ultrafiltration (using a MW 30kDa filter) to eliminate any remaining UCNPs from the solution.

Table 3.3: Parameters of the dissolution study. RT denotes room temperature (20–25 °C).

UCNPs	Aqueous media	pH	T (°C)	Aging time
La,Gd-HS	Deionized water	~ 5–7	RT	3 days
La,Gd-SS				
La-SS-nitrates				
NaY-HS-1	Deionized water	~ 5–7	RT	3 days
NaY-HS-10				
NaY-HS-20				
NaY-TS	Deionized water	~ 5–7	RT	3 days
	PBS	7.4	37	2 days
		7.4	50	2 days
NaY-R	PBS	7.4	RT	15min–2days
		7.4	37	2 days
		7.4	50	2 days
NaY-R@PVP	PBS	7.4	RT	15min–2days
NaY-R@SiO_2	PBS	7.4	RT	15min–2days
NaY-TS-1@PMAO-BHMT	PBS	7.4	37	2 days
NaY-TS-2@TPGS	PBS	7.4	37	2 days

3.2.4 Characterization Techniques

3.2.4.1 UCNPs Characterization

The crystal structure of synthesized UCNPs was verified by X-ray diffraction (XRD) with an X-ray diffractometer (Philips X'Pert PRO MPD Diffractometer, PANanalytical with CuKα radiation, $\lambda_{CuK\alpha 1}$=1.5406 Å). Morphology of the UCNPs was inspected with a transmission electron microscope (TEM, Jeol 2100). TEM samples were prepared by dropping a diluted dispersion of UCNPs onto a copper grid. The equivalent diameters of the UCNPs were determined from their surfaces using Gatan Digital Micrograph Software. A minimum of ~150 UCNPs per sample was accounted for statistics. An energy dispersive X-ray spectroscopy (EDXS) and selected area electron diffraction (SAED) were also

performed during TEM analyses. The particles were also observed with a scanning electron microscope (SEM). For the SEM analysis the material was deposited on a graphite specimen mount. The field fluorescence electron source SEM (JEOL 7600F) was operated at 15 kV. Thermogravimetric (TG) analyses for determination of PMAO-BHMT and TPGS amount were performed on a Jupiter 449 simultaneous thermal analysis (STA) instrument with a heating rate of 3 °C/min in an O_2/Ar (40/10) atmosphere using a TG/DTA sample holder and Al_2O_3 crucibles. Attenuated total reflectance (ATR) measurements were performed on ATR-FTIR device (Dura Sample IR – Technologies Dunbury, ZDA). The surface chemistry of the unaged and aged UCNPs was analysed with X-ray photoelectron spectroscopy (XPS) on the PHI-TFA XPS spectrometer produced by Physical Electronics Inc. The analyzed area was 0.4 mm in diameter and the analyzed depth was about 3–5 nm. Sample surfaces were excited by X-ray radiation from monochromatic Al source at photon energy of 1486.6 eV. Quantification of surface composition was performed from XPS peak intensities taking into account relative sensitivity factors provided by the instrument manufacturer [151].

3.2.4.2 Suspension Characterization

The aqueous suspensions were characterized with electrokinetic measurements of the zeta (ζ)-potential (ZetaPALS Zeta Potential Analyser, Brookheaven Instruments Corporation). Ten measurements (10 cycles per measurement) were made at a particular pH. The pH values were adjusted with HCl or NaOH. Hydrodynamic particle size was analysed using dynamic light scattering (DLS, Fritsch, Analysette 12 DynaSizer). The concentration of UCNPs in suspension was determined thermogravimetrically. The solvent was evaporated at 70 °C during the night and the organic species (CA, OA, PVP, TPGS, PMAO-BHMT) were decomposed during the heating (3 °C/min) to 600 °C with a holding time of 2 h.

An Orion 960 Autochemistry System with a temperature sensor and a combined fluoride ion selective electrode (Thermo, Orion model 96-09) was used for a potentiometric determination of the fraction of dissolved F^- using the multiple known addition method with a blank subtraction [152]. The concentration of the fraction of dissolved cations (Yb^{3+}, Tm^{3+}, Y^{3+} and Na^+) was determined with ICP-OES.

3.2.4.3 Optical Properties

Photofluorescence of the UCNPs was characterized for irradiation with a continuously emitting 978 nm diode laser (MDL-III by CNI, Changchun, China). Focusing of the laser beam with average power of 2 W produced an irradiant power density of ~160 J/cm^2. The resulting UC fluorescence was collected at an angle of ~90° angle with respect to the beam axis and analyzed using a compact diffraction spectrometer (USB4000, Ocean Optics, Dunedin, FL) in the 400–900 nm spectral range.

The downconversion (DC) fluorescence decay kinetics of the Yb^{3+} sensitizer's fluorescence at 980 nm upon excitation with 940 nm were carried out with a commercial Edinburgh Instruments spectrofluorometer FSP-920 equipped with a μ-flash lamp 920H (pulse width 3 μs). UC emission spectra of unaged and aged UCNPs of the same sizes were recorded on spectrofluorometer FSP-920 using a 1 W 980 nm laser diode for sample excitation.

Chapter 4

Results

The aim of this thesis was to study the dissolution of fluoride UCNPs in aqueous suspensions in correlation to their chemical stability. Since the dissolution process can also induce different structural defects and changes of the crystal field of the Ln^{3+} ions, the influence of dissolution on the optical properties of fluoride UCNPs was also studied. The dissolution of fluoride UCNPs should be minimized or prevent if they were to be used in medical diagnostics. Therefore, different protective coatings against the dissolution of UCNPs were tested.

4.1 Fluoride UCNPs and Their Dissolution in Aqueous Systems

4.1.1 Dissolution of Binary Fluoride UCNPs in Water

The dissolution of binary fluoride UCNPs with two different compositions, i.e., LaF_3 and GdF_3, codoped with Yb^{3+} and Tm^{3+}, synthesized hydrothermally (HS samples) or solvothermally (SS samples), was investigated.

XRD patterns (Figure 4.1) of La-based and Gd-based UCNPs are in agreement with the hexagonal structure of LaF_3 (JCPDS 32-0483; space group P3c1) and orthorhombic structure of GdF_3 UCNPs (JCPDS 12-0788; space group Pnma), respectively. No secondary phase was detected in the XRD patterns, revealing that Yb^{3+}/Tm^{3+} were effectively incorporated into the host lattices of LaF_3 or GdF_3.

Table 4.1: Structural and morphological properties of binary fluoride UCNPs and the pH values of the aged suspensions with the fraction of dissolved F^-.

UCNPs	Crystal structure of UCNPs	d(XRD) (nm)	d(TEM) (nm)	Morphology of UCNPs	pH of the aged suspensions	Fraction of dissolved F^- (mol.%)
La-HS	hexagonal	20 ± 2	20±5	Elongated UCNPs	~6.2	0.65 ± 0.01
La-SS	hexagonal	12 ± 5	13±3	Interconnected to each other	~5.2	1.16 ± 0.05
La-SS-nitrates	hexagonal	11 ± 2	11±2	Elongated UCNPs	4–6	2.5 ± 0.1
Gd-HS	orthorombic	35 ± 4	(63±17)×(36±10)	Elongated UCNPs	~5.4	0.30 ± 0.01
Gd-SS	orthorombic	19 ± 2	(48±15)×(24±7)	Elongated UCNPs	~4.5	0.30 ± 0.02

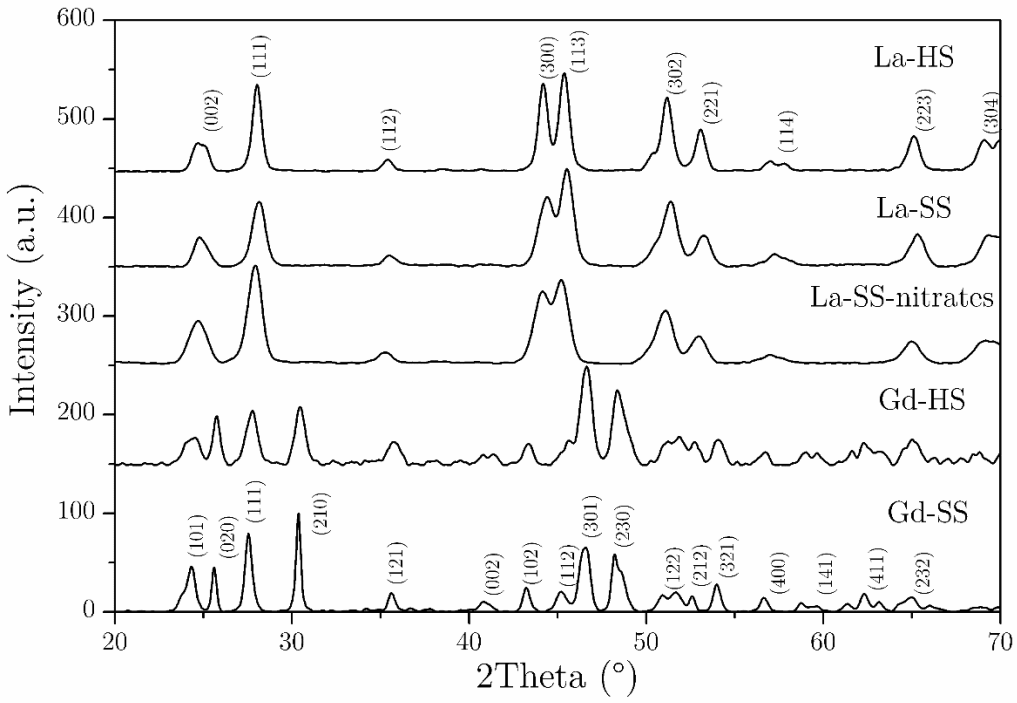


Figure 4.1: XRD patterns of the as-synthesized binary fluoride UCNPs. The incides for La-based UCNPs correspond to LaF_3 (JCPDS 32-0483, space group P3c1) and for Gd-based UCNPs correpond to GdF_3 (JCPDS 12-0788, space group: Pnma).

The effect of doping of LaF_3 and GdF_3 UCNPs with Yb^{3+} and Tm^{3+} can be also seen from the parameters of their crystal lattices, which were different for the doped and undoped UCNPs (Table 4.2). While a contraction of the cell volume was observed for all La-based UCNPs, this was not significant for the Gd-based UCNPs. Nevertheless, a decrease of the a-parameter was observed for both Gd-based samples. This phenomenon can be explained by the incorporation of the Yb^{3+} (87 pm) and Tm^{3+} (88 pm) that are smaller than La^{3+} (103 pm) or Gd^{3+} ions (94 pm) [153]. The synthesis procedure did not significantly influence the variation of the cell parameters of La or Gd-based UCNPs.

Table 4.2: Crystal cell parameters for undoped NPs and doped UCNPs.

Undoped NPs	La-HS-1	La-SS-1	La-SS-nitrates-1	Gd-HS-1	Gd-SS-1
	a=7.186(1) Å c=7.354(1) Å V=0.3289 nm^3	a=7.38(1) Å c=7.57(1) Å V=0.357 nm^3	a=7.178(1) Å c=7.356(1) Å V=0.328 nm^3	a=6.56(1) Å b=6.99(1) Å c=4.41(1) Å V=0.202 nm^3	a=6.567 (1) Å b=6.992 (1) Å c=4.394 (1) Å V=0.202 nm^3
Doped UCNPs	La-HS	La-SS	La-SS-nitrates	Gd-HS	Gd-SS
	a=7.12(1) Å c=7.27(1) Å V=0.319 nm^3	a=7.11(1) Å c=7.26(1) Å V=0.317 nm^3	a=7.11(1) Å c=7.28(1) Å V=0.319 nm^3	a=6.494(1) Å b=6.952(1) Å c=4.421(1) Å V=0.199 nm^3	a= 6.508 (1) Å b=6.956 (1) Å c=4.402 (1) Å V=0.199 nm^3

TEM studies showed that the La-HS UCNPs, synthesized in water, were of irregular shape and their sizes were around 20 nm (Table 4.1, Figure 4.2a). Morphology of La-SS UCNPs was similar to La-HS UCNPs, their sizes were around 13 nm (Figure 4.2b). Gd-HS UCNPs were composed of small elongated NPs with lengths of around 63 nm (Figure 4.2c). They were aggregated into larger ellipsoidal aggregates with lengths of around 500 nm. Gd-SS UCNPs also had elongated shape lengths of around 50 nm (Figure 4.2d).

XRD analyses using the Pawley method [154] showed that the crystal size of La-HS UCNPs was around 20 nm, while for La-SS UCNPs it was 12 nm and for La-SS-nitrates UCNPs 11 nm (Table 4.1). The crystal size of Gd-HS was 35 nm and 19 nm for Gd-SS UCNPs. Crystallite sizes of La-based UCNPs are in good agreement with TEM results (Table 4.1). However, for the Gd-based UCNPs the difference between diameters is observed. This can be attributed to the Pawley method, which assumes a spherical shape of crystallites. As seen in Figure 4.2c,d, this was not so for the Gd-based UCNPs.

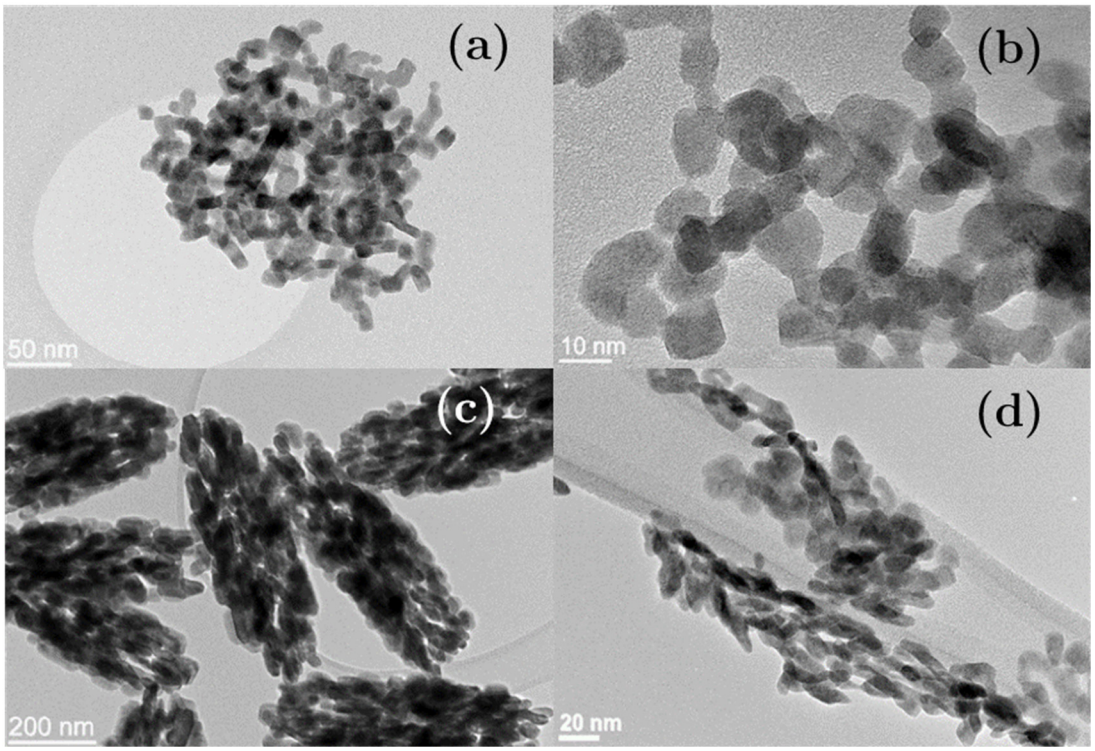


Figure 4.2: TEM images of La-HS (a), La-SS (b), Gd-HS (c) and Gd-SS (d) UCNPs.

The incorporation of Yb^{3+} and Tm^{3+} into a host lattice was additionally confirmed with a typical fluorescence emission for Tm^{3+}. As an example we present UC emission spectrum of La-HT UCNPs (Figure 4.3). Peaks around 450 ($^1D_2$ → $^3F_4$) and 475 nm ($^1G_4$→$^3H_6$) are attributed to blue emission, while peaks at around 650 nm ($^1G_4$→$^3F_4$) and 700 nm ($^3F_3$→$^3H_6$) can be assigned to red emission. The most intense emission is observed in NIR at around 800 nm ($^3H_4$→$^3H_6$).

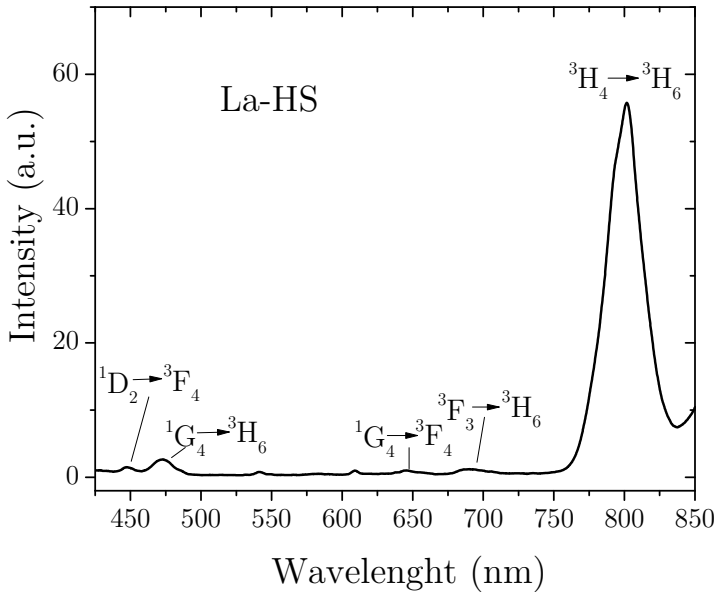


Figure 4.3: UC spectra of La-HS UCNPs suspension in water with $c = 13.6$ mg/ml.

The binary fluoride UCNPs were aged in water at RT for 3 days in weakly acidic pH in the range ~4–6. The fraction of dissolved F^- was lower for the Gd-based UCNPs than for the La-based UCNPs, whether they were synthesized hydrothermally or solvothermally (Table 4.1). This can be attributed to the smaller particles sizes of the La-based UCNPs. Similar to this, the highest fraction of dissolved F^-, among La-based UCNPs, was determined for the smallest La-SS-nitrates (11nm) UCNPs, 2.5 mol.%, while for the largest La-HS UCNPs (20 nm) only 0.65 mol.% of F^- was dissolved.

Although these results were only preliminary, they stimulated a more comprehensive investigation of the dissolution of ternary fluoride UCNPs in aqueous systems.

4.1.2 The Dissolution of $NaYF_4$ UCNPs in Water

$NaYF_4$ was selected for further studies as the most studied host matrix for UCNPs [23]. In this work, the attention was paid to the dissolution of α-$NaYF_4$ with cubic structure in comparison to the β-$NaYF_4$ with hexagonal structure. Hydrothermally synthesized α- $NaYF_4$ UCNPs (NaY-HS) and β-$NaYF_4$ UCNPs, synthesized with modified thermal decomposition (NaY-TS) were aged for 3 days at RT in weakly acidic aqueous suspensions.

Under hydrothermal conditions, $NaYF_4$ crystallizes in a metastable cubic (α) structure and it transforms into a thermodynamically stable hexagonal (β) structure after using severe experimental conditions, such as high-temperature and longer reaction times [148]. The phase evolution process during the HS synthesis was examined within a reaction time of 1–20 h at a temperature of 180 °C (Table 4.3, Figure 4.4). The samples obtained after a 1, 10 and 20 h of reaction time (NaY-HS-1, NaY-HS-10, NaY-HS-20) showed a cubic, α- $NaYF_4$ structure (JCPDS 77-2042, space group Fm3m) (Figure 4.4). In contrast to the HS samples, a pure β-$NaYF_4$ phase was obtained with the modified thermal decomposition synthesis (NaY-TS in Figure 4.4).

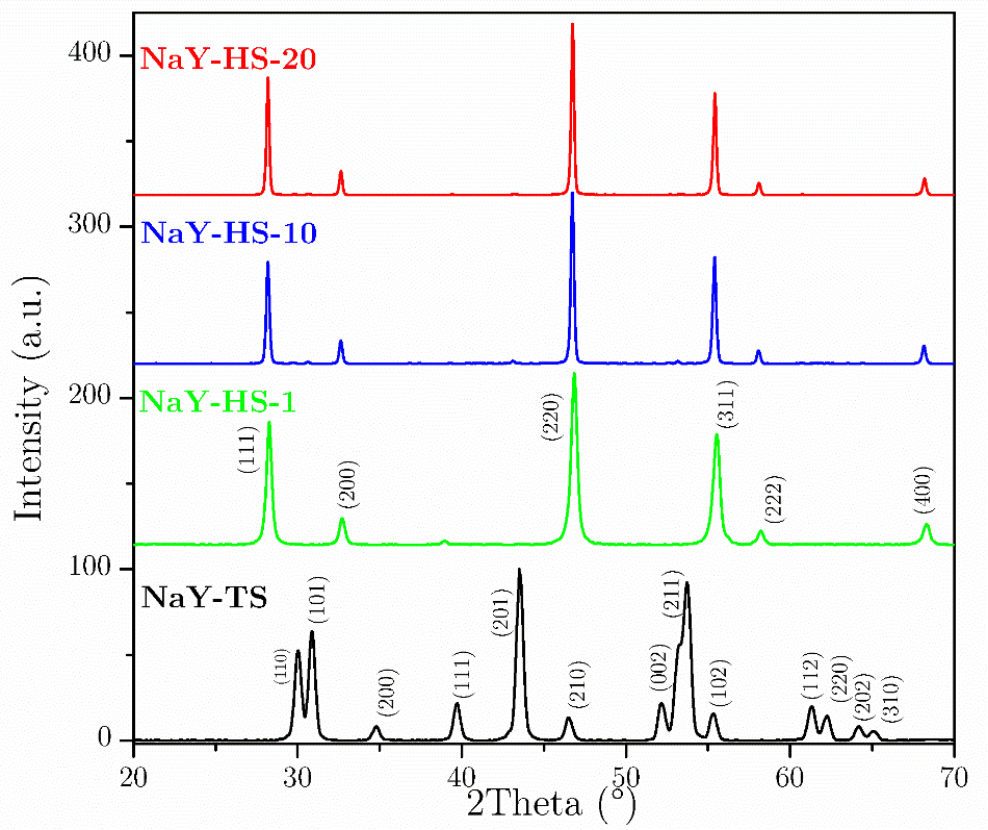


Figure 4.4: XRD patterns of the as-synthesized UCNPs. The indices correspond to β- $NaYF_4$ (JCPDS 16-0334, space group P63/m for NaY-TS sample) and α-$NaYF_4$ (JCPDS 77-2042, space group Fm3m for the NaY-HS samples) [155].

Table 4.3: Structural and morphological properties of fluoride UCNPs, and pH values of the aged suspensions with the fraction of dissolved ions [155].

UCNPs	Crystal structure	Crystallite size (nm)	UCNPs size (nm)	Morphology	pH of analysed suspension	Fraction of the dissolved ions (mol.%)
NaY-HS-20	α-$NaYF_4$	120±10	1135±25	Anisotropic, truncated, cube-like morphology	4–6	Na:6.30 ± 0.02
						Y:0.52 ± 0.01
						Yb:1.15±0.01
						Tm:1.00±0.03
						F:1.10±0.01
NaY-HS-10	α-$NaYF_4$	94±5	160±13	Quasi-spherical	4–6	Na:5.00±0.02
						Y:0.17±0.01
						Yb:0.50±0.01
						Tm:1.02±0.02
						F:0.85±0.01
NaY-HS-1	α-$NaYF_4$	80±4	103±10	Quasi-spherical	~6.3	Na:5.40±0.03
						Y:0.19±0.01
						Yb:0.21±0.02
						Tm:0.34±0.04
						F:0.94±0.02
NaY-TS	β-$NaYF_4$	30±1	21±3	Quasi-spherical	4–5	Na:2.33±0.11
						Y:0.08±0.01
						Yb:0.09±0.01
						Tm:0.19±0.05
						F:0.39±0.11

TEM images (Figure 4.5) show differences in the morphologies between the different UCNPs. The NaY-HS-20 UCNPs have an anisotropic, truncated, cube-like morphology (Figure 4.5 and Figure 4.6) and they are of micron size. The NaY-HS-10 and NaY-HS-1 UCNPs are quasi-spherical with sizes of around 100–200 nm (Table 4.3, Figure 4.5). The NaY-TS UCNPs are quasi spherical and with a relatively homogeneous size of around 20 nm (Figure 4.5). The size distribution of the NaY-HS-10 and NaY-HS-1 UCNPs is broader than that of the NaY-TS UCNPs, while the largest size distribution was observed in the case of the NaY-HS-20 UCNPs. The EDXS analyses of the samples confirmed the presence of all the constituent elements, including a minor fraction of O. The latter may originate from the surface ligands (CA or OA). The incorporation of dopants (Yb^{3+}, Tm^{3+}) into the $NaYF_4$ matrix was also suggested by the UC fluorescence spectra (Figure 4.7).

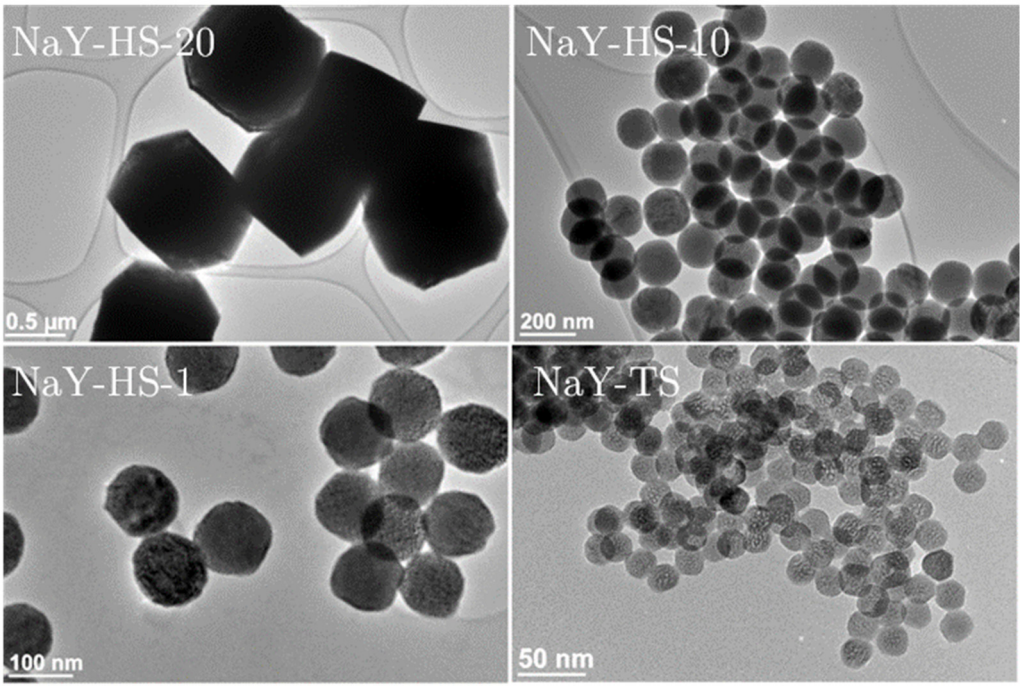


Figure 4.5: TEM images of the as-synthesized UCNPs [155].

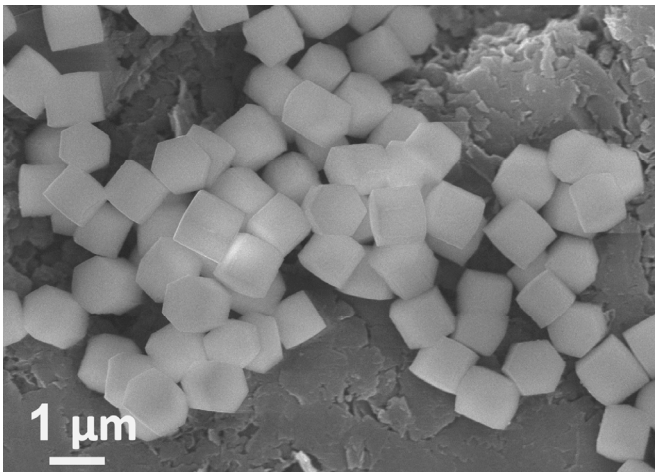


Figure 4.6: SEM image of NaY-HS-20 UCNPs [155].

The characteristic emission peaks of the Tm^{3+} ions for NaY-HS UCNPs and NaY-TS UCNPs are clearly observed in Figure 4.7. The dominant emission peak is in the NIR region, at 800 nm, which can be attributed to the electronic transition from $^3H_4$ to $^3H_6$. Six individual transitions can be distinguished within the emission band at 800 nm, with peaks at 770, 782, 793, 800, 817, and ~834 nm. The strongest NIR emission at 800 nm was observed for the NaY-TS UCNPs and among the NaY-HS samples for the NaY-HS-20 UCNPs. For NaY-HS-20 UCNPs, only three of the above mentioned transitions are observed, with the 800 nm peak dominating over the peaks at 872 nm and 817 nm. Similar was true for the NaY-HS-1, while the NaY-HS-10 showed a dominant emission at 817 nm. The superior UC emission of the NaY-HS-20 UCNPs, when compared with other HS

samples, can be attributed to the largest particle sizes (Table 4.3) and thus the lowest surface-to-volume ratio. NaY-TS and NaY-HS-20 UCNPs also showed a weaker blue emission at 450 and 475 nm, which can be attributed to the electronic transition from $^1D_4$ to $^3F_6$ and $^1G_4$ to $^3H_6$, respectively. Other weak peaks at 642 nm and ~700 nm can be assigned to the electronic transition of $^1G_4$ to $^3F_4$ and $^3F_3$ to $^3H_6$, respectively. Minor peaks at 582 nm and 657 nm were observed only for the HS samples and can be attributed to impurities, originating from the reagents [155].

A significant difference of the emission peak at 800 nm between the NaY-HS and NaY-TS UCNPs is seen in Figure 4.7. The peak is narrower with higher emission intensity for the NaY-TS UCNPs than for the HS samples. The different shape of the peak can be assigned to different crystal structure and, in part, also to different surface composition (see below).

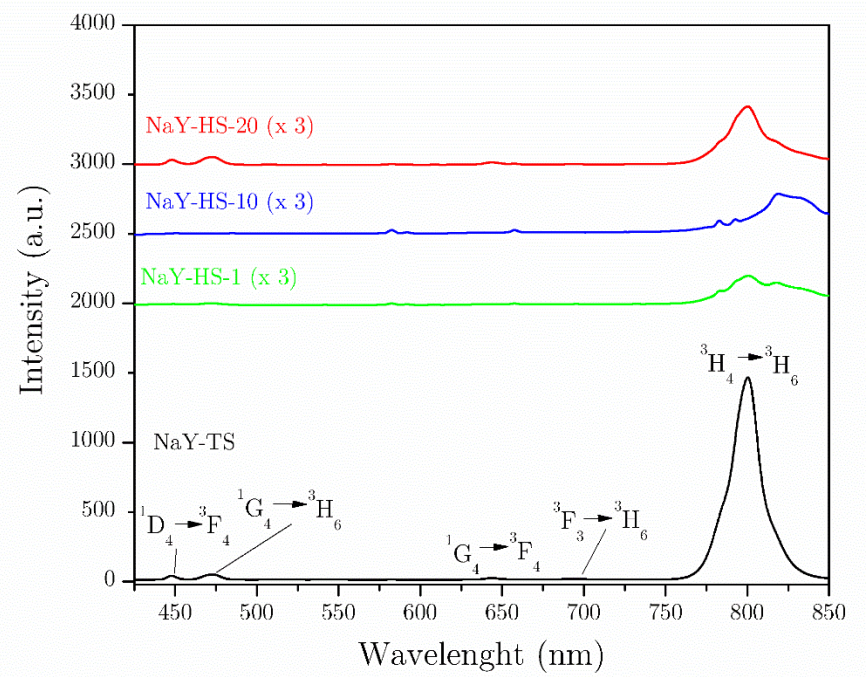


Figure 4.7: UC emission spectra of UCNPs in aqueous suspensions. In order to make the weak fluorescence peaks of the HS samples more easily seen, their spectra were multiplied by a factor of 3 [155].

In order to understand the possible effect of the surface chemistry on the optical properties of studied ternary fluoride UCNPs, XPS surface analyses of NaY-HS-1 and NaY- TS UCNPs was done. Both of the UCNPs had nominal composition $NaY_{0.78}Yb_{0.2}Tm_{0.02}F_4$. For easier comparison and interpretation, the nominal composition ($Na_{1.3}Y_1Yb_{0.26}Tm_{0.026}F_{5.13}$) and the surface compositions of studied UCNPs were normalized to Y=1. For NaY-HS-1 UCNPs normalized surface composition was $Na_{0.29}Y_1Yb_{0.08}F_{2.24}O_1$ and for NaY-TS UCNPs was $Na_{0.58}Y_1Yb_{0.24}F_{2.96}O_{0.47}$. All the constituent elements were detected at UCNPs surface together with C and O (Figure 4.8). An exception was Tm^{3+}, which could not be detected due to its low concentration. Some C concentration is typically detected in any sample and results from the specific nature of the method. However, C can be also originate from the surface ligands (CA in NaY-HS-1 and remaining OA in NaY-TS). The comparison of the normalized nominal and surface compositions revealed that the surfaces of both samples contain a substoichiometric ratio of Na versus Y. An almost stoichiometric ratio of Y versus Yb was determined on the surfaces of NaY-TS UCNPs,

while in the case of NaY-HS-1 UCNPs ratio Y versus Yb is larger. Substoichiometric ratio of F versus Y was detected on the surface of both samples, with a slightly lower value for the NaY-HS-1 UCNPs. A significant fraction of O was detected on the UCNPs. Part of this O can be attributed to the surface ligands, CA in the NaY-HS-1 and OA in NaY-TS. However, there is a significantly larger fraction of O on the surface of NaY-HS-1 UCNPs (16.9 at.%) in comparison to NaY-TS UCNPs (4.7 at.%). This fact can be correlated to the poorer optical properties of NaY- HS- 1 UCNPs with a cubic crystal structure (Figure 4.7).

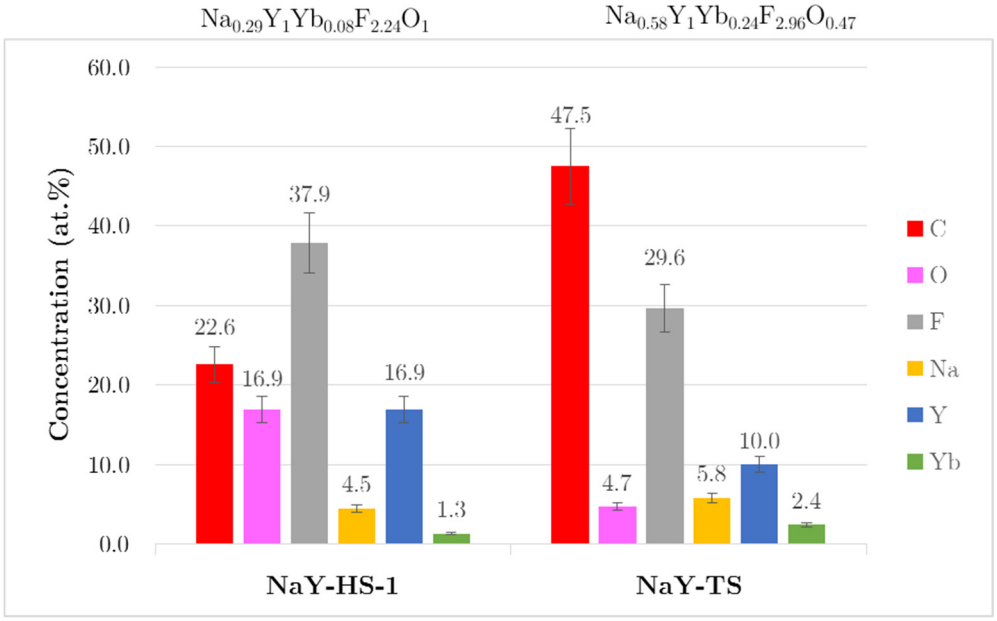


Figure 4.8: NaY-HS-1 and NaY-TS UCNPs with their respective surface composition given in at.%. The relative error in concentration was estimated to be about 10 %. The normalized surface compositions with respect to Y are written on the top.

All UCNPs from Table 4.3 were aged for 3 days at RT in weakly acidic aqueous suspension, similar as binary fluoride UCNPs (Section 4.1.1). The dissolved F^-, Y^{3+}, Ln (Yb^{3+} and Tm^{3+}) and Na^+ ions were detected in suspensions. There was no significant difference in the concentration of the fraction of dissolved F^- among NaY-HS samples. However, the fractions of dissolved Ln^{3+} ions were larger in NaY-HS-20 than in the other two HS samples. A significantly lower dissolution degree of all ions was measured for the NaY-TS UCNPs than for the NaY-HS UCNPs. This can be correlated to differences in their crystal structures and chemical composition of their surfaces. NaY-TS UCNPs with a stable hexagonal structure had a less defective surface composition than metastable cubic NaY-HS UCNPs (Table 4.3, Figure 4.4 and Figure 4.8).

4.1.3 Dissolution of $NaYF_4$ UCNPs at Simulated Physiological Conditions

The verification of the suitability of $NaYF_4$ UCNPs for biomedical applications also includes stability tests under physiological conditions, specific to their application, e.g., imitating the blood conditions (pH = 7.4 at 37 °C). In the following we present results on the dissolution of α-$NaYF_4$ and β-$NaYF_4$ UCNPs, aged in PBS with pH of 7.4 at RT, 37 °C and 50 °C. In both cases, $NaYF_4$ matrix was co-doped with Yb^{3+} and Tm^{3+}. Both types

of UCNPs were synthesized in non-aqueous media in order to prevent any potential dissolution in the mother solution during the synthesis.

4.1.3.1 α-$NaYF_4$ UCNPs

α-$NaYF_4$ UCNPs, co-doped with Yb^{3+} and Tm^{3+}, were synthesized with coprecipitation under reflux in EG (NaY-R UCNPs). The effect of surface modification with PVP (NaY-R@PVP UCNPs) and silica (NaY-R@SiO_2 UCNPs) on the dissolution was studied.

XRD analyses of all NaY-R samples (Figure 4.9) confirmed their cubic structure ($NaYF_4$, JCPDS 77-2042, space group Fm3m), regardless of the surface modification. Well defined peaks suggested high crystallinity of the UCNPs which was also confirmed with SAED (Inset in Figure 4.10a).

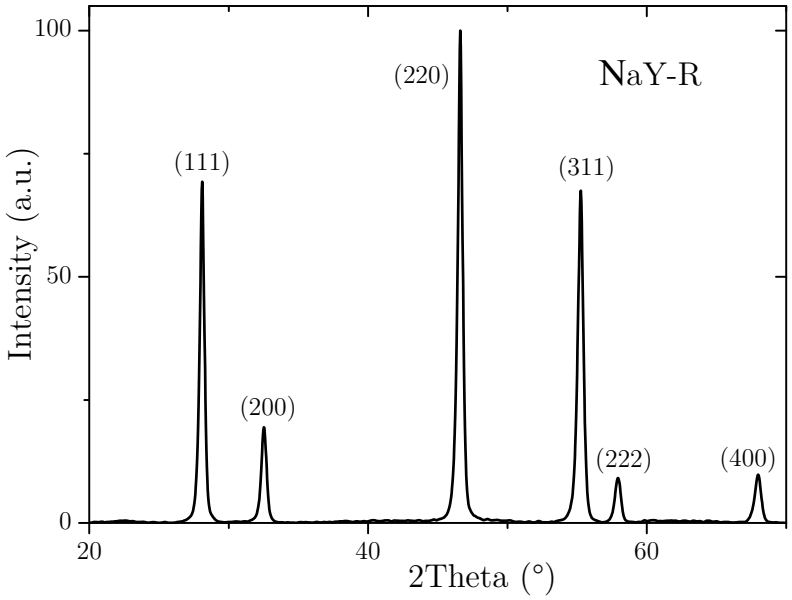


Figure 4.9: XRD patterns of NaY-R UCNPs. Indices correspond to JCPDS 77-2042, space group Fm3m.

As-synthesized NaY-R UCNPs were of irregular shape and aggregated (Figure 4.10a). Their size, determined with TEM analysis, was (33±5) nm, (Figure 4.10b). NaY-R UCNPs are typically stabilized with polymer PVP to enable a successful coating with silica using a modified Stöber procedure [31], [35], [67]. The addition of PVP did not significantly affect the morphology of NaY-R@PVP UCNPs (not shown here). In contrast to this, the formation of silica coating was clearly seen with TEM (Figure 4.11). NaY-R@SiO_2 UCNPs were uniformly coated with a silica layer with thickness of around 7–8 nm.

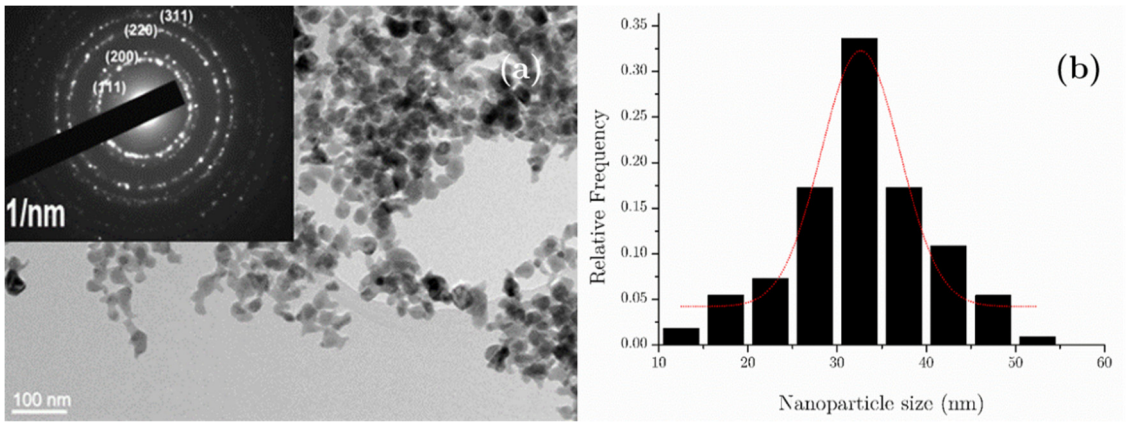


Figure 4.10: TEM image of the as-synthesized NaY-R UCNPs (a) with particle-size distribution (b), where red line represents a Gauss fit of relative frequency.

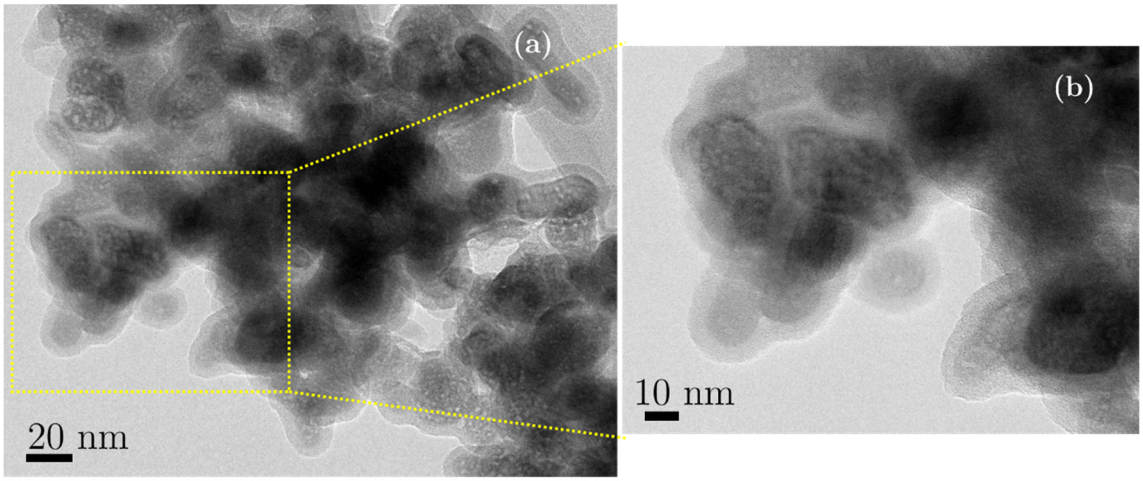


Figure 4.11: TEM images of NaY-R@SiO_2 UCNPs at lower (a) and higher magnification (b).

The effectiveness of the surface modification of NaY-R UCNPs was also verified with electrokinetic measurements of the zeta potential of the UCNPs in water (Figure 4.12). The zeta potential of NaY-R UCNPs was positive in the acidic pH range and negative in the basic pH range, with isoelectric point (IEP) at pH = 8. Similar zeta potential behaviour was determined for NaY-R@PVP, which suggests that PVP does not change the surface charge. However it allows for the steric stabilization of aqueous suspensions [68], [156]. Zeta potential of NaY-R@SiO_2 is negative in almost entire pH range (IEP at pH = 3) due to the negatively charged silanol groups from the silica coating.

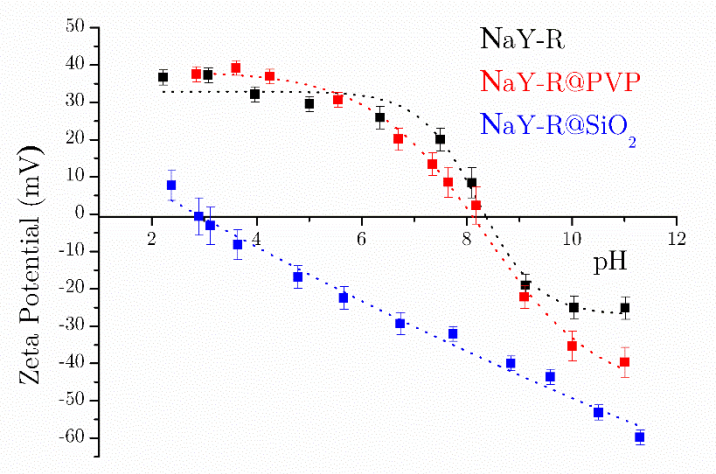


Figure 4.12: Zeta potential values versus pH for NaY-R, NaY-R@PVP and NaY-R@SiO_2 UCNPs dispersed in water.

UC emission spectra of NaY-R samples, dispersed in water, confirmed the successful incorporation of dopants into crystal lattice of α-$NaYF_4$ (Figure 4.13). The characteristics emission peaks of Tm^{3+} are clearly observed at around 475 nm (blue emission), 650 nm (red emission) and around 800 nm (NIR emission). The strongest NIR emission is observed in the case of NaY-R@SiO_2 UCNPs because silica layer protects against surface quenching [7],[19],[20]. The surface of UCNPs is protected with silica against the direct contact of Yb^{3+} and Tm^{3+} ions with OH^- ions from the water. The lowest NIR emission intensity was observed in the case of NaY-R@PVP UCNPs, suggesting that PVP with its pyrrolidone functional group may additionally quench the Tm^{3+} emission. Note that for the comparison of emission intensities and, subsequently for the dissolution studies, the fraction of the PVP (~10 %, calculated from TGA) in NaY-R@PVP UCNPs and of the silica in NaY-R@SiO_2 UCNPs (~50 %, approximated from spherical 33-nm sized UCNPs with a 7-nm tick silica layer) were taken into an account.

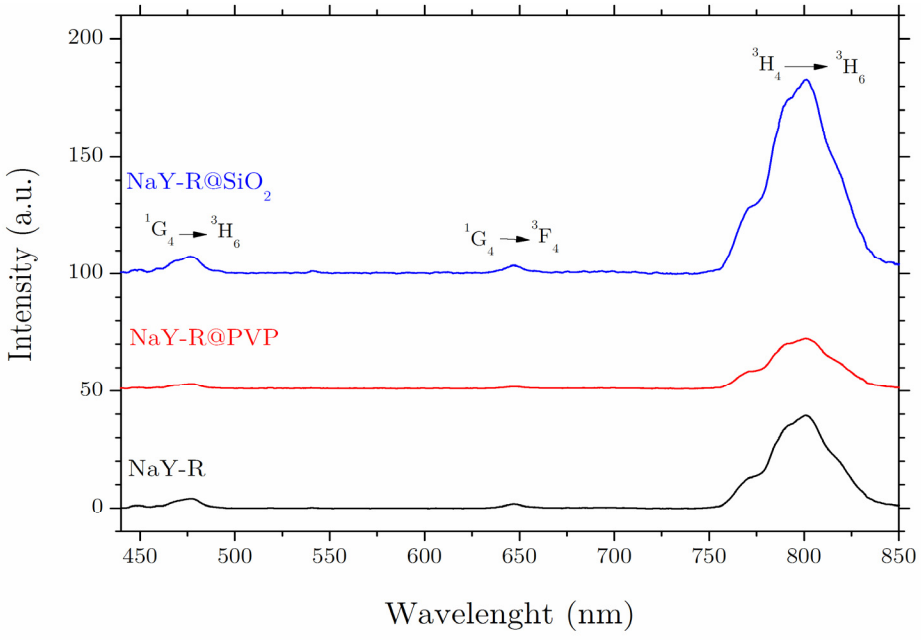


Figure 4.13: UC emission spectra of NaY-R UCNPs (c = 1 mg/ml) in water.

To further explain the surface effect on the measured UC emission (Figure 4.7 and Figure 4.13) additional surface analysis was done on NaY-R UCNPs and their surface composition is presented in Figure 4.14. Normalized surface composition (normalized to Y=1) of NaY-R UCNPs was $Na_{0.53}Y_1Yb_{0.21}F_{3.45}O_{0.32}$. Comparison of nominal surface composition with other UCNPs (Section 4.1.2, Figure 4.8) revealed that the surface composition of NaY-R is more similar to the surface composition of NaY-TS UCNPs ($Na_{0.58}Y_1Yb_{0.24}F_{2.96}O_{0.47}$) than to the surface composition of NaY-HS ($Na_{0.29}Y_1Yb_{0.08}F_{2.24}O_1$) In contrast to this, this was not so in the case of their optical properties. NaY-R and NaY-HS UCNPs showed similar UC emission spectra, which both differed from that of NaY-TS. Specifically, the splitting of the peak at 800 nm was observed in all NaY-R and NaY-HS samples but not in NaY-TS samples (Figure 4.7 and Figure 4.13). Therefore, we can assume that this difference originated from the different crystal structures and not from the different surface composition.

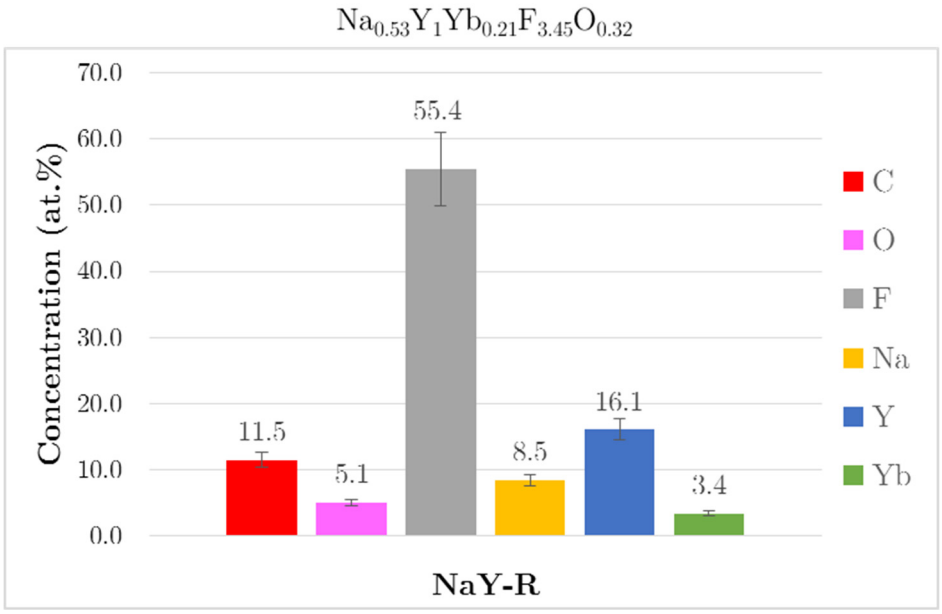


Figure 4.14: NaY-R UCNPs with their respective surface composition given in at.%.The relative error in concentration was estimated to be about 10 %. The normalized surface composition with respect to Y is written on the top.

In order to understand the effect of surface modification on the dissolution rate of NaY- R UCNPs, the dissolution at short aging times (i.e., 15, 60 and 120 min) and longer aging times (1–2 days) in PBS suspensions with pH = 7.4 at RT were studied. The main goal of this study was to investigate whether the silica coating prevents the dissolution of UCNPs. The dissolution of all samples, including the NaY-R@SiO_2 UCNPs, increases monotonously with time (Figure 4.15 and Figure 4.16). This is in accordance with the fact that silica is porous and, thus, it is impossible to prevent the contact of water molecules with the surface of NaY-R UCNPs. Nevertheless, the dissolution rate of NaY-R UCNPs and NaY-R@PVP UCNPs is higher than that of the NaY@SiO_2. This can also be inferred from the slope of linear fit at short aging times (Figure 4.16). We can conclude that the silica coating slows down the dissolution of UCNPs in PBS but it does not prevent it.

Surprisingly, NaY-R@PVP UCNPs dissolve more than NaY-R UCNPs at long aging times (Figure 4.15). One possible explanation could be that PVP with his carbonyl group coordinates with Ln^{3+} [31], [35], [68], which can accelerate the dissolution of UCNPs by the formation of stable complexes.

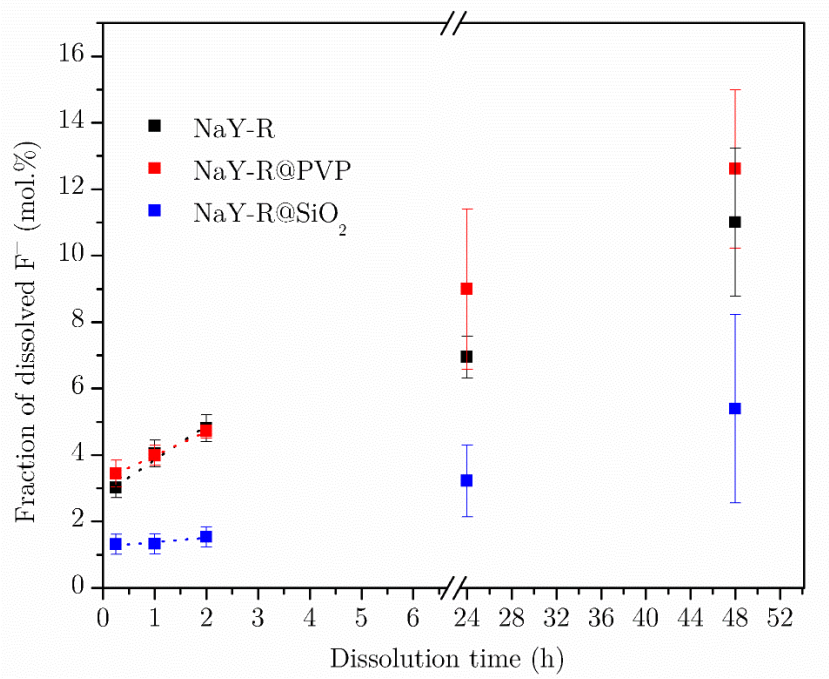


Figure 4.15: Dissolution of NaY-R, NaY-R@PVP and NaY-R@SiO_2 UCNPs.

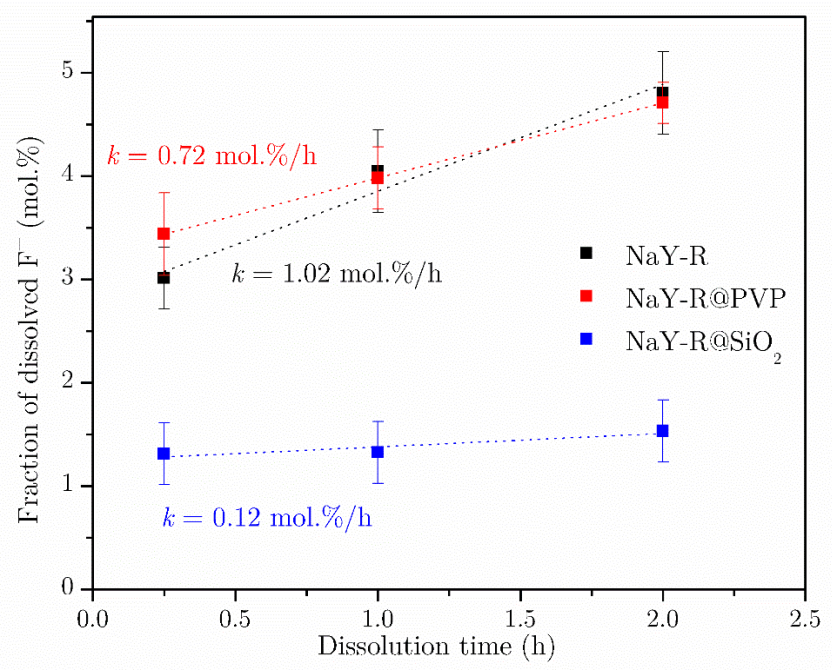


Figure 4.16: Dissolution of NaY-R, NaY-R@PVP, NaY-R@SiO_2 UCNPs at shorter aging times. Symbol k denotes the slope of the linear fit.

4.1.3.2 β-$NaYF_4$ UCNPs

β-$NaYF_4$ UCNPs with a hexagonal crystal structure provide a much higher efficiency of the UC process than their cubic (α-$NaYF_4$) counterparts [53] and are thus even more interesting for potential application as fluorescent biomarkers [157].

β-$NaYF_4$ UCNPs (NaY-TS) were synthesized with modified thermal decomposition synthesis (for basic properties see Section 4.1.2). As-synthesized NaY-TS UCNPs (Table 4.4) were uniform in size, monodispersed and non-agglomerated (Figure 4.17a). As-synthesized NaY-TS UCNPs were coated with OA and formed stable transparent suspensions in nonpolar solvents (e.g., cyclohexane, chloroform). All as-synthesized NaY-TS UCNPs were well crystallized, as suggested from XRD (Figure 4.4) and SAED (inset in Figure 4.17a). Detailed TEM analyses revealed that NaY-TS UCNPs have narrow size distribution (Figure 4.17b) but, the sizes of NaY-TS UCNPs varied between different syntheses batches (Table 4.4). This size difference may originate from the inability to control precisely the cooling from the reaction temperature.

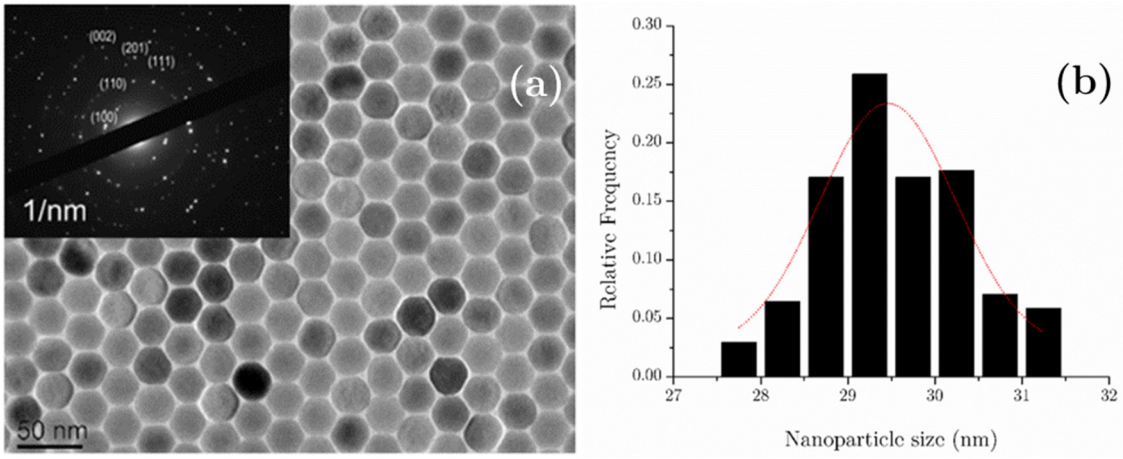


Figure 4.17: TEM image of the as-synthesized NaY-TS-B UCNPs (a) and particle size distribution (b). The SAED (Inset in (a)) is indexed according to β-$NaYF_4$ (JCPDS 16- 0334, space group P63/m). The red line in (b) represents a Gauss fit of the size distribution.

NaY-TS were aged for two days in PBS at pH = 7.4 and temperatures of 37 °C and 50 °C (Table 4.4). The dissolution results were compared to the NaY-R UCNPs with a cubic crystal structure.

Larger fractions of F^- were detected in PBS from NaY-R UCNPs than from NaY-TS UCNPs. This was also observed previously in water (Table 4.3) and can be attributed to the different crystal structures [155]. [158]. The dissolution degree increases with the aging temperature (37 versus 50 °C) for all samples, suggesting that the dissolution would be more significant at 37 °C after longer aging times (> 2 days). Namely, the higher aging temperature was applied as a simulation of longer-term aging at physiological conditions.

When comparing the fraction of dissolved F^- between NaY-TS UCNPs of different sizes, we can see that it increases with the decreasing particle size; for example: from around 10 mol.% of the fraction of dissolved F^- for the 36-nm-sized NaY-TS-A-aged to around 15 mol.% for 24-nm-sized NaY-TS-37. This is in agreement with the mentioned particle-size effect on the dissolution [12], [13], [14] – see Introduction, Section 1.1.3: Effect of the Surface on the Optical Properties of UCNPs.

Table 4.4: Particle size, aging temperature and the fraction of dissolved F^- of NaY-TS and NaY-R UCNPs. All samples were aged for two days in PBS at pH = 7.4.

UCNPs	Size (nm)	Aging temperature (°C)	Fraction of dissolved F^- (mol.%)
NaY-R-37	33 ± 5	37	27 ± 1
NaY-R-50	33 ± 5	50	48 ± 7
NaY-TS-A-aged	36 ± 1	37	9.90 ± 0.02
NaY-TS-XPS- aged	25 ± 1	37	13.8 ± 0.1
NaY-TS-37	24 ± 1	37	15.5 ± 1.4
NaY-TS-50	26 ± 2	50	23 ± 5
NaY-TS-B-aged	24 ± 1	50	27.3 ± 0.1

4.1.3.3 Effect of the Dissolution of β-$NaYF_4$ UCNPs on their Optical Properties

A significant dissolution of UCNPs in PBS (Table 4.4) encouraged us to study the effect of the dissolution of β-$NaYF_4$ UCNPs on their optical properties. Optical properties of unaged and aged NaY-TS UCNPs of specific sizes were compared and variations in the intensities of emission bands and changes in Yb^{3+} lifetimes were observed.

UC emission spectra of NaY-TS UCNPs, dispersed in miliQ water with concentration of $c \leq 1.4$ mg/ml, are shown in Figure 4.18. Emission intensities of all peaks were larger for the UCNPs with a larger size: 36-nm-sized NaY-TS-A versus 24-nm-sized NaY-TS-B. Due to this size effect [12], [13], [14] we only compare unaged and aged UCNPs of the same size in the subsequent text. Aged samples showed a significantly lower emission intensities in comparison to the unaged samples of the same size (Figure 4.18a). This can be, at least in part, explained by the formation of a nonluminescent solid side product (see results on the XPS analysis in the following and in the Discussion). Therefore, it should be more appropriate to compare normalized intensity that is normalized to the peak at 800 nm. Only a small difference in the normalized intensity of blue (475 nm) and red emission (650 nm) between the unaged and aged samples NaY-TS-A can be seen in Figure 4.18b and could be attributed to the fluctuations of the laser. Similarly, no significant difference in normalized emission intensity in red (at 650 nm) and blue emission (at 475 nm) was detected in the case of NaY-TS-B and NaY-TS-B-aged (Figure 4.18b). Therefore, we can conclude that no significant difference can be seen in the normalized emission intensities (Plohl *et.al*, submitted). Nevertheless, further investigations are required to completely understand the influence of dissolution on absolute emission intensity.

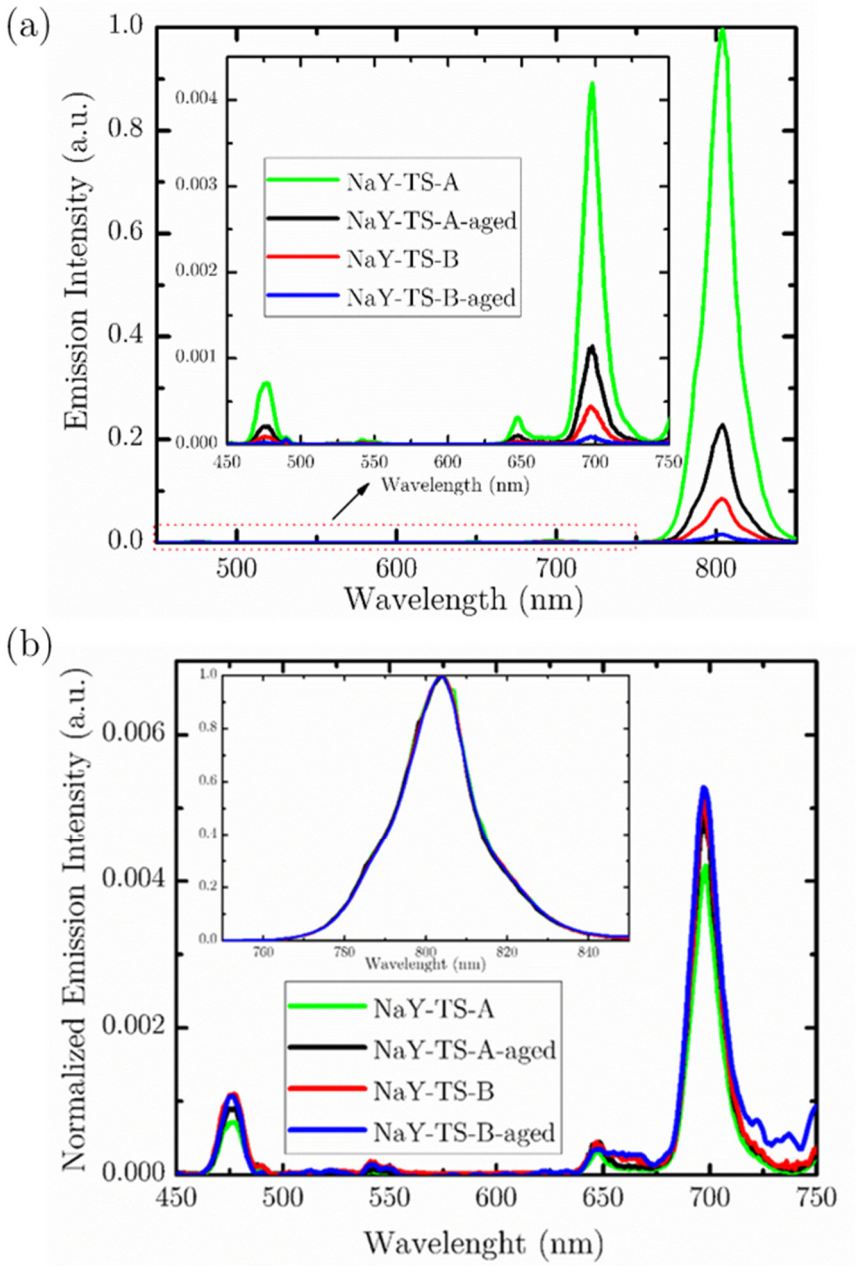


Figure 4.18: UC emission spectra (a) with normalized emission intensities (b) of unaged and aged NaY-TS samples A and B.

In the following, the emission decay kinetics of the Yb^{3+} sensitizer's emission at 980 nm upon excitation with 940 nm of NaY-TS samples was studied. Similar to the emission intensities, Yb^{3+} lifetimes also decreased with a decreasing size of the NaY-TS samples (Figure 4.19). Both size effects can be attributed to the effect of surface quenching arising from OH^- groups from the solvent [7], [13], [14]. Aged samples showed lower Yb^{3+} lifetimes than the unaged samples of the same size (Figure 4.19), which can be correlated to the partial deactivation of a $^2F_{5/2}$ state, which further results in lower lifetime for the $^2F_{5/2} \rightarrow {}^2F_{7/2}$ transition to the ground state [7]. The comparison between the two samples shows the larger decrease in the Yb^{3+} lifetime (around 17 %) for the NaY-TS-B sample with the larger fraction of the dissolved F^- (27.3 mol.%) than for the NaY-TS-A (around 15 %) with

the lower fraction of the dissolved F^- (9.9 mol.%). This suggests that the dissolution of UCNPs in PBS must significantly affect their surface chemistry (Plohl *et al.*, submitted).

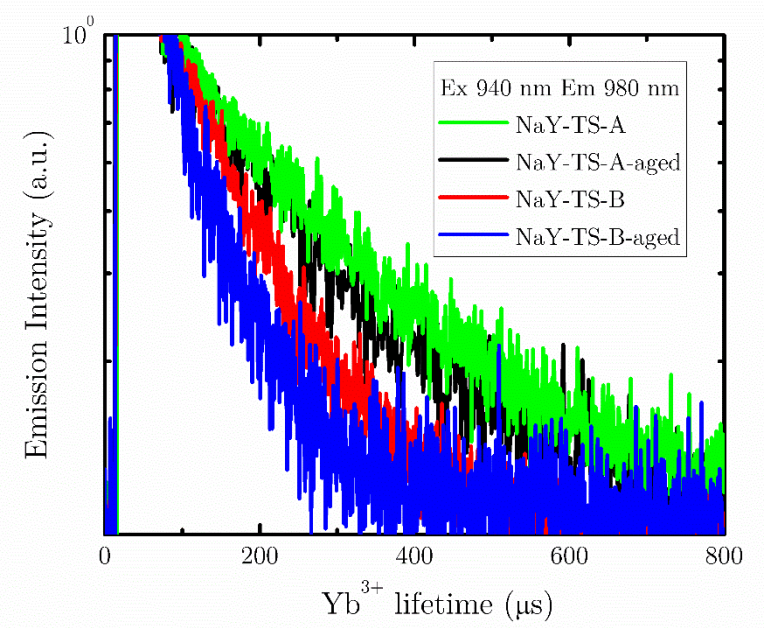


Figure 4.19: Emission intensity of Yb^{3+} lifetimes for unaged and aged NaY-TS samples.

To understand the effect of the dissolution on the surface composition and further on their optical properties, a surface analysis with XPS was performed on the unaged and aged 25 nm-sized NaY-TS-XPS UCNPs. Typical survey spectra, comparison of the samples surface composition and normalized surface composition are shown in Figure 4.20. All the constituent elements (including O) were detected at surfaces with exception of Tm, (below the detection limit). The normalized surface composition (to Y=1) for the NaY-TS-XPS-unaged was $Na_{0.53}Y_1Yb_{0.24}F_{3.55}O_{0.33}$ and for the NaY-TS-XPS-aged was $Na_{0.4}Y_1Yb_{0.25}F_{1.3}O_{3.6}P_{0.8}$. The fraction of detected O is significantly higher in the aged sample than in the unaged sample, while the fraction of F is lower in the aged sample. This is consistent with the observed dissolution of F^- (Table 4.4). The deficiency of F^- ions can be compensated with other species, i.e. O^{2-} or OH^- ([158], [159] - see Discussion).

Moreover, both the unaged and the aged sample revealed the Na:Y ratio < 1, suggesting a substoichiometric fraction of Na at the UCNP surface, while the ratio between Y:Yb in normalized surface composition is close to stoichiometric and it does not change with aging.

Beside the peaks of constituent elements, the C peak is also observed in both samples. The concentration of C was typical as in any sample and resulted from the specific nature of the method.

In addition to this, P was detected in the aged sample. The latter can be attributed to the phosphates from the PBS that form insoluble compounds with the dissolved Ln^{3+} from UCNPs [159]. This is also in accordance with the significantly larger fraction of O in the aged sample. Based on the XPS results (Figure 4.20), lower emission intensities of aged NaY-TS UCNPs (Figure 4.18a) can be attributed to the larger deviation of the surface composition from the nominal composition and to the "dilution" of the UCNPs with the solid side product of Ln-phosphate (see Discussion).

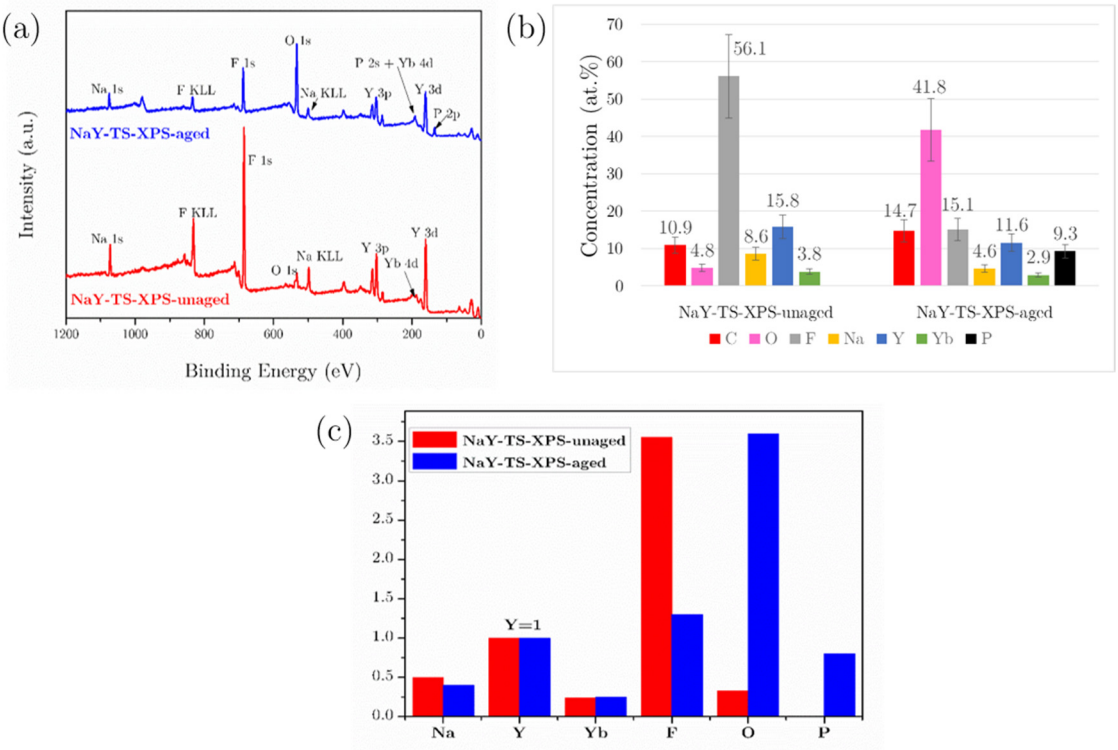


Figure 4.20: XPS survey spectra of the unaged and aged NaY-TS-XPS UCNPs (a) with respective atomic fractions (b). The relative error in concentration in (b) was estimated to be about 20 %. The normalized surface compositions with respect to Y are compared in (c).

4.2 Effects of Amphiphilic Coatings on the Dissolution of Fluoride UCNPs in Aqueous Systems

Due to the significant dissolution of UCNPs it is necessary to protect the UCNPs' surfaces against aqueous media. One of the simplest solutions would be the application of a silica coating. However, porous silica cannot prevent the diffusion of small molecules and cations to and from the UCNPs' surfaces (see Chapter 4.1.3.1). Therefore, we decided to test polymer coatings. Due to their superior optical properties hexagonal β-$NaYF_4$ UCNPs were used in this study. Surfaces of the as-synthesized oleate-capped β-$NaYF_4$ UCNPs are hydrophobic and, they have to be properly functionalized in order to be dispersable in water. An elegant solution would be the coating of UCNPs with amphiphilic copolymers. First, there is no need for the exchange of the hydrophobic oleate with hydrophilic ligands. Second, the hydrophilic part of the amphiphilic polymer with specific functional groups ensures the colloidal stability of UCNPs in water. At the same time, we assumed that the hydrophobic layer at the very surface of UCNPs would prevent the interaction with water media. During this study two different amphiphilic coatings were tested: PMAO-BHMT and TPGS.

4.2.1 Formation of the PMAO-BHMT Coating

In this study we used as-synthesized oleate-capped UCNPs, NaY-TS@OA, with sizes of around 22–24 nm. The NaY-TS@OA UCNPs were first coated with PMAO, which was subsequently cross-linked with BHMT (Figure 3.2, Figure 4.21) to yield NaY-TS@PMAO-BHMT UCNPs.

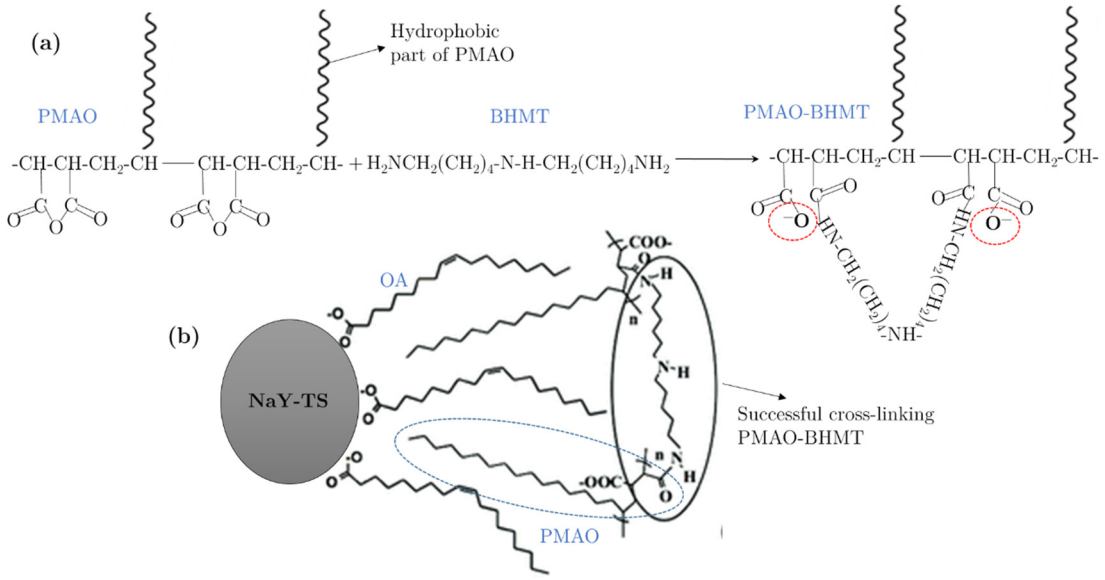


Figure 4.21: Schematic representation of cross-linking of PMAO with BHMT (a,b). (b) was modified from [19].

The cross-linking of NaY-TS@OA UCNPs with PMAO-BHMT polymers was confirmed with ATR-FTIR spectroscopy (Figure 4.22). The bands at 1857 and 1780 cm^{-1} correspond to stretching vibrations of anhydride rings present in the pure PMAO. These two bands are absent in the NaY-TS@PMAO-BHMT UCNPs indicating that the anhydride rings opened and reacted with BHMT (Figure 4.21). Moreover, the band at 1712 cm^{-1} in NaY-

TS@PMAO-BHMT corresponds to stretching of COOH groups from opened anhydride rings of the PMAO (Figure 4.21). The bands at 1560 and 1407 cm^{-1}, from the NaY-TS@PMAO-BHMT, are attributed to the vibrations of R-COO^- groups. The bands at 2924, 2848 and 1467 cm^{-1} correspond to $-CH_2$ group present in both polymers and at the surface of NaY-TS@PMAO-BHMT. The bands from cross-linker BHMT at 3359, 3280 and 1598 cm^{-1} are attributed to the N-H bonds from $-NH_2$ groups. However, these groups are absent in the NaY-TS@PMAO-BHMT UCNPs, again indicating the successful cross-linking of the amphiphilic polymer PMAO with cross-linker BHMT [19].

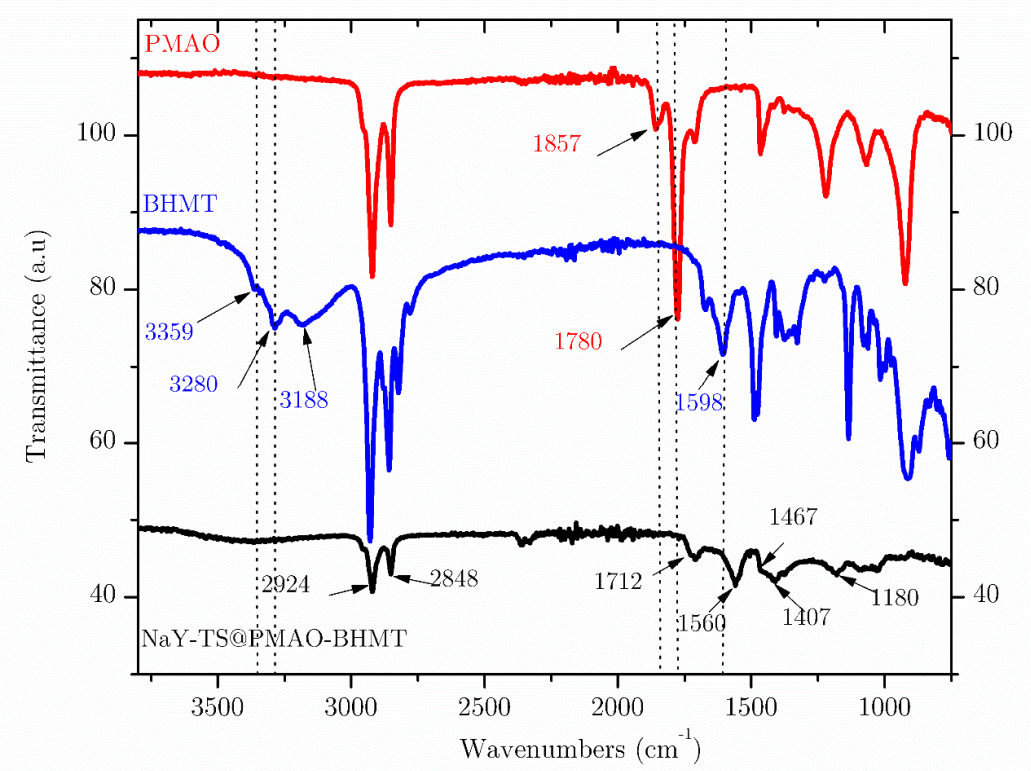


Figure 4.22: ATR-FTIR spectra of PMAO, BHMT and NaY-TS@PMAO-BHMT UCNPs.

The above results suggest, but do not directly confirm, the formation of the PMAO-BHMT coating on the surfaces of NaY-TS@OA. To verify this, we measured zeta potential versus pH for bare (without OA) NaY-TS UCNPs and NaY-TS@PMAO-BHMT UCNPs, both dispersed in water (Figure 4.23). NaY-TS@PMAO-BHMT UCNPs formed an optically transparent suspension in water with no sedimentation over the weeks, while bare NaY-TS UCNPs agglomerated and sedimented in water immediately. Zeta potential of bare NaY-TS UCNPs is positive at low pH values, due to the presence of OH^{2+} groups on their surfaces, and negative at higher pH values, where negative potential results from OH^- groups on their surfaces. The IEP is around pH = 8. However, zeta potential of NaY-TS@PMAO-BHMT UCNPs is negative in the whole measured pH range with relatively high absolute values, indicating that the surfaces of the NaY-TS were successfully coated with PMAO-BHMT. The negative zeta potential arises from the hydrolyzed carboxylic groups, formed by the ring opening of the maleic anhydrides (Figure 4.21) [19]. The IEP is at pH = 2 and it was also confirmed with the flocculation of the suspensions at this pH.

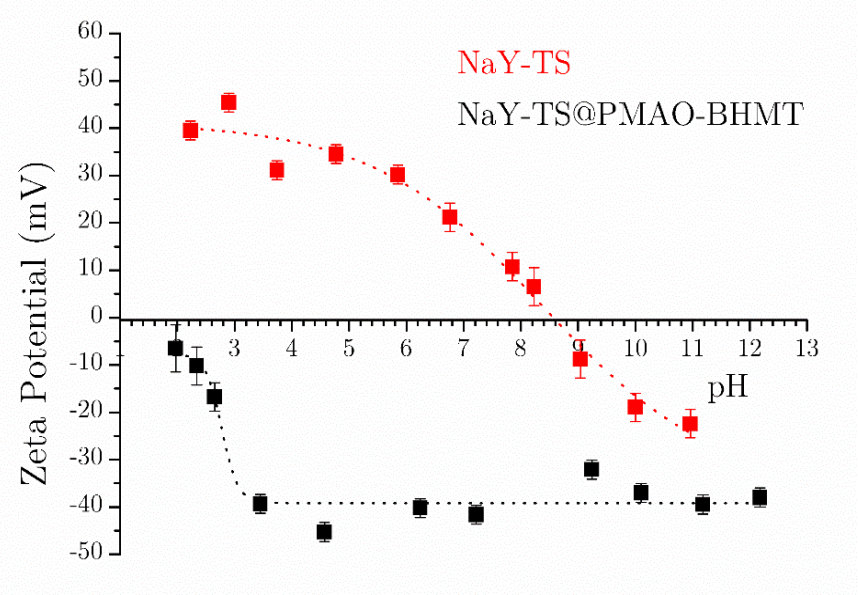


Figure 4.23: Zeta potential versus pH of NaY-TS and NaY-TS@PMAO-BHMT UCNPs in water.

DLS measurements were performed on stable suspensions of NaY-TS@PMAO-BHMT UCNPs in water. The hydrodynamic diameter is significantly larger ~40–50 nm. (Figure 4.24a) than the size of as-synthesized NaY-TS UCNPs (24 nm), determined with the TEM analysis (Figure 4.24b). This can be correlated to the formation of the PMAO-BHMT coating on the surfaces of the NaY-TS UCNPs. Note that it was not possible to measure the hydrodynamic diameter of bare NaY-TS UCNPs, for a comparison, since they agglomerated in water.

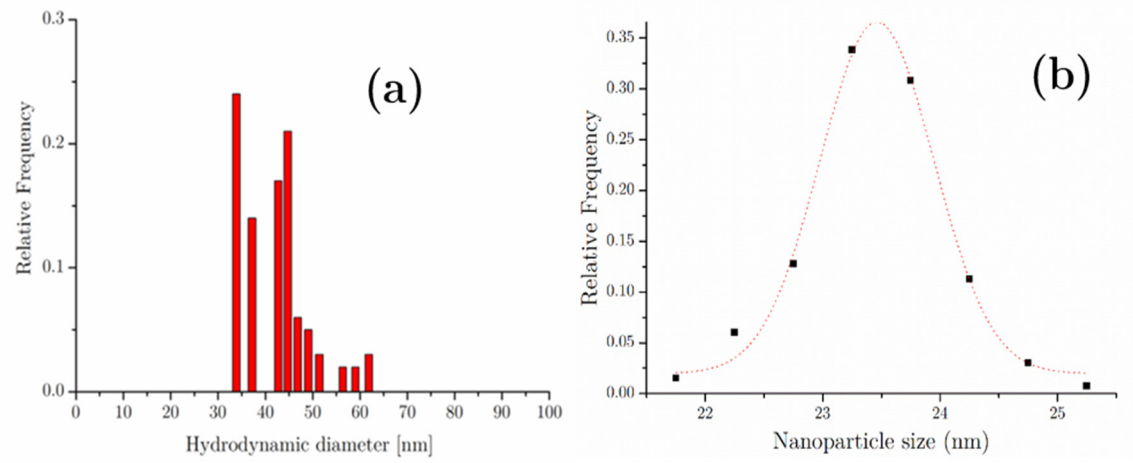


Figure 4.24: Number-weighted distribution of the hydrodynamic diameter of NaY-TS@PMAO-BHMT UCNPs in water (a) and the size of NaY-TS UCNPs (b).

TGA of bare (NaY-TS-1) and coated (NaY-TS-1@PMAO-BHMT) UCNPs was performed (Figure 4.25) in order to determine the fraction of organic coating. The bare NaY-TS-1 UCNPs do not show any significant mass loss, indicating that the OA was successfully removed from their surfaces. However, NaY-TS-1@PMAO-BHMT UCNPs

display a significant mass loss. First, a minor mass loss above 100 °C can be most probably related to the desorption of water, also seen as endothermic peak in the DTA curve. Additionally, a significant mass loss in the NaY-TS-1@PMAO-BHMT UCNPs is seen in the range between 150 and 450 °C, with the largest mass-loss rate at T ~ 280 °C, which was accompanied with an exothermic peak in the DTA curve. This mass loss of 55 % can be attributed to the decomposition of PMAO-BHMT. The fact that the mass loss stopped above 450 °C indicates that the decomposition of the organic phase was quantitative.

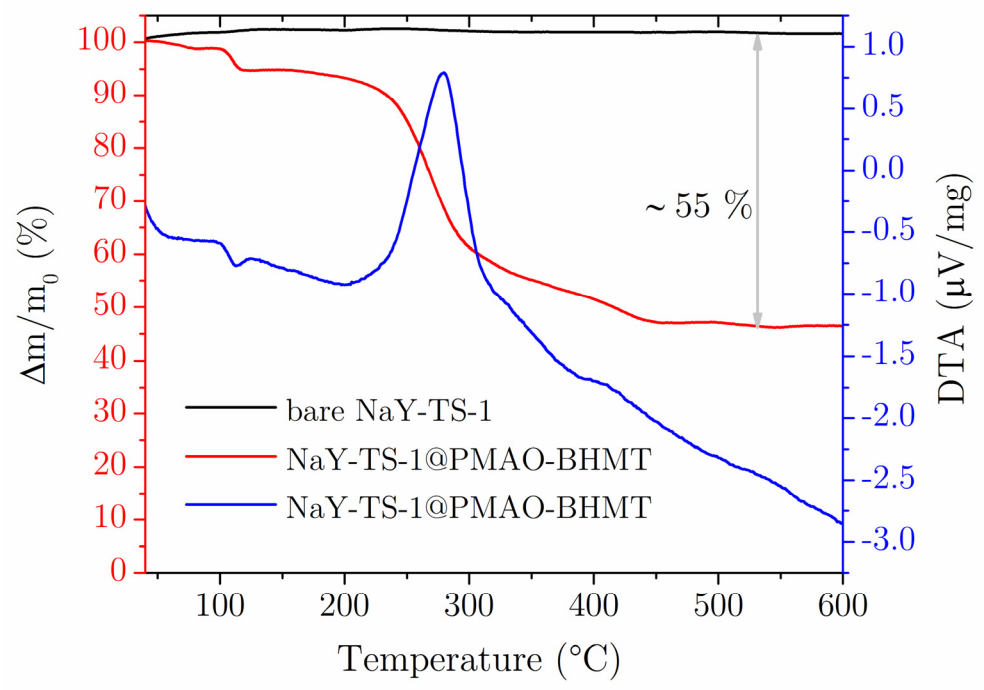


Figure 4.25: TGA (red line) and DTA (blue line) curves of the PMAO-BHMT-coated NaY-TS-1 UCNPs. For the comparison the TGA curve (black line) of bare NaY-TS-1 UCNPs in also included.

UC emission spectra of the bare NaY-TS-1 and coated NaY-TS-1@PMAO-BHMT UCNPs are presented in Figure 4.26. NaY-TS-1@PMAO-BHMT UCNPs show significantly higher emission intensity than the bare NaY-TS-1 UCNPs, although they were both dispersed in water. This is attributed to the quenching of the emission of Tm^{3+} with OH^- groups from water, which interact with the bare NaY-TS UCNPs' surfaces [7], [15], [24]. In contrast to this, the PMAO-BHMT coating protects the surfaces of NaY-TS UCNPs against these interactions.

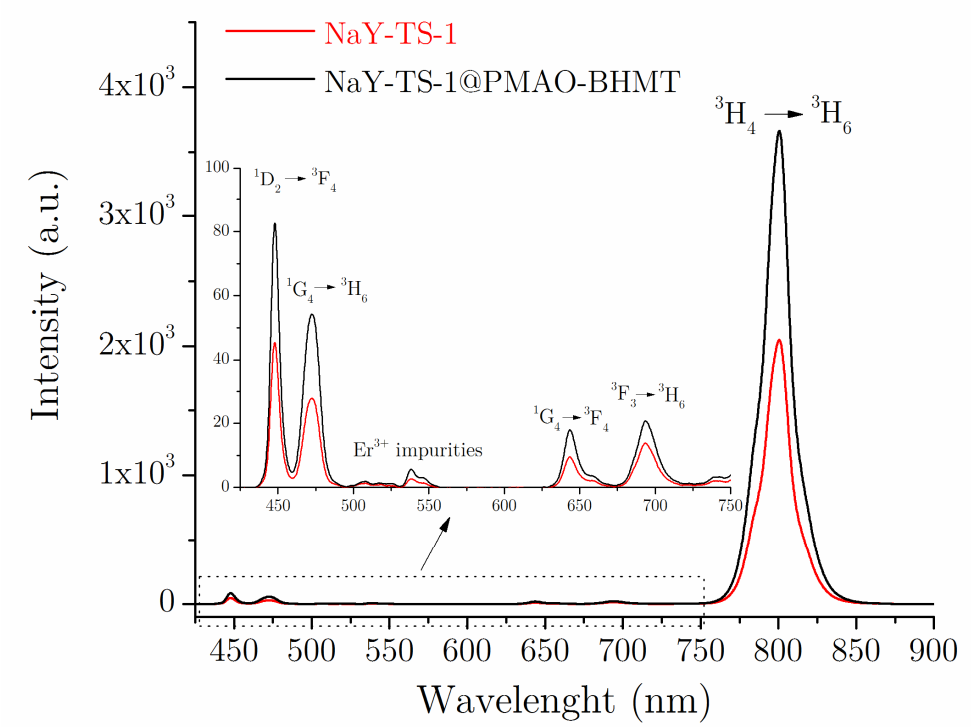


Figure 4.26: Comparison of emission intensities of bare NaY-TS-1 and coated NaY-TS-1@PMAO-BHMT UCNPs in aqueous suspension. Emission intensities were normalized to the UCNPs' concentration (c = 1 mg/ml).

4.2.2 Formation of the TPGS Coating

TPGS consists of a hydrophobic part based on vitamin E ($C_{29}H_{50}O_2$) and a hydrophilic part, which is PEG. Both of the constituent components (i.e., vitamin E and PEG), as well as TPGS are known to be biocompatible [20], [77]–[80], [160]. We were interested in the efficiency of the TPGS coating as a protection against the dissolution of UCNPs. For this purpose, we coated as-synthesized 28 nm-sized β-$NaYF_4$ UCNPs (NaY-TS@OA) with TPGS (NaY-TS-2@TPGS).

The formation of amphiphilic polymer TPGS was examined with ATR-FTIR spectroscopy (Figure 4.27). The presence of the OA ligands on the surfaces of as-synthesized NaY-TS@OA were confirmed with the band at 2924 cm^{-1}, which is attributed to antisymmetric stretching of $–CH_2$ in OA, while the band at 2854 cm^{-1} corresponds to symmetric stretching of $–CH_2$. The band at 1710 cm^{-1} is attributed to stretching vibrations of C=O and the band at 1461 cm^{-1} is attributed to $–CH_2$ bending [161]. The band at 1734 cm^{-1}, observed in NaY-TS@TPGS, corresponds to the stretching vibrations of – COOH, band at 1143 cm^{-1} corresponds to the anti-symmetric vibration of –C-O-C– and stretching band at 1101 cm^{-1} corresponds to the vibration of –C-C– bonds [20], [80]. Other bands, at 1045–1500 cm^{-1}, correspond to C-O stretching vibrations [162]. The stretching vibrations at 2925–2854 cm^{-1} were significantly enhanced after the coating with TPGS, indicating the increased number of $–CH_2$ groups on the UCNPs' surfaces. Moreover, the presence of C-O vibrations at 1045–1500 cm^{-1} bands also suggests the formation of TPGS on the surfaces of NaY-TS@OA.

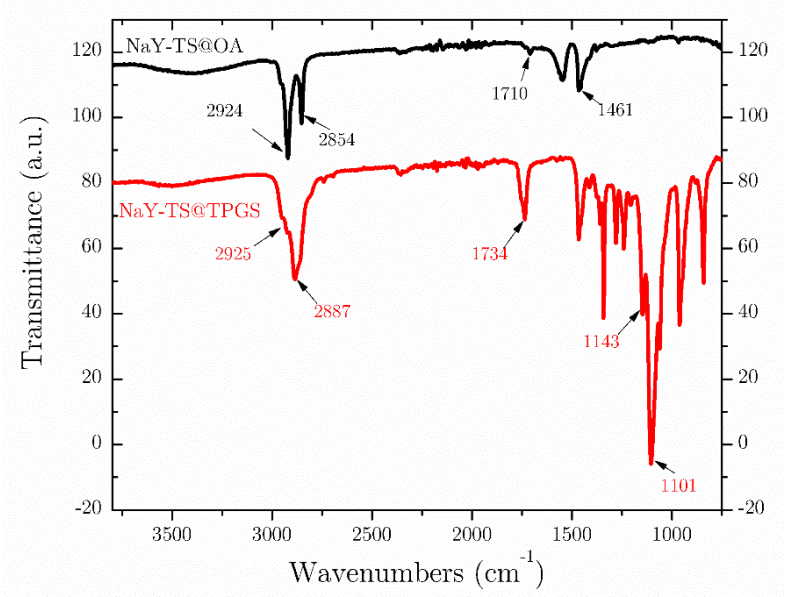


Figure 4.27: ATR-FTIR curves before and after the coating of UCNPs with TPGS.

To confirm the formation of the TPGS coating on the NaY-TS UCNPs zeta potential of the bare NaY-TS UCNPs and NaY-TS@TPGS UCNPs in water were measured (Figure 4.28). A significant difference in zeta potential values of between the two samples is observed. The zeta-potential behavior of the bare NaY-TS UCNPs was similar as previously (Figure 4.23) with IEP at pH ~ 8. On the contrary, NaY-TS@TPGS UCNPs showed relatively low absolute values of the zeta-potential, which is common for NPs, coated with PEG [163], [164], the hydrophilic component of TPGS. TPGS is a non-ionic surfactant and PEG provides steric stabilization of NPs by extending its long chains into aqueous media [163]. The change of the IEP from pH ~ 8 for NaY-TS UCNPs to pH ~ 4 for NaY-TS@TPGS, additionally confirms the formation of the TPGS on the UCNPs' surfaces.

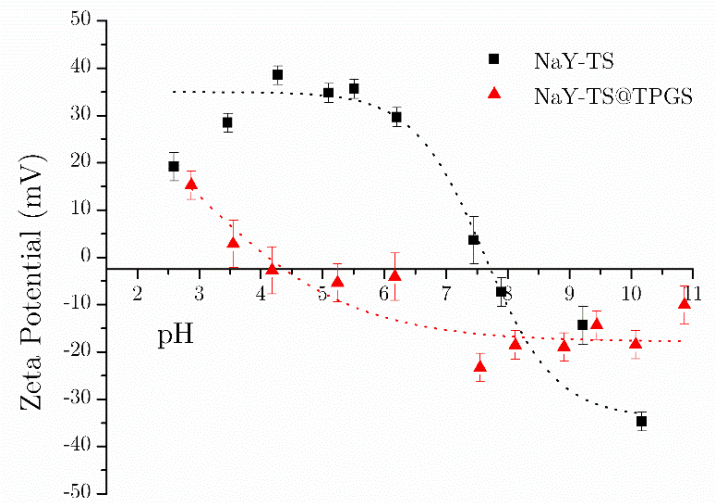


Figure 4.28: Zeta potential versus pH of NaY-TS UCNPs and NaY-TS@TPGS UCNPs in water.

The decomposition of the TPGS coatings was followed with TGA (Figure 4.29). TPGS started to decompose at approximately 180 °C. The mass loss below 300 °C can be attributed to intramolecular dehydration, associated with the hydroxyl groups of the PEG [165]. The dehydration consequently resulted in the decomposition of the alkene chain(s), which were thermally unstable and promoted a continuous degradation of TPGS [165]. Three exothermic DTA peaks at three different stages (~200, 285, 380 °C) confirm the decomposition of TPGS. TPGS decomposes completely at T ~ 450 °C.

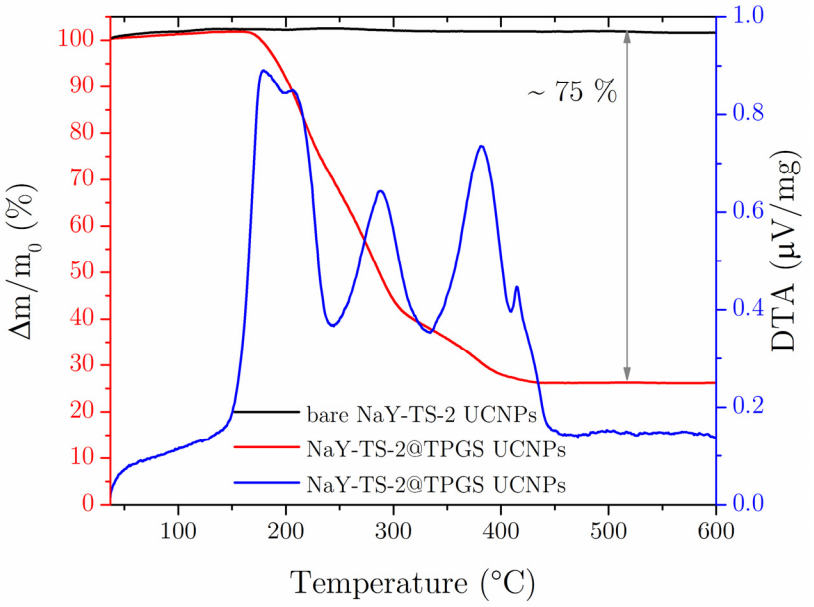


Figure 4.29: TGA (red line) and DTA (blue line) curves of the TPGS-coated NaY-TS-2 UCNPs. For the comparison the TGA curve (black line) of bare UCNPs is also included.

A very large fraction of the TPGS polymer (i.e., ~75 %) was determined on the NaY-TS UCNPs and was consistent with the previous study (~84 %) [80]. A part of it can be attributed to the excess of the unbound polymer. However, OA, originating from the as-synthesized NaY-TS@OA, also contributes 30 % of the weight loss.

Nevertheless, the NaY-TS@TPGS UCNPs were stable in water for several weeks and were also dispersible in PBS. However, after a while, when the suspension in PBS was exposed to 37 °C, some floccules were observed with a naked eye. After 2 days of aging at 37 °C in the PBS suspension an enormous amount of a flocculated product was observed. This can be ascribed to the sterically stabilized NPs, which are more sensitive to temperature than electrostatically stabilized NPs. The latter are more sensitive to the changes of ionic strength and pH of the media [106].

Emission spectra of the bare NaY-TS-2 and NaY-TS-2@TPGS UCNPs, both dispersed in water, show a significant difference in emission intensities between the two samples (Figure 4.30). A significantly higher emission intensity of the coated NaY-TS-2@TPGS UCNPs originates from the TPGS, which protects the Yb^{3+} and Tm^{3+} surface ions from OH^- vibrations arising from the solvent [7], [15], [24], similar as in the case of PMAO-BHMT coating (Figure 4.26).

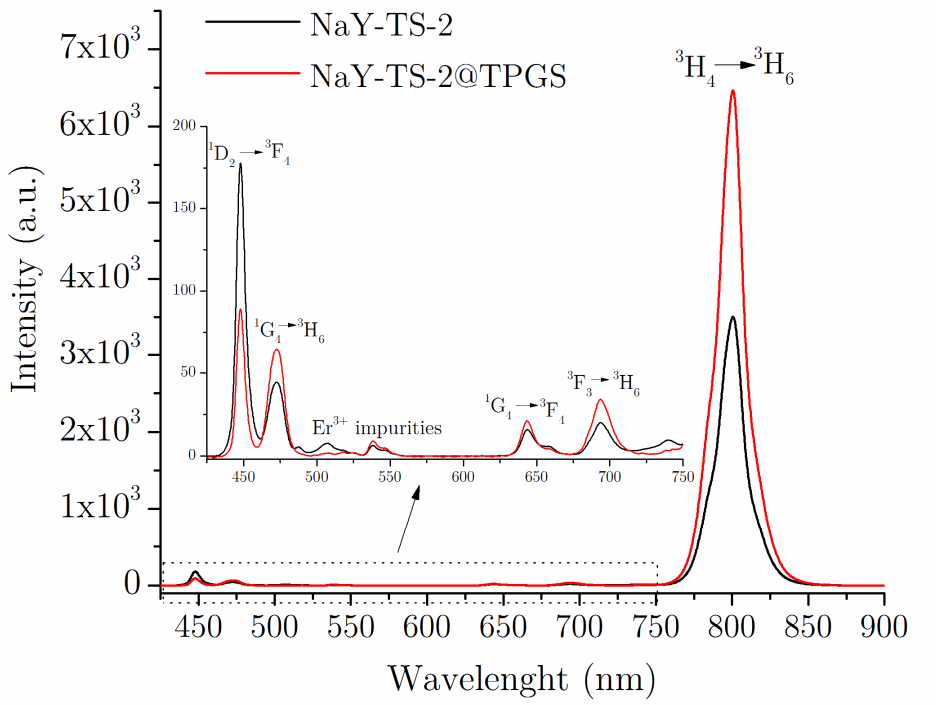


Figure 4.30: UC emission spectra of the bare NaY-TS-2 UCNPs and coated NaY-TS-2@TPGS (28 nm). Emission intensities were normalized to UCNPs' concentration (c = 1 mg/ml).

4.2.3 Dissolution Study

To evaluate the efficiency of the studied amphiphilic coatings against the dissolution of UCNPs in aqueous systems the dissolution degree of bare NaY-TS UCNPs and those coated with amphiphilic coatings was compared. The samples were aged for two days in PBS at 37 °C and pH = 7.4 (Table 4.5). In order to avoid the size effect on the dissolution (Table 4.4), bare and coated UCNPs of the same sizes were compared.

It is obvious that the PMAO-BHMT coating significantly decreases the dissolution of NaY-TS UCNPs. However, it does not prevent it completely. The fraction of dissolved F^- from NaY-TS-1@PMAO-BHMT UCNPs is 8-times lower than that from the bare NaY-TS-1 UCNPs. This makes the PMAO-BHMT coating much more efficient than the silica coating (Figure 4.16).

In contrast to the above, the TPGS coating seems to promote the dissolution of the studied UCNPs. The fraction of the dissolved F^- implies that almost all NaY-TS@TGPS UCNPs were dissolved during the aging. This was confirmed with the TEM analysis, with which only a few remaining UCNPs were observed (Figure 4.31c). Detailed TEM analysis of the residuals after aging (Figure 4.31a) revealed that only amorphous structures were present in the PBS after aging, consisting of Y, Yb, P and O (Figure 4.31b). The phosphate-rich material most likely precipitates from the dissolved Ln^{3+} and the phosphates from the PBS [138], [159], [166].

Table 4.5: Fraction of the dissolved F^- from the bare and coated NaY-TS UCNPs after the aging for two days in PBS at pH = 7.4 and T = 37 °C.

UCNPs	Size of UCNPs (nm)	Fraction of dissolved F^- (mol.%)
bare NaY-TS-1	22 ± 1	19.0 ± 0.5
NaY-TS-1@PMAO-BHMT	22 ± 1	2.4 ± 0.6
bare NaY-TS-2	26 ± 1	18.2 ± 0.4
NaY-TS-2@TPGS	26 ± 1	83.4 ± 6.9

Additionally, a significant decrease of the UC emission intensity was measured in water suspensions of aged NaY-TS@TGPS UCNPs (Figure 4.31d). We observed a 37-times lower emission intensity at 800 nm. However, when TPGS-coated UCNPs were dispersed in water, the UC emission intensity did not change over time [20], suggesting their chemical stability in water.

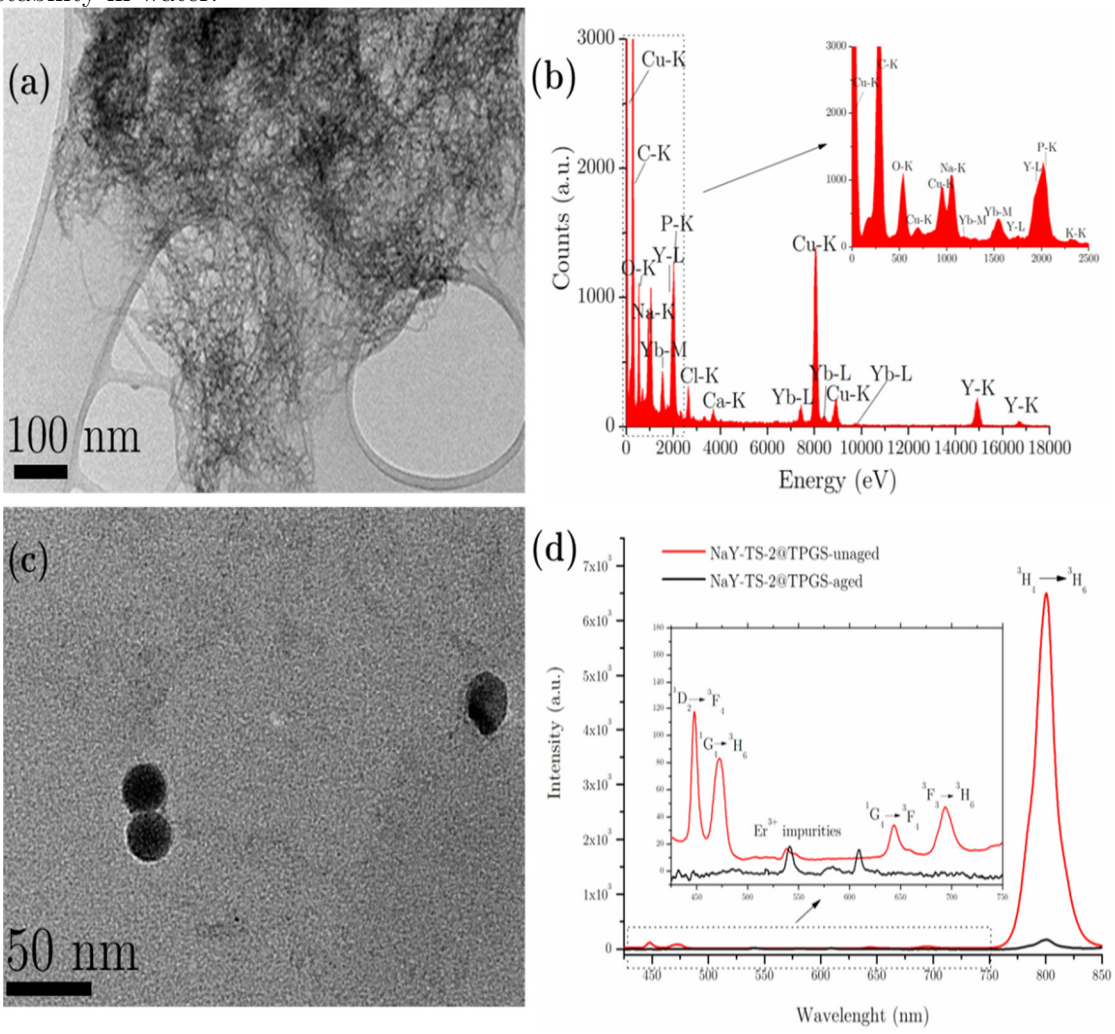


Figure 4.31: Amorphous side product after the aging of NaY-TS@TPGS UCNPs in PBS (a), with the corresponding EDXS spectrum (b), and few remaining UCNPs after the aging (c). The UC emission spectra of the unaged and aged TPGS-coated UCNPs are shown in (d).

Chapter 5

Discussion

5.1 Dissolution of Fluoride UCNPs in Aqueous Media

In the ever growing field of nanomaterials for biomedical applications numerous studies about fluoride UCNPs were published [3], [4], [28], [54]. However, to the best of our knowledge, the dissolution studies of fluoride UCNPs have rarely been reported [106]. In my thesis, I studied the dissolution of fluoride UCNPs. Preliminary results indicated chemical instability of binary fluoride UCNPs [158]. However they suffer from poor emission efficiency and in the continuation a special attention was paid to the dissolution of the $NaYF_4$ UCNPs, co-doped with Yb^{3+}/Tm^{3+} in two polymorphic forms (i.e., cubic (α) and hexagonal (β)).

First we evaluate the effect of different factors on the dissolution of the $NaYF_4$ UCNPs (Table 5.1).

The *effect of crystal structure* was evaluated by a comparison of the dissolution of the α- $NaYF_4$ UCNPs with a cubic structure and β-$NaYF_4$ UCNPs with a hexagonal crystal structure (i.e., NaY-HS versus NaY-TS UCNPs and NaY-R-37,50 versus NaY-TS-37,50 UCNPs, Table 5.1) in different aqueous media (i.e., weakly acidic water solution and PBS). The lower degree of the dissolution of β-$NaYF_4$ UCNPs was suggested from the lower degree of the dissolution of F^- and other constituent ions (Table 4.3).

The usage of different synthesis methods for the synthesis of the $NaYF_4$ UCNPs with the two different structures might also affect their surface chemistry, which can further affect their dissolution behavior. Therefore, we analyzed the surface compositions of the respective UCNPs. The unaged α-$NaYF_4$ UCNPs (NaY-R) and β-$NaYF_4$ UCNPs (NaY-TS-XPS) UCNPs' surface compositions were similar (Figure 4.14 and Figure 4.20b), while a larger fraction of O was detected on the surfaces of the hydrothermally synthesized α- $NaYF_4$ UCNPs (NaY-HS-1, Figure 4.8). The latter can be attributed to the water used for the synthesis of NaY-HS-1, while the other samples (NaY-R and NaY-TS) were synthesized in aqueous-free media. Regardless of this, a significantly lower dissolution degree was observed for the β-$NaYF_4$ UCNPs aged at the same conditions than for the α- $NaYF_4$ UCNPs (Table 5.1). Therefore the differences in the dissolution between α- and β-$NaYF_4$ UCNPs can be (primarily) attributed to the different crystal structures and their thermodynamic stabilities [155], [158], [167].

Table 5.1: Summary of UCNPs and their dissolution study. Note that binary fluoride UCNPs were excluded from the discussion.

UCNPs	Synthesis and synthesis medium	UCNPs' size (nm)	Aqueous media for aging	pH of aging	T (°C)	Aging time	Fraction of dissolved F^- (mol.%)
NaY-HS-20	HS, Water	1135±25	water	Weakly acidic	RT	3 days	1.10 ± 0.01
NaY-HS-10		160±13					0.85 ± 0.01
NaY-HS-1		103±10					0.94 ± 0.02
NaY-R	R, EG	33±5	PBS	7.4	RT	(15–120) min	(3.0±0.3)–(4.8±0.4)
						1 day	6.9 ± 0.6
						2 days	11.0 ± 2.2
NaY-R-37					37	2 days	27 ± 1
NaY-R-50					50	2 days	48 ± 7
NaY-R@PVP	R, EG	38±8	PBS	7.4	RT	(15–120) min	(3.4±0.3)–(4.7±0.2)
						1 day	8.9 ± 2.4
						2 days	12.6 ± 2.4
NaY-R@SiO2	R, EG	38±8	PBS	7.4	RT	(15–120) min	(1.3±0.3)–(1.5±0.3)
						1 day	3.2 ± 1.1
						2 days	5.4 ± 2.6
NaY-TS	TS, OA+ODE	21 ± 3	water	Weakly acidic	RT	3 days	0.39±0.11
NaY-TS-37		24 ± 1	PBS	7.4	37	2 days	15.5 ± 1.4
NaY-TS-XPS		25 ± 1			37		13.8 ± 0.1
NaY-TS-A-aged		36 ± 1			37		9.90 ± 0.02
NaY-TS-B-aged		24 ± 1			50		27.3 ± 0.1
NaY-TS-50		26 ± 2			50		23 ± 5
NaY-TS-1		22 ± 1			37		19.0 ± 0.5
NaY-TS-1@PMAO-BHMT		22 ± 1			37		2.4 ± 0.6
NaY-TS-2		26 ± 1			37		18.2 ± 0.4
NaY-TS-2@TPGS		26 ± 1			37		83.4 ± 6.9

The influence of the size on the dissolution of β-$NaYF_4$ UCNPs (NaY-TS) was studied (Table 4.4 and Table 5.1). The fraction of dissolved F^- in PBS is increasing exponentially with the decreasing size of UCNPs (Figure 5.1). This is consistent with the Ostwald-Freundlich equation (Equation (1.5)) [111] and with other studies. For example, the dissolution degree of Ag and ZnO NPs in acidic media increased with the decreasing of their sizes [168],[169].

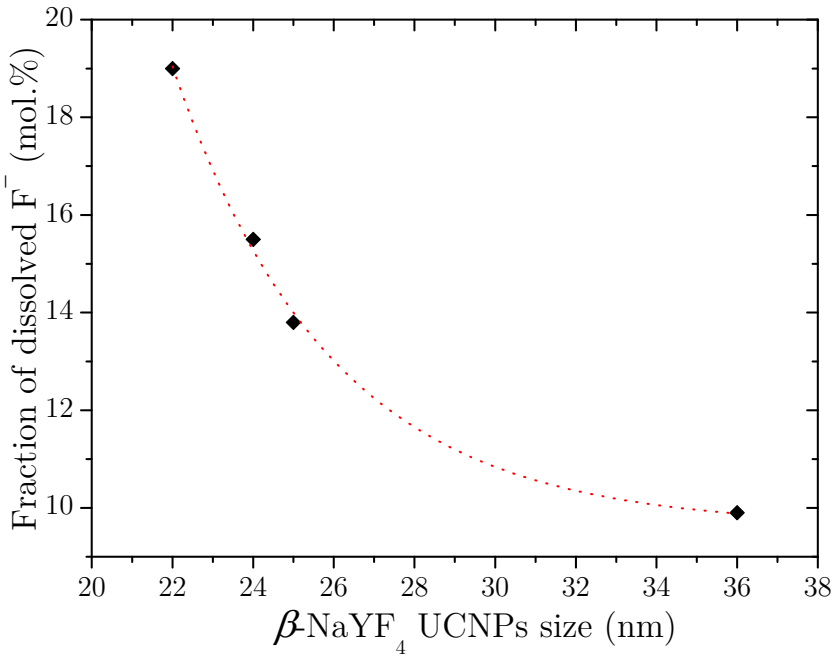


Figure 5.1: Fraction of dissolved F^- versus β-$NaYF_4$ (NaY-TS) UCNPs' size, aged in PBS at pH = 7.4 for 2 days at 37 °C. The dotted line represents an exponential fit.

The effect of agglomeration was not possible to study because bare UCNP were not colloidally stable in aqueous suspensions. At the same time the degree of agglomeration was not controllable in the studied systems. In general, the formation of agglomerates can slow down the dissolution by reducing the surface of NPs exposed directly to the solvent [104]. Considering this, dissolution of F^- could be even higher, if the UCNPs were not agglomerated. Nevertheless, for this purpose we did a comparison test of the dissolution of α-$NaYF_4$ UCNPs (NaY-R UCNPs), which were stirred or not (both samples from the same synthesis batch) during the whole aging process (in PBS at the pH = 7.4 at 37 °C for 2 days). No significant difference in the fraction of dissolved F^- between the unstirred (27 mol.% of F^-) and stirred (26 mol.% F^-) sample was observed.

The dissolution is also *dependent on the aging temperature*. The influence of temperature was studied on the α-$NaYF_4$ (NaY-R) and β-$NaYF_4$ (NaY-TS) UCNPs, aged for 2 days in PBS, at pH = 7.4 at different temperatures (Table 5.1). It is clear that the dissolution degree increased significantly with the increasing temperature. This is in agreement with the Arrhenius equation [170] (Figure 5.2).

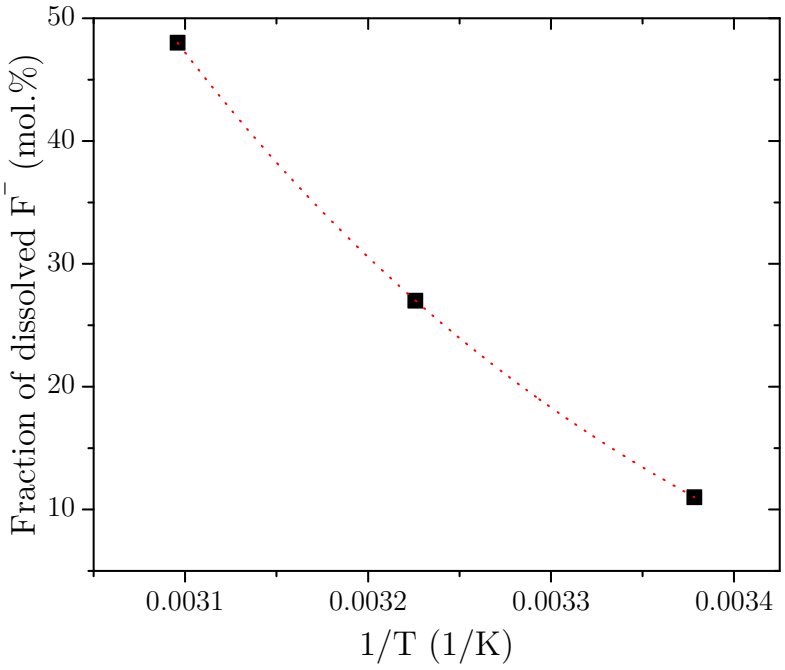


Figure 5.2: Fraction of dissolved F^- of α-$NaYF_4$ (NaY-R) UCNPs, aged in PBS for 2 days at pH = 7.4, versus aging temperature. The dotted red line represents an exponential fit.

We also investigated *the influence of the media composition* on the dissolution of $NaYF_4$ UCNPs. When UCNPs are used *in vivo* and *vitro* experiments [142], [171], they are often dispersed in PBS with a defined physiological pH (i.e., 7.4). For this reason, the dissolution of α-$NaYF_4$ (i.e., NaY-R-37,50) and β-$NaYF_4$ (i.e., NaY-TS-37,50) UCNPs in PBS was studied. Both types of UCNPs dissolved much more significantly in PBS than in water (Table 5.1).

The dissolution of the UCNPs in aqueous media most likely begins with the hydrolysis of the UCNPs' surfaces [158], [159] and can be processed until all the surfaces F^- are substituted with OH^-:

$$\alpha,\beta - NaLnF_4(s) \overset{H_2O}{\Longleftrightarrow} NaLnF_{4-x}(OH)_x(s) \; + \; x\; F^-(aq) \; + \; x\; H_3O^+(aq) \tag{5.1}$$

In a typical dissolution process, the UCNPs would dissolve stoichiometrically, as below:

$$\alpha,\beta - NaLnF_4(s) \overset{H_2O}{\Longleftrightarrow} xNa^+(aq) + \; xLn^{3+}(aq) + 4xF^-(aq) + (1-x)NaLnF_4(s) \tag{5.2}$$

However, our dissolution experiments in water showed substoichiometric fractions of the dissolved Ln^{3+} versus F^- (Table 4.3). This was true for both types of UCNPs aged in water, α-$NaYF_4$ (NaY-HS-1) and β-$NaYF_4$ (NaY-TS), regardless of their different surface compositions (Figure 4.8). Namely, the surface composition of NaY-HS-1 deviated much more significantly from the nominal composition than that of NaY-TS (Figure 4.8). All these support the above assumption on the hydrolysis of the UCNPs in water (Equation (5.1)).

A much more significant degree of the dissolution of the UCNPs was observed in PBS than in water (Table 5.1). This was attributed to the high affinity of Ln^{3+} ions for the

complexation with phosphates [172]. The formation of stable Ln-phosphates compounds was proposed as a driving force for the dissolution of UCNPs [159]:

$$\begin{aligned}\alpha,\beta - NaLnF_4(s) + \ xHPO_4^{2-}(aq) \overset{PBS}{\Longleftrightarrow} xNa^+(aq) \\ + \ 4xF^-(aq) + xLnPO_4 \times nH_2O\ (s) + xH_3O^+(aq) + (1-x)NaLnF_4(s)\end{aligned} \tag{5.3}$$

Since the phosphate ions can be differently hydrated [173], a general formula for Ln-phosphate compounds was used.

The proposed mechanism is in accordance with the decreasing of the pH during the aging of the suspensions in PBS, as a consequence of the released H_3O^+ (Equation (5.3)). For instance, the PBS with dispersed fluoride NaY-TS-37 UCNPs had pH = 7.4 at the beginning and it decreased during the aging at 37 °C for 2 days to pH = 7.17. Higher decrease in the pH was observed in the samples with a higher fraction of the dissolved F^-. Furthermore, amorphous side product formed during the aging in PBS (Figure 5.3a). EDXS confirmed that these residuals were composed of Y, Yb, O and P (Figure 5.3b,c). This suggested that the side product was Y/Yb-phosphate. The amorphous side product was insoluble in water and it was not possible to eliminate it by washing with water. Its presence was also confirmed with XPS analysis (Figure 4.20). A similar product as in our case was also observed in ref. [138], where Ln_2O_3 in the presence of phosphates transformed into more stable Ln-phosphates. This is also consistent with the report of Tehrani *et al.* [166] where Ln-precursors at moderate aging conditions transformed into Ln-phosphates.

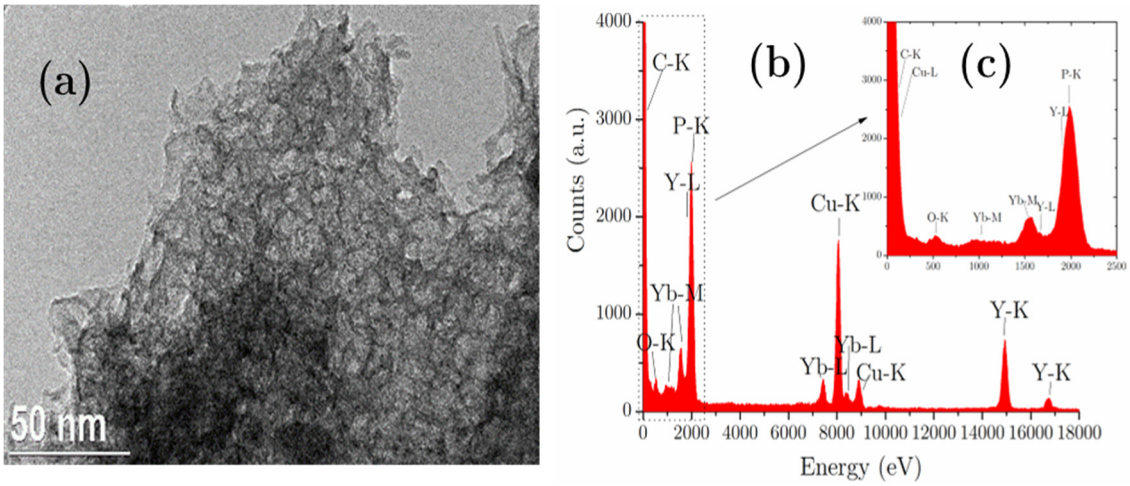


Figure 5.3: TEM image of a solid side product from the aged NaY-TS-XPS sample (a) with the corresponding EDXS spectrum (b). Y-L and P-K overlap (at around 2 keV), which can be seen in an inset in (c). Additional Y-K peaks at around 15 and 17 keV confirm the presence of Y, while the presence of Yb is confirmed by the Yb-M and Yb-L peaks. The Cu and C peaks originate from the TEM supporting grid.

The dissolution process is also *time-dependent* and it slows down as the equilibrium solubility level is approaching [104]. We observed only the increased degree of dissolution of F^- with the increasing the aging time (Figure 4.15). This can be explained by the too short aging times (max. of 2 days). The dissolution process of the UCNPs starts immediately with the dissolution of a small fraction of F^- due to the surface hydrolysis. In the continuation, the dissolution can be promoted with different factors, i.e., the formation

of Ln-phosphates compounds [159]. In our studies at aging times up to 2 h the dissolution rate was low and almost constant (Figure 4.16) but it increased in the time frame of 1–2 days (Figure 4.15).

The effect of surface chemistry on the dissolution of fluoride UCNPs. Theoretical size differences due to the aging of UCNPs, calculated from the fraction of dissolved F^- and assuming a stoichiometric dissolution (Equation (5.2)), were negligible, in the range of ~0.5 nm. This suggests that the observed dissolution of UCNPs is a surface process and thus strongly affected by the surface chemistry. Certain classes of molecules, e.g., chelating agents, can promote the dissolution process by forming stable complexes [68], [104]. One such example is PVP because its pyrrolidone group can coordinate with Ln^{3+} ions [31], [35], [68]. A significant effect of the PVP on the dissolution of α-$NaYF_4$ UCNPs (NaY-R versus NaY-R@PVP) was also observed in our study (Figure 4.15 and Figure 4.16). The dissolution degree of the NaY-R@PVP UCNPs was much more significant in the time period of 2 days than for the NaY-R at the same aging conditions. We propose the following mechanism of the dissolution of UCNPs in the presence of PVP:

$$\begin{aligned} \alpha - NaLnF_4@PVP(s) \overset{PBS}{\Longleftrightarrow} & xNa^+(aq) + 4xF^-(aq) \\ & + xLn^{3+} - PVP\ (aq) + (1-x)NaLnF_4(s) \end{aligned} \tag{5.4}$$

Following this, we decided to protect the direct contact of the UCNPs' surfaces with the aqueous media. PVP-stabilized NaY-R UCNPs were coated with ~7 nm thick silica layer, NaY-R@SiO_2 UCNPs (Figure 4.11). The dissolution of F^- from NaY-R@SiO_2 UCNPs was more than 2-times lower than the dissolution of NaY-R@PVP UCNPs at the same aging conditions (Table 5.1). However, due to the porosity of silica it was impossible to completely prevent the direct contact of solvent molecules with the UCNPs' surfaces.

Therefore, the silica coating should be additionally functionalized with an effective protective layer. However, there are some issues related to the silica coating. As-synthesized β-$NaYF_4$ UCNPs, which are preferred for bioapplications due to their superior optical properties, are hydrophobic. Thus a surface modification is required to disperse them into aqueous media. The most straightforward option is to use a reverse microemulsion method for the direct coating with silica [64]. However, silica-coated UCNPs, prepared with this method, aggregated in water after one day, and the complete elimination of the surfactant (i.e., CTAB) was not possible. Alternatively, one could use a ligand exchange method, where OA at the surface is replaced with PVP [67]. However, this procedure is robust and the remaining excess surfactants result in lower colloidal stability. Moreover, the dissolution of UCNPs is accelerated during the ligand exchange process. For example, during the transfer of the OA-coated NaY-TS UCNPs into aqueous media by the protonation of OA using HCl [149], we detected NaCl as a side product. Here, Cl^- ions originate from HCl and Na^+ ions can only originate from the UCNPs, meaning that some dissolution of the UCNPs occurs during the ligand-exchange. Another option to transfer hydrophobic UCNPs into aqueous media is with amphiphilic coatings, which is discussed in the following Section.

5.2 Effect of Amphiphilic Coatings on the Dissolution of β-$NaYF_4$ UCNPs in Aqueous Media

Amphiphilic coatings are supposed to provide colloidal stability in aqueous media and an efficient protection against the dissolution of UCNPs. UCNPs are first coated with a hydrophobic polymer shell via hydrophobic interactions between alkyl chains of the polymer and the surface ligand (i.e., OA), present at the UCNPs' surface [150]. A hydrophilic polymer, which is bound to the hydrophobic part electrostatically or chemically makes UCNPs hydrophilic. We tested two amphiphilic polymers: TPGS (based on vitamin E) [20] and amphiphilic polymer PMAO cross-linked with BHMT [19]. Both coatings were reported to be suitable for bioapplications [19], [79].

TPGS could be potentially used in drug delivery [78], [79]. Moreover, vitamin E is approved by FDA as a safe pharmaceutical adjuvant used in drug delivery [77]. Therefore the TPGS coating could, beside the colloidal stability of UCNPs in aqueous systems [20], also ensure their biocompatibility. However, our studies showed that TPGS does not prevent the dissolution of UCNPs in PBS. The dissolution analysis of TPGS-coated NaY-TS UCNPs revealed such high fractions of the dissolved F^- (Table 4.5, Table 5.1) that implied on the complete dissolution of the UCNPs in PBS.

We propose the following explanation: TPGS-coated UCNPs, at first, formed stable suspensions in PBS but with time UCNPs aggregated. This suggests that TPGS must have been detached from the UCNPs surfaces, most likely due to the high concentration of phosphates in the PBS. Similar detachment of amphiphilic coating (i.e., PEG-oleate) was reported by Pichaandi *et al.* [18]. Their suspension was stable in water for several weeks as in our case and then UCNPs agglomerated and sedimented in PBS at room temperature. The detachment of the polymer from the UCNPs' surfaces was probably caused by the presence of salts in buffer, to which Ln^{3+} ions show high affinity [172]. Moreover, our results suggest that the phosphates must have expelled, not only TPGS, but also OA from the UCNPs' surfaces, similar to [18]. However, this does not explain why the dissolution (under the same conditions) was more significant for the NaY-TS@TPGS than that of the bare UCNPs (Table 4.5). At least one of the TPGS components must promote the dissolution of UCNPs but the mechanism is not clear.

The issue related to the stability of the coatings in physiological buffers, specifically in PBS, where phosphates can replace for the coating, was addressed by Jiang *et al.* [19]. They proposed cross-linking of the two hydrophobic/amphiphilic/hydrophilic polymers, which form a stable amphiphilic co-polymer coating on the UCNPs' surfaces. As an example we studied PMAO crosslinked with BHMT, which is discussed in the following.

Amphiphilic coating PMAO-BHMT

Because of the dynamic nature of ligands on the surface of UCNPs, they should be cross-linked with another polymer, to form a ligand shell around the UCNPs [174]. This strategy should prevent the detachment of the ligands from the UCNPs' surfaces in water and physiological buffers.

Here we studied the effectiveness of amphiphilic polymer PMAO that intercalates with OA on the surface of UCNPs with its hydrophobic part, while the hydrophilic part (anhydride rings) are subsequently cross-linked with BHMT [19]. During the cross-linking the anhydride rings open, which ensures electrosteric stabilization of UCNPs in aqueous media and further functionalization. Excellent colloidal stability, observed during our study on NaY-TS@PMAO-BHMT UCNPs, was also a consequence of a large fraction of the PMAO-BHMT on the NaY-TS UCNPs' surfaces (Figure 4.25). The efficiency of PMAO-BHMT coating as a protection of UCNPs against dissolution was tested in PBS at

pH = 7.4, at 37 °C for 2 days. Although the coating did not prevent the dissolution completely, it did limit it significantly. The fraction of dissolved F^- was 8-times lower than that of the bare NaY-TS UCNPs. It has to be noted that the same results were obtained in the PBS suspensions with excellent colloidal stability and those with some degree of agglomeration. This indicates that the suppression of the dissolution by the PMAO-BHMT coating is so effective that the reduced free surface in agglomerates does not affect significantly the dissolution degree.

PMAO as a amphiphilic polymer is not known only to provide an excellent colloidal stability, it also provides biocompatibility with additional functionalization, like with PEG [19], [75]. Therefore, we find our studies to be a suitable basis towards the development of biocompatible water-proof coatings based on the PMAO-BHMT.

5.3 Effect of the Dissolution of UCNPs on the Potential Use in Biomedicine

Possible cyto(toxicity)

Studies on the potential leakage of Ln^{3+} or F^- from fluoride-based Ln^{3+} doped UCNPs in aqueous media and their potential cyto(toxicity) in a biological environment have been rarely reported and the latter have not revealed any significant cyto(toxicity) yet [141]–[143], [175]. This is surprising since the cytotoxicity of Ln^{3+} has been generally known [126]. Only few (cyto)toxicological studies of UCNPs pointed out a potential dissolution problem [69], [89], [126], [158], based on which risk assessment studies on exposure and hazard of UCNPs were proposed [126]. It is interesting to note that Yang *et al.* [144] assumed that UCNPs partially decomposed or that were damaged without significant extraction. Toxicological studies of UCNPs were performed and abnormalities were observed, such as delayed embryonic and larvar development [145]. Author assumed that this may be related to the Ln^{3+} binding to the DNA, consequently causing DNA damage.

Other studies using various environmental and chemical sources of F^- demonstrated that in sufficiently large concentrations (around a few mM) F^- represents a cytotoxic threat in different tissues [128], [129]. Many of these cellular events can ultimately lead to death.

In this study we point out the problematics of the dissolution of UCNPs in aqueous media. We would like to emphasize the importance of our finding related to the increased dissolution of UCNPs by the phosphates (i.e., in PBS) [159]. Li *et al.* [138] reported about a transformation of Ln_2O_3 NPs into Ln-phosphates by extraction of the phosphates from the lipid bilayer of lysosomes. This problem was overcome by coating the NPs with phosphates. Sikora *et al.* reported about internalization of Ln^{3+} doped fluoride UCNPs in HeLa cells in the vicinity of the nucleus [176]. Since phosphate groups link nucleoid acids in DNA and RNA, phosphates could be, in the worst scenario, extracted from the DNA and RNA and, consequently, could damage the genetic code. Additional sources of phosphates in cells that could react with Ln^{3+} are adenine-tri-phosphates (ATP), a source of energy [177], and nikotinamid adenine dinukleotid (NAD^+), responsible for the cellular transport of H^+ [177].

Therefore, the dissolution of UCNPs should be limited, not to release F^- or Ln^{3+} ions. As a solution we propose a protective coating based on PMAO-BHMT. The PMAO-BHMT coating almost completely prevents the dissolution of UCNPs, ensures colloidal stability and biocompatibility, when functionalized with, e.g., PEG-amine [19]. Moreover, optical properties of UCNPs are also enhanced after the coating (Figure 4.26).

Optical properties

Optical properties of the UCNPs are sensitive to their surface chemistry and/or crystal field of the Ln^{3+} ions [178], which can be both affected by the dissolution. The effect of the surface chemistry, especially on the surface quenching, is significant in the case of UCNPs due to their large surface-to-volume ratio [12], [13], [14]. We detected the variations in the intensities of all emission peaks and changes in the Yb^{3+} lifetimes between unaged and aged UCNPs. We correlated these changes to the modified surface chemistry as a consequence of the dissolution (Figure 4.20) and to the formation of nonluminescent solid side product (Figure 5.3). The dissolution of fluoride UCNPs influences mainly on increase of the multiphonon deactivation of Yb^{3+} lifetime. Yb^{3+} lifetime decreases with the aging of the UCNPs (Figure 4.19) together with a decrease of the intensity of UC fluorescence (Figure 4.18). The influence of the aging process can be seen in a decrease of the UC fluorescence intensity between 70 and 80 % for all emission bands, compared to the respective unaged sample (Plohl *et al.*, to be submitted). Consequently, the sensibility of the diagnostic methods (like bioimaging), using UCNPs as contrasting agents, would decrease with time. Therefore, UCNPs are not directly applicable for *in vivo* diagnostics.

We conclude that UCNPs should be protected with, for example, PMAO-BHMT coating against the dissolution, not only due to a cytotoxic threat, but also because of the deterioration of their optical properties.

Chapter 6

Conclusions

This thesis covers a study on the dissolution of fluoride UCNPs in aqueous suspensions and their possible protection against the dissolution using amphiphilic coatings. We showed, for the first time, the dissolution of selected binary and ternary fluoride upconverting nanoparticles (UCNPs; LaF_3, GdF_3, $NaYF_4$, all codoped with Yb^{3+} and Tm^{3+}) in aqueous suspensions.

Various parameters affected the dissolution of the UCNPs. The dissolution degree of β-$NaYF_4$ UCNPs was significantly lower in comparison to the α-$NaYF_4$ UCNPs, regardless of the synthesis and aging conditions. This was correlated to the different thermodynamic stabilities of the two crystal modifications, where β-$NaYF_4$ UCNPs with a hexagonal crystal structure are thermodynamically stable at room temperature, whereas α-$NaYF_4$ UCNPs, having a cubic crystal structure, are metastable. Namely, the potential effect of the surface chemistry on the dissolution was excluded, since surface composition for the α-$NaYF_4$ and β-UCNPs was similar when synthesized in nonaqueous media.

The dissolution degree increased exponentially with the decreasing UCNPs sizes and increasing temperature within the aging time of up to two days.

It was found that the stabilizing surface agent, polyvinylpirrolidone (PVP), promoted the dissolution, probably due to its affinity for the complexation with lanthanide (Ln^{3+}) ions. In contrast to this, the silica coating slowed down the dissolution and 2-times lower dissolution degree was detected in comparison to the bare UCNPs at the same aging times.

UCNPs dissolved more significantly in the phosphate buffer saline (PBS) than in the weakly acidic water. The dissolution of UCNPs in water could be explained with surface hydrolysis. On the other hand, the unexpectedly high dissolution degree observed in the PBS was explained by the formation of highly stable and poorly soluble Ln-phosphates compounds. It was suggested that these Ln-phosphates are the driving force for the dissolution in the PBS due to the high affinity of the phosphates from PBS to Ln^{3+} ions. The suggested mechanism was confirmed with P-rich amorphous side products in the aged samples and with the decreasing of the pH during the aging of the suspensions.

Moreover, the dissolution of UCNPs had an influence on the surface chemistry and, consequently on optical properties of the UCNPs. β-$NaYF_4$ UCNPs, aged in PBS, showed significantly lower emission intensities of all emission bands, which can be, in part, attributed to the formation of the nonluminescent side product. However, lower Yb^{3+} lifetimes originate from the changes in the surface chemistry of the UCNPs, caused by their dissolution. Consequently, luminescent lifetime measurements could form a basis for a stability screening method of UCNPs.

Following this, there was a necessity to protect UCNPs with protective coatings. The studied options were amphiphilic coatings, i.e., TPGS and PMAO-BHMT. Surprisingly, UCNPs coated with TPGS dissolved almost completely in PBS. Not only that phosphates

promoted the dissolution, also some of the components of the TPGS must have enhanced the dissolution. Nevertheless, the mechanism is not clear yet. More promising results were obtained with the PMAO cross-linked with BHMT, with which the dissolution of the UCNPs in PBS was significantly decreased. Moreover, the PMAO-BMHT coating ensured colloidal stability not only in water, but also in PBS.

This study demonstrates the problematics of the dissolution of fluoride UCNPs. Consequently, cytotoxicity may originate from the released F^- and Ln^{3+}, or due to the reaction of phosphates with the dissolved Ln^{3+}. In addition to this, the dissolution also limits the diagnostic efficiency of the UCNPs in bioimaging due to the consequent deterioration of their optical properties. The results of this thesis point out the need for a protective coating. As an example we propose the coating based on PMAO-BHMT.

References

[1] H. Dong, S. R. Du, X. Y. Zheng, G. M. Lyu, L. D. Sun, L. D. Li, P. Z. Zhang, C. Zhang, and C. H. Yan, "Lanthanide Nanoparticles: From Design toward Bioimaging and Therapy," *Chem. Rev.*, vol. 115, no. 19, pp. 10725–10815, 2015.

[2] A. Gnach and A. Bednarkiewicz, "Lanthanide-doped up-converting nanoparticles: Merits and challenges," *Nano Today*, vol. 7, no. 6, pp. 532–563, 2012.

[3] H. S. Mader, P. Kele, S. M. Saleh, and O. S. Wolfbeis, "Upconverting luminescent nanoparticles for use in bioconjugation and bioimaging," *Curr. Opin. Chem. Biol.*, vol. 14, no. 5, pp. 582–596, 2010.

[4] J. Shen, L. Zhao, and G. Han, "Lanthanide-doped upconverting luminescent nanoparticle platforms for optical imaging-guided drug delivery and therapy," *Adv. Drug Deliv. Rev.*, vol. 65, no. 5, pp. 744–755, 2013.

[5] M. Lin, Y. Zhao, S. Wang, M. Liu, Z. Duan, Y. Chen, F. Li, F. Xu, and T. Lu, "Recent advances in synthesis and surface modification of lanthanide-doped upconversion nanoparticles for biomedical applications," *Biotechnol. Adv.*, vol. 30, no. 6, pp. 1551–1561, 2012.

[6] C. Cao, W. Qin, and J. Zhang, "Study on up-conversion emissions of Yb^{3+}/Tm^{3+} co-doped GdF_3 and $NaGdF_4$," *Opt. Commun.*, vol. 283, no. 4, pp. 547–550, 2010.

[7] R. Arppe, I. Hyppanen, N. Perälä, R. Peltomaa, M. Kaiser, C. Würth, S. Christ, U. Resch-Genger, M. Schäferling, and T. Soukka, "Quenching of the upconversion luminescence of $NaYF_4:Yb^{3+}$, Er^{3+} and $NaYF_4:Yb^{3+}$, Tm^{3+} nanophosphors by water: the role of the sensitizer Yb^{3+} in non-radiative relaxation," *Nanoscale*, vol. 7, pp. 11746–11757, 2015.

[8] F. Wang and X. Liu, "Recent advances in the chemistry of lanthanide-doped upconversion nanocrystals," *Chem. Soc. Rev.*, vol. 38, no. 4, pp. 976–989, 2009.

[9] C. Renero-Lecuna, R. Martin-Rodriguez, R. Valiente, J. Gonzalez, F. Rodriguez, K. W. Kramer, and H. U. Gudel, "Origin of the high upconversion green luminescence efficiency in β-$NaYF_4$:2%Er^{3+},20%Yb^{3+}," *Chem. Mater.*, vol. 23, no. 15, pp. 3442–3448, 2011.

[10] E. Harju, I. Hyppanen, J. Holsa, J. Kankare, M. Lahtinen, M. Lastusaari, L. Pihlgren, and T. Soukka, "Polymorphism of $NaYF_4$:Yb^{3+}, Er^{3+} up- conversion luminescence materials," *Zeitschrift fuer Krist.*, vol. 1, pp. 381–387, 2011.

[11] F. Wang, Y. Han, C. S. Lim, Y. Lu, J. Wang, J. Xu, H. Chen, C. Zhang, M. Hong, and X. Liu, "Simultaneous phase and size control of upconversion nanocrystals through lanthanide doping," *Nat. L*, vol. 463, pp. 1061–1065, 2010.

[12] J. Zhao, Z. Lu, Y. Yin, C. McRae, J. A. Piper, J. M. Dawes, D. Jin, and E. M.

Goldys, "Upconversion luminescence with tunable lifetime in $NaYF_4$:Yb,Er nanocrystals: role of nanocrystal size.," *Nanoscale*, vol. 5, pp. 944–952, 2013.

[13] F. Wang, J. Wang, and X. Liu, "Direct evidence of a surface quenching effect on size-dependent luminescence of upconversion nanoparticles," *Angew. Chemie - Int. Ed.*, vol. 49, no. 41, pp. 7456–7460, 2010.

[14] J. C. Boyer and F. C. van Veggel, "Absolute quantum yield measurements of colloidal $NaYF_4$: Er^{3+}, Yb^{3+} upconverting nanoparticles," *Nanoscale*, vol. 2, no. 8, pp. 1417–1419, 2010.

[15] S. Wilhelm, M. Kaiser, C. Würth, J. Heiland, C. Carrillo-Carrion, V. Muhr, O. S. Wolfbeis, W. J. Parak, U. Resch-Genger, and T. Hirsch, "Water dispersible upconverting nanoparticles: effects of surface modification on their luminescence and colloidal stability.," *Nanoscale*, vol. 7, no. 4, pp. 1403–1410, 2015.

[16] Q. Zhan, J. Qian, H. Liang, G. Somesfalean, D. Wang, S. He, Z. Zhang, and S. Andersson-Engels, "Using 915 nm laser excited Tm^{3+}/Er^{3+}/Ho^{3+}-doped $NaYbF_4$ upconversion nanoparticles for in vitro and deeper in vivo bioimaging without overheating irradiation," *ACS Nano*, vol. 5, no. 5, pp. 3744–3757, 2011.

[17] A. Beeby, I. M. Clarkson, R. S. Dickins, S. Faulkner, D. Parker, L. Royle, A. S. de Sousa, J. A. G. Williams, and M. Woods, "Non-radiative deactivation of the excited states of europium, terbium and ytterbium complexes by proximate energy-matched OH, NH and CH oscillators: an improved luminescence method for establishing solution hydration states," *J. Chem. Soc. Perkin Trans. 2*, vol. 2, no. 3, pp. 493–503, 1999.

[18] J. Pichaandi, J. C. Boyer, K. R. Delaney, and F. C. J. M. Veggel, "Two-Photon Upconversion Laser (Scanning and Wide-Field) Microscopy Using Ln^{3+}-Doped $NaYF_4$ Upconverting Nanocrystals: A Critical Evaluation of their Performance and Potential in Bioimaging," *J. Phys. Chem. C*, vol. 115, no. 39, pp. 19054–19064, 2011.

[19] G. Jiang, J. Pichaandi, N. J. J. Johnson, R. D. Burke, and F. C. J. M. Van Veggel, "An effective polymer cross-linking strategy to obtain stable dispersions of upconverting $NaYF_4$ nanoparticles in buffers and biological growth media for biolabeling applications," *Langmuir*, vol. 28, no. 6, pp. 3239–3247, 2012.

[20] G. Tian, X. Zheng, X. Zhang, W. Yin, J. Yu, D. Wang, Z. Zhang, X. Yang, Z. Gu, and Y. Zhao, "TPGS-stabilized $NaYbF_4$: Er Upconversion nanoparticles for dual-modal fluorescent/CT imaging and anticancer drug delivery to overcome multi-drug resistance," *Biomaterials*, vol. 40, pp. 107–116, 2015.

[21] K. Prorok, M. Pawlyta, W. Stręk, and A. Bednarkiewicz, "Energy Migration Up-conversion of Tb^{3+} in Yb^{3+} and Nd^{3+} Codoped Active-Core/Active-Shell Colloidal Nanoparticles," *Chem. Mater.*, vol. 28, pp. 2295–2300, 2016.

[22] F. Wang, R. Deng, J. Wang, Q. Wang, Y. Han, H. Zhu, X. Chen, and X. Liu, "Tuning upconversion through energy migration in core-shell nanoparticles.," *Nat. Mater.*, vol. 10, no. 12, pp. 968–973, 2011.

[23] H.-S. Qian and Y. Zhang, "Synthesis of Hexagonal-Phase Core-Shell $NaYF_4$ Nanocrystals with Tunable Upconversion Fluorescence," *Langmuir*, vol. 24, no. 13, pp. 12123–12125, 2008.

[24] F. Vetrone, R. Naccache, V. Mahalingam, C. G. Morgan, and J. A. Capobianco,

"The active-core/active-shell approach: A strategy to enhance the upconversion luminescence in lanthanide-doped nanoparticles," *Adv. Funct. Mater.*, vol. 19, no. 18, pp. 2924–2929, 2009.

[25] G. Chen, T. Y. Ohulchanskyy, S. Liu, W. C. Law, F. Wu, M. T. Swihart, H. Ågren, and P. N. Prasad, "Core/shell $NaGdF_4$:Nd^{3+}/$NaGdF_4$ nanocrystals with efficient near-infrared to near-infrared downconversion photoluminescence for bioimaging applications," *ACS Nano*, vol. 6, no. 4, pp. 2969–2977, 2012.

[26] G.-S. Yi and G.-M. Chow, "Water-Soluble $NaYF_4$:Yb,Tm/$NaYF_4$/Polymer Core/Shell/Shell Nanoparticles with Significant Enhancement of Upconversion Fluorescence," *Chem. Mater.*, vol. 19, no. 3, pp. 341–343, 2007.

[27] D. Wawrzynczyk, M. Nyk, A. Bednarkiewicz, W. Strek, and M. Samoc, "A comparison of morphology, structure and optical properties of ultrasmall, small and core–shell up-converting $NaYF_4$/$NaGdF_4$ nanocrystals co-doped with Tm^{3+} and Yb^{3+} ions," *J. Lumin.*, vol. 133, pp. 138–144, 2013.

[28] D. K. Chatterjee, M. K. Gnanasammandhan, and Y. Zhang, "Small upconverting fluorescent nanoparticles for biomedical applications," *Small*, vol. 6, no. 24, pp. 2781–2795, 2010.

[29] J.-P. Jolivet, M. Henry, J. Livage, and E. Bescher, *Metal oxide chemistry and synthesis*. Chichester, England: John Wiley & Sons, 2000.

[30] H. Fueredi-Milhofer, "Spontaneous precipitation from electrolytic solutions," *Pure Appl. Chem.*, vol. 53, pp. 2041–2055, 1981.

[31] M. Wang, G. Abbineni, A. Clevenger, C. Mao, and S. Xu, "Upconversion nanoparticles: Synthesis, surface modification and biological applications," *Nanomedicine Nanotechnology, Biol. Med.*, vol. 7, no. 6, pp. 710–729, 2011.

[32] G. Zhi, J. Song, B. Mei, and W. Zhou, "Synthesis and characterization of Er^{3+} doped CaF_2 nanoparticles," *J. Alloys Compd.*, vol. 509, no. 37, pp. 9133–9137, 2011.

[33] G. Yi, H. Lu, S. Zhao, Y. Ge, W. Yang, D. Chen, and L.-G. Guo, "Synthesis , characterization, and biological application of size-controlled nanocrystalline $NaYF_4$: Yb, Er phosphors," *Nano Lett.*, vol. 4, no. 11, pp. 2191–2196, 2004.

[34] Y. Wei, F. Lu, X. Zhang, and D. Chen, "Polyol-mediated synthesis and luminescence of lanthanide-doped $NaYF_4$ nanocrystal upconversion phosphors," *J. Alloys Compd.*, vol. 455, pp. 376–384, 2008.

[35] Z. Li and Y. Zhang, "Monodisperse silica-coated polyvinyl-pyrrolidone/$NaYF_4$ nanocrystals with multicolor upconversion fluorescence emission," *Angew. Chemie*, vol. 118, pp. 7896–7899, 2006.

[36] Q. Xu, R., Pang, W, Huo, *Modern inorganic synthetic chemistry*. Amsterdam, Netherlands: Elsevier B.V., 2011.

[37] M. Byrappa, K., Yoshimura, *Handbook of hydrothermal technology: Technology for crystal growth and materials processing*. New York: Noyes Publications, 2001.

[38] O. Gun, "Hydrothermal synthesis and characterization of ethylenediamine-containing molybdenum oxides," 2006.

[39] C. Li, J. Yang, P. Yang, H. Lian, and J. Lin, "Hydrothermal synthesis of lanthanide fluorides LnF_3 (Ln = La to Lu) nano-/microcrystals with multiform structures and morphologies," *Chem. Mater.*, vol. 20, no. 13, pp. 4317–4326, 2008.

[40] W. Shao, R. Hua, W. Zhang, Y. Tian, J. Zhao, L. Na, J. Yu, and Z. Sun, "Hydrothermal synthesis of poly(acrylic acid)-functionalized α-(β-)$NaYF_4$: Yb, Er up-conversion nano-/micro-phosphors," *Powder Technol.*, vol. 237, pp. 326–332, 2013.

[41] X. Yang, X. Dong, J. Wang, and G. Liu, "Glycine-assisted hydrothermal synthesis of single-crystalline LaF_3:Eu^{3+} hexagonal nanoplates," *J. Alloys Compd.*, vol. 487, pp. 298–303, 2009.

[42] T. Jiang, W. Qin, and J. Zhou, "Citric acid-assisted phase controlled synthesis of $NaYF_4$:Yb^{3+},Tm^{3+} crystals and their intense ultraviolet upconversion emissions," *J. Fluor. Chem.*, vol. 156, pp. 177–182, 2013.

[43] C. Wang and X. Cheng, "Controlled hydrothermal growth and tunable luminescence properties of β-$NaYF_4$:Yb^{3+}/Er^{3+} microcrystals," *J. Alloys Compd.*, vol. 617, pp. 807–815, 2014.

[44] M. Ding, D. Chen, S. Yin, Z. Ji, J. Zhong, Y. Ni, C. Lu, and Z. Xu, "Simultaneous morphology manipulation and upconversion luminescence enhancement of -$NaYF_4$:Yb^{3+}/Er^{3+} microcrystals by simply tuning the KF dosage.," *Sci. Rep.*, vol. 5, p. 12745, 2015.

[45] M. Ding, C. Lu, L. Cao, Y. Ni, and Z. Xu, "Controllable synthesis, formation mechanism and upconversion luminescence of β-$NaYF_4$: Yb^{3+}/Er^{3+} microcrystals by hydrothermal process," *CrystEngComm*, vol. 15, no. 41, p. 8366, 2013.

[46] X. Qu, H. K. Yang, J. W. Chung, B. K. Moon, B. C. Choi, J. H. Jeong, and K. H. Kim, "Polyol-mediated solvothermal synthesis and luminescence properties of CeF_3, and CeF_3:Tb^{3+} nanocrystals," *J. Solid State Chem.*, vol. 184, no. 2, pp. 246–251, 2011.

[47] X. Qu, G. Pan, H. K. Yang, Y. Chen, J. W. Chung, B. K. Moon, B. C. Choi, and J. H. Jeong, "Solvothermal synthesis and luminescence properties of $NaYF_4$:Ln^{3+} (Eu^{3+}, Tb^{3+}, Yb^{3+}/Er^{3+}) nano- and microstructures," *Opt. Mater. (Amst).*, vol. 34, no. 7, pp. 1007–1012, 2012.

[48] J. Guo, F. Ma, S. Gu, Y. Shi, and J. Xie, "Solvothermal synthesis and upconversion spectroscopy of monophase hexagonal $NaYF_4$:Yb^{3+}/Er^{3+} nanosized crystallines," *J. Alloys Compd.*, vol. 523, pp. 161–166, 2012.

[49] Y.-W. Zhang, X. Sun, R. Si, L.-P. You, and C.-H. Yan, "Single-crystalline and monodisperse LaF_3 triangular nanoplates from a single-source precursor," *J. Am. Chem. Soc.*, vol. 127, no. 10, pp. 3260–3261, 2005.

[50] J.-C. Boyer, F. Vetrone, L. A. Cuccia, and J. A. Capobianco, "Synthesis of colloidal upconverting $NaYF_4$ nanocrystals doped with Er^{3+},Yb^{3+} and Tm^{3+},Yb^{3+} via thermal decomposition of lanthanide trifluoroacetate precursors," *J. Am. Chem. Soc.*, vol. 128, no. 23, pp. 7444–7445, 2006.

[51] H.-X. Mai, Y.-W. Zhang, R. Si, Z.-G. Yan, L.-D. Sun, L.-P. You, and C.-H. Yan, "High-quality sodium rare-earth fluoride nanocrystals: Controlled synthesis and optical properties," *J. Am. Chem. Soc.*, vol. 128, pp. 6426–6436, 2006.

[52] Z. Li and Y. Zhang, "An efficient and user-friendly method for the synthesis of hexagonal-phase $NaYF_4$:Yb, Er/Tm nanocrystals with controllable shape and upconversion fluorescence," *Nanotechnology*, vol. 19, no. 34, pp. 345606–345610,

2008.

[53] J. D. Suter, N. J. Pekas, M. T. Berry, and P. S. May, "Real-time-monitoring of the synthesis of β-$NaYF_4$: 17% Yb, 3% Er nanocrystals using NIR-to-visible upconversion luminescence," *J. Phys. Chem. C*, vol. 118, pp. 13238–13247, 2014.

[54] M. Haase and H. Schafer, "Upconverting nanoparticles," *Angew. Chemie - Int. Ed.*, vol. 50, no. 26, pp. 5808–5829, 2011.

[55] P. B. May, J. D. Suter, P. S. May, and M. T. Berry, "The dynamics of nanoparticle growth and phase change during synthesis of β-$NaYF_4$," *J. Phys. Chem. C*, vol. 120, no. 17, pp. 9482–9489, 2016.

[56] H. X. Mai, Y. W. Zhang, L.-D. Sun, and C.-H. Yan, "Size- and phase-controlled synthesis of monodisperse $NaYF_4$:Yb,Er nanocrystals from a unique delayed nucleation pathway monitored with upconversion spectroscopy," *J. Phys. Chem. C*, vol. 111, no. 37, pp. 13730–13739, 2007.

[57] C. Li and J. Lin, "Rare earth fluoride nano-/microcrystals: synthesis, surface modification and application," *J. Mater. Chem.*, vol. 20, no. 33, pp. 6831–6847, 2010.

[58] N. T. K. Thanh and L. A. W. Green, "Functionalisation of nanoparticles for biomedical applications," *Nano Today*, vol. 5, no. 3, pp. 213–230, 2010.

[59] D. J. Shaw, *Introduction to colloid & surface chemistry*, 4th Editio. Oxford: Butterworth-Heinemann, 1992.

[60] J. Israelachvili, *Intermolecular & surface forces*, 2nd Editio. London: Academic Press, Harcourt Brace & Company, 1992.

[61] J. A. Lewis, "Colloidal processing of ceramics," *J. Am. Chem. Soc.*, vol. 83, no. 10, pp. 2341–2359, 2000.

[62] W. Stöber, A. Fink, and E. Bohn, "Controlled growth of monodisperse silica spheres in the micron size range," *J. Colloid Interface Sci.*, vol. 26, no. 1, pp. 62–69, 1968.

[63] I. A. M. Ibrahim, A. A. F. Zikry, and M. A. Sharaf, "Preparation of spherical silica nanoparticles: Stober silica," *J. Am. Sci.*, vol. 6, no. 11, pp. 985–989, 2010.

[64] R. Abdul Jalil and Y. Zhang, "Biocompatibility of silica coated $NaYF_4$ upconversion fluorescent nanocrystals," *Biomaterials*, vol. 29, no. 30, pp. 4122–4128, 2008.

[65] Z. Liu, G. Yi, H. Zhang, J. Ding, Y. Zhang, and J. Xue, "Monodisperse silica nanoparticles encapsulating upconversion fluorescent and superparamagnetic nanocrystals.," *Chem. Commun.*, vol. 1, no. 6, pp. 694–696, 2008.

[66] S. Sivakumar, P. R. Diamente, and F. C. J. M. van Veggel, "Silica-coated Ln^{3+}-Doped LaF_3 nanoparticles as robust down- and upconverting biolabels.," *Chem. Eur. J.*, vol. 12, no. 22, pp. 5878–5884, 2006.

[67] N. J. J. Johnson, N. M. Sangeetha, J. C. Boyer, and F. C. J. M. van Veggel, "Facile ligand-exchange with polyvinylpyrrolidone and subsequent silica coating of hydrophobic upconverting β-$NaYF_4$:Yb^{3+}/Er^{3+} nanoparticles," *Nanoscale*, vol. 2, no. 5, pp. 771–777, 2010.

[68] J. Wang, Y. Li, Q. Ge, H. Yao, and Z. Li, "Preparation and luminescence of water soluble poly (N-vinyl-2-pyrrolidone)/ LaF_3: Eu^{3+} nanocrystals," *Appl. Surf. Sci.*, vol. 257, no. 9, pp. 4100–4104, 2011.

[69] D. H. Chavez, K. Juarez-Moreno, and G. A. Hirata, "Aminosilane functionalization

and cytotoxicity effects of upconversion nanoparticles Y_2O_3 and Gd_2O_3 co-doped with $Yb^{3+}$and Er^{3+}," *Nanobiomedicine*, vol. 3, no. 1, pp. 1–7, 2016.

[70] H. Hu, L. Xiong, J. Zhou, F. Li, T. Cao, and C. Huang, "Multimodal-luminescence core-shell nanocomposites for targeted imaging of tumor cells," *Chem. Eur. J.*, vol. 15, no. 14, pp. 3577–3584, 2009.

[71] B. Holmberg, K., Jonnson, B., Kronberg, B., Lindaman, *Surfactants and polymers in aqueous solutions*, 2nd Editio. Chichester, England, 2003.

[72] Y. Liu, K. Ai, J. Liu, Q. Yuan, Y. He, and L. Lu, "A high-performance ytterbium-based nanoparticulate contrast agent for in vivo X-ray computed tomography imaging," *Angew. Chemie - Int. Ed.*, vol. 51, no. 6, pp. 1437–1442, 2012.

[73] J.-W. Yoo, E. Chambers, and S. Mitragotri, "Factors that control the circulation time of nanoparticles in blood: challenges, solutions and future prospects.," *Curr. Pharm. Des.*, vol. 16, no. 21, pp. 2298–2307, 2010.

[74] J. Nam, N. Won, J. Bang, H. Jin, J. Park, S. Jung, S. Jung, Y. Park, and S. Kim, "Surface engineering of inorganic nanoparticles for imaging and therapy," *Adv. Drug Deliv. Rev.*, vol. 65, no. 5, pp. 622–648, 2013.

[75] W. W. Yu, E. Chang, J. C. Falkner, J. Zhang, A. M. Al-Somali, C. M. Sayes, J. Johns, R. Drezek, and V. L. Colvin, "Forming biocompatible and nonaggregated nanocrystal in water using amphiphilic polymers," *J. Am. Chem. Soc.*, vol. 129, no. 10, pp. 2871–2879, 2007.

[76] W. W. Yu, E. Chang, C. M. Sayes, R. Drezek, and V. L. Colvin, "Aqueous dispersion of monodisperse magnetic iron oxide nanocrystals through phase transfer," *Nanotechnology*, vol. 17, no. 17, pp. 4483–4487, 2006.

[77] Z. Zhang, S. Tan, and S. S. Feng, "Vitamin E TPGS as a molecular biomaterial for drug delivery," *Biomaterials*, vol. 33, no. 19, pp. 4889–4906, 2012.

[78] Y. Guo, J. Luo, S. Tan, B. O. Otieno, and Z. Zhang, "The applications of Vitamin E TPGS in drug delivery," *Eur. J. Pharm. Sci.*, vol. 49, no. 2, pp. 175–186, 2013.

[79] L. Mu and P. H. Seow, "Application of TPGS in polymeric nanoparticulate drug delivery system," *Colloids Surfaces B Biointerfaces*, vol. 47, no. 1, pp. 90–97, 2006.

[80] S.-M. Lai, J.-K. Hsiao, H.-P. Yu, C.-W. Lu, C.-C. Huang, M.-J. Shieh, and P.-S. Lai, "Polyethylene glycol-based biocompatible and highly stable superparamagnetic iron oxide nanoclusters for magnetic resonance imaging," *J. Mater. Chem.*, vol. 22, no. 30, pp. 15160–16167, 2012.

[81] X. Yu, M. Li, M. Xie, L. Chen, Y. Li, and Q. Wang, "Dopant-controlled synthesis of water-soluble hexagonal $NaYF_4$ nanorods with efficient upconversion fluorescence for multicolor bioimaging," *Nano Res.*, vol. 3, no. 1, pp. 51–60, 2010.

[82] E. Hemmer, T. Yamano, H. Kishimoto, N. Venkatachalam, H. Hyodo, and K. Soga, "Cytotoxic aspects of gadolinium oxide nanostructures for up-conversion and NIR bioimaging," *Acta Biomater.*, vol. 9, no. 1, pp. 4734–4743, 2013.

[83] S. Wu, G. Han, D. J. Milliron, S. Aloni, V. Altoe, D. V Talapin, B. E. Cohen, and P. J. Schuck, "Non-blinking and photostable upconverted luminescence from single lanthanide- doped nanocrystals," *PNAS*, vol. 106, no. 27, pp. 10917–10921, 2009.

[84] D. K. Chatterjee, A. J. Rufaihah, and Y. Zhang, "Upconversion fluorescence imaging of cells and small animals using lanthanide doped nanocrystals," *Biomaterials*, vol.

29, no. 7, pp. 937–943, 2008.

[85] N. N. Dong, M. Pedroni, F. Piccinelli, G. Conti, A. Sbarbati, J. E. Ramirez-Hernandez, L. M. Maestro, M. C. Iglesias-De La Cruz, F. Sanz-Rodriguez, A. Juarranz, F. Chen, F. Vetrone, J. A. Capobianco, J. G. Sole, M. Bettinelli, D. Jaque, and A. Speghini, "NIR-to-NIR two-photon excited CaF_2:Tm^{3+},Yb^{3+} nanoparticles: Multifunctional nanoprobes for highly penetrating fluorescence bio-imaging," *ACS Nano*, vol. 5, no. 11, pp. 8665–8671, 2011.

[86] Y. Il Park, J. H. Kim, K. T. Lee, K. S. Jeon, H. Bin Na, J. H. Yu, H. M. Kim, N. Lee, S. H. Choi, S. Il Baik, H. Kim, S. P. Park, B. J. Park, Y. W. Kim, S. H. Lee, S. Y. Yoon, I. C. Song, W. K. Moon, Y. D. Suh, and T. Hyeon, "Nonblinking and nonbleaching upconverting nanoparticles as an optical imaging nanoprobe and T1 magnetic resonance imaging contrast agent," *Adv. Mater.*, vol. 21, no. 44, pp. 4467–4471, 2009.

[87] F. Evanics, P. R. Diamente, F. C. J. M. Van Veggel, G. J. Stanisz, and R. S. Prosser, "Water-soluble GdF_3 and GdF_3/LaF_3 nanoparticles s physical characterization and NMR relaxation properties," *Chem. Mater.*, vol. 18, no. 2, pp. 2499–2505, 2006.

[88] H. Xing, W. Bu, Q. Ren, X. Zheng, M. Li, S. Zhang, H. Qu, Z. Wang, Y. Hua, K. Zhao, L. Zhou, W. Peng, and J. Shi, "A $NaYbF_4$: Tm^{3+} nanoprobe for CT and NIR-to-NIR fluorescent bimodal imaging," *Biomaterials*, vol. 33, no. 21, pp. 5384–5393, 2012.

[89] Y. F. Wang, L. D. Sun, J. W. Xiao, W. Feng, J. C. Zhou, J. Shen, and C. H. Yan, "Rare-earth nanoparticles with enhanced upconversion emission and suppressed rare-earth-ion leakage," *Chem. - A Eur. J.*, vol. 18, no. 18, pp. 5558–5564, 2012.

[90] Q. Liu, M. Chen, Y. Sun, G. Chen, T. Yang, Y. Gao, X. Zhang, and F. Li, "Multifunctional rare-earth self-assembled nanosystem for tri-modal upconversion luminescence/fluorescence/positron emission tomography imaging," *Biomaterials*, vol. 32, no. 32, pp. 8243–8253, 2011.

[91] A. Xia, M. Chen, Y. Gao, D. Wu, W. Feng, and F. Li, "Gd^{3+} complex-modified $NaLuF_4$-based upconversion nanophosphors for trimodality imaging of NIR-to-NIR upconversion luminescence, X-Ray computed tomography and magnetic resonance," *Biomaterials*, vol. 33, no. 21, pp. 5394–5405, 2012.

[92] X. Kang, Z. Cheng, C. Li, D. Yang, M. Shang, P. Ma, G. Li, N. Liu, and J. Lin, "Core-shell structured up-conversion luminescent and mesoporous $NaYF_4$:Yb^{3+}/Er^{3+}@$nSiO_2$@$mSiO_2$ nanospheres as carriers for drug delivery," *J. Phys. Chem. C*, vol. 115, no. 32, pp. 15801–15811, 2011.

[93] Y. Yang, Y. Qu, J. Zhao, Q. Zeng, Y. Ran, Q. Zhang, X. Kong, and H. Zhang, "Fabrication of and drug delivery by an upconversion emission nanocomposite with monodisperse LaF_3:Yb,Er core / mesoporous silica shell structure," *Eur. J. Inorg. Chem.*, pp. 5195–5199, 2010.

[94] Y. Dai, P. Ma, Z. Cheng, X. Kang, X. Zhang, Z. Hou, C. Li, D. Yang, X. Zhai, and J. Lin, "Up-conversion cell imaging and pH-induced thermally controlled drug release from $NaYF_4$:Yb^{3+}/Er^{3+}@hydrogel core-shell hybrid microspheres," *ACS Nano*, vol. 6, no. 4, pp. 3327–3338, 2012.

[95] L. Cheng, K. Yang, Y. Li, J. Chen, C. Wang, M. Shao, S. T. Lee, and Z. Liu, "Facile

preparation of multifunctional upconversion nanoprobes for multimodal imaging and dual-targeted photothermal therapy," *Angew. Chemie - Int. Ed.*, vol. 50, no. 32, pp. 7385–7390, 2011.

[96] C. Wang, H. Tao, L. Cheng, and Z. Liu, "Near-infrared light induced in vivo photodynamic therapy of cancer based on upconversion nanoparticles," *Biomaterials*, vol. 32, no. 26, pp. 6145–6154, 2011.

[97] A. Hlaváček, Z. Farka, M. Hübner, V. Horňáková, D. Němeček, R. Niessner, P. Skládal, D. Knopp, and H. H. Gorris, "A competitive upconversion-linked immunosorbent assay (ULISA) for the rapid and sensitive detection of diclofenac," *Anal. Chem.*, vol. 88, no. 11, pp. 6011–6017, 2016.

[98] S. Lahtinen, Q. Wang, and T. Soukka, "Long-lifetime luminescent europium(III) complex as an acceptor in an upconversion resonance energy transfer based homogeneous assay," *Anal. Chem.*, vol. 88, no. 1, pp. 653–658, 2016.

[99] L. Wang, R. Yan, Z. Huo, L. Wang, J. Zeng, J. Bao, X. Wang, Q. Peng, and Y. Li, "Fluorescence resonant energy transfer biosensor based on upconversion-luminescent nanoparticles," *Angew. Chemie - Int. Ed.*, vol. 44, no. 37, pp. 6054–6057, 2005.

[100] Z. Li, Y. Zhang, and S. Jiang, "Multicolor core/shell-structured upconversion fluorescent nanoparticles," *Adv. Mater.*, vol. 20, no. 24, pp. 4765–4769, 2008.

[101] F. Vetrone, R. Naccache, A. Zamarron, A. J. De La Fuente, F. Sanz-Rodriguez, L. M. Maestro, E. M. Rodriguez, D. Jaque, J. G. Sole, and J. A. Capobianco, "Temperature sensing using fluorescent nanothermometers," *ACS Nano*, vol. 4, no. 6, pp. 3254–3258, 2010.

[102] J. P. Hsu and B. T. Liu, "Dissolution of solid particles in liquids: A reaction-diffusion model," *Colloids and Surfaces*, vol. 69, no. 4, pp. 229–238, 1993.

[103] U. Cornell, R.M., Schwertmann, *The iron oxides: Structure, properties, reactions, occurrences and users*, 2th Editio. WILEY-VCH, 2003.

[104] P. Borm, F. C. Klaessig, T. D. Landry, B. Moudgil, J. Pauluhn, K. Thomas, R. Trottier, and S. Wood, "Research strategies for safety evaluation of nanomaterials, Part V: Role of dissolution in biological fate and effects of nanoscale particles," *Toxicol. Sci.*, vol. 90, no. 1, pp. 23–32, 2006.

[105] W. Utembe, K. Potgieter, A. B. Stefaniak, and M. Gulumian, "Dissolution and biodurability: Important parameters needed for risk assessment of nanomaterials.," *Part. Fibre Toxicol.*, vol. 12, no. 1, p. 11, 2015.

[106] S. K. Misra, A. Dybowska, D. Berhanu, S. N. Luoma, and E. Valsami-Jones, "The complexity of nanoparticle dissolution and its importance in nanotoxicological studies," *Sci. Total Environ.*, vol. 438, pp. 225–232, 2012.

[107] D. R. Lide, *CRC Handbook of Chemistry and Physics*, 84th Editi. 2003.

[108] J. Atkins, P., Paula, *Atkins' Physical Chemistry*, 8th Editio. New York: W.H. Freeman and Company.

[109] W. Wu and G. H. Nancollas, "A new understanding of the relationship between solubility and particle size," *J. Solution Chem.*, vol. 27, no. 6, pp. 521–531, 1998.

[110] W. D. Chiang, Y.M.; Kingery, *Physical Ceramics*. New York: John Wiley & Sons, Inc., 1997.

[111] G. Kaptay, "On the size and shape dependence of the solubility of nano-particles in

solutions," *Int. J. Pharm.*, vol. 430, pp. 253–257, 2012.

[112] A. W. Adamson and A. P. Gast, *Physical Chemistry Of Surfaces*, 6th Editio. New York: John Wiley & Sons, Inc., 1997.

[113] S. Kittler, C. Greulich, J. Diendorf, M. Köller, and M. Epple, "Toxicity of silver nanoparticles increases during storage because of slow dissolution under release of silver ions," *Chem. Mater.*, vol. 22, no. 16, pp. 4548–4554, 2010.

[114] S. W. Bian, I. A. Mudunkotuwa, T. Rupasinghe, and V. H. Grassian, "Aggregation and dissolution of 4 nm ZnO nanoparticles in aqueous environments: Influence of pH, ionic strength, size, and adsorption of humic acid," *Langmuir*, vol. 27, no. 10, pp. 6059–6068, 2011.

[115] C. N. Fredd and H. S. Fogler, "The influence of chelating agents on the kinetics of calcite dissolution," *J. Colloid Interface Sci.*, vol. 204, no. 1, pp. 187–197, 1998.

[116] C. Jiang, G. R. Aiken, and H. Hsu-Kim, "Effects of natural organic matter properties on the dissolution kinetics of zinc oxide nanoparticles.," *Environ. Sci. Technol.*, vol. 49, no. 19, pp. 11476–11484, 2015.

[117] S.-L. Loo, W. B. Krantz, X. Hu, A. G. Fane, and T.-T. Lim, "Impact of solution chemistry on the properties and bactericidal activity of silver nanoparticles decorated on superabsorbent cryogels," *J. Colloid Interface Sci.*, vol. 461, pp. 104–113, 2016.

[118] C. Gunawan, W. Y. Teoh, C. P. Marquis, and R. Amal, "Cytotoxic origin of copper(II) oxide nanoparticles : Comparative studies with micron-sized particles, leachate and metal salts," *ACS Nano*, vol. 5, no. 9, pp. 7214–7225, 2011.

[119] J. Liu, D. A. Sonshine, S. Shervani, and R. H. Hurt, "Controlled release of biologically active silver from nanosilver surfaces," *ACS Nano*, vol. 4, no. 11, pp. 6903–6913, 2010.

[120] J. Schmidt and W. Vogelsberger, "Dissolution kinetics of titanium dioxide nanoparticles: The observation of an unusual kinetic size effect," *J. Phys. Chem. B*, vol. 110, no. 9, pp. 3955–3963, 2006.

[121] H. Itoh, H. Hachiya, M. Tsuchiya, Y. Suzuki, and Y. Asano, "Determination of solubility products of rare earth fluorides by fluoride ion-selective electrode," *Bull. Chem. Soc. Jpn.*, vol. 57, no. 6, pp. 1689–1690, 1984.

[122] Y. V. Sokolova and R. N. Cherepanin, "Preparation and examination of the properties of complex scandium fluorides," *Russ. J. Appl. Chem.*, vol. 84, no. 8, pp. 1319–1323, 2011.

[123] D. Wu, X. Wu, Y. Lv, and H. Wang, "Influence of solubility on the particle size of fluorides crystalline precipitated from aqueous solutions," *Mater. Lett.*, vol. 62, pp. 3003–3006, 2008.

[124] T. Mioduski, C. Guminski, and D. Zeng, "IUPAC-NIST Solubility data series. 100. Rare earth metal fluorides in water and aqueous systems. Part 1. Scandium group (Sc, Y, La)," *J. Phys. Chem. Ref. Data*, vol. 43, no. 1, pp. 1–48, 2014.

[125] D. Rai, M. Yui, A. Kitamura, H. Yoshikawa, and A. R. Felmy, "Thermodynamic model for the solubility of NdF_3(cr) in the Na^+-NH_4^+-Nd^{3+}-F^--H_2O system at 25 C," *J. Solution Chem.*, vol. 42, no. 7, pp. 1500–1517, 2013.

[126] A. Gnach, T. Lipinski, A. Bednarkiewicz, J. Rybka, and J. A. Capobianco,

"Upconverting nanoparticles: assessing the toxicity," *Chem. Soc. Rev.*, vol. 44, pp. 1561–1584, 2015.

[127] A. Elsaesser and C. V. Howard, "Toxicology of nanoparticles," *Adv. Drug Deliv. Rev.*, vol. 64, no. 2, pp. 129–137, 2012.

[128] O. Barbier, L. Arreola-Mendoza, and L. M. Del Razo, "Molecular mechanisms of fluoride toxicity," *Chem. Biol. Interact.*, vol. 188, no. 2, pp. 319–333, 2010.

[129] N. I. Agalakova and G. P. Gusev, "Molecular mechanisms of cytotoxicity and apoptosis induced by inorganic fluoride," *ISRN Cell Biol.*, vol. 2012, pp. 1–16, 2012.

[130] European Food Safety Authority, "Scientific Opinion on Dietary Reference Values for fluoride, EFSA Panel on Dietetic Products, Nutrition, and Allergies (NDA)," *EFSA J.*, vol. 11, no. 8, p. 3323, 2013.

[131] M. Zhang, A. Wang, W. He, P. He, B. Xu, T. Xia, X. Chen, and K. Yang, "Effects of fluoride on the expression of NCAM, oxidative stress, and apoptosis in primary cultured hippocampal neurons," *Toxicology*, vol. 236, no. 3, pp. 208–216, 2007.

[132] K. T. Morgan, H. Ni, H. R. Brown, L. Yoon, C. W. J. Qualls, L. M. Crosby, R. Reynolds, B. Gaskill, S. P. Anderson, T. B. Kepler, T. Brainard, N. Liv, M. Easton, C. Merrill, D. Creech, D. Sprenger, G. Conner, P. R. Johnson, T. Fox, M. Sartor, E. Richard, S. Kuruvilla, W. Casey, and G. Benavides, "Application of cDNA microarray technology to in vitro toxicology and the selection of genes for a real-time RT-PCR-based screen for oxidative stress in Hep-G2 cells," *Toxicol. Pathol.*, vol. 30, no. 4, pp. 435–451, 2002.

[133] Q. Gao, Y. J. Liu, and Z. Z. Guan, "Oxidative stress might be a mechanism connected with the decreased α7 nicotinic receptor influenced by high-concentration of fluoride in SH-SY5Y neuroblastoma cells," *Toxicol. Vitr.*, vol. 22, no. 4, pp. 837–843, 2008.

[134] T. Grobner, "Gadolinium - a specific trigger for the development of nephrogenic fibrosing dermopathy and nephrogenic systemic fibrosis?," *Nephrol. Dial. Transplant.*, vol. 21, no. 6, pp. 1104–1108, 2006.

[135] D. R. Broome, "Nephrogenic systemic fibrosis associated with gadolinium based contrast agents: A summary of the medical literature reporting.," *Eur. J. Radiol.*, vol. 66, no. 2, pp. 230–234, May 2008.

[136] L. Feng, H. Xiao, X. He, Z. Li, F. Li, N. Liu, Y. Zhao, Y. Huang, Z. Zhang, and Z. Chai, "Neurotoxicological consequence of long-term exposure to lanthanum," *Toxicol. Lett.*, vol. 165, no. 2, pp. 112–120, Aug. 2006.

[137] H. Xiao, F. Li, Z. Zhang, L. Feng, Z. Li, J. Yang, and Z. Chai, "Distribution of ytterbium-169 in rat brain after intravenous injection.," *Toxicol. Lett.*, vol. 155, no. 2, pp. 247–252, Feb. 2005.

[138] R. Li, Z. Ji, C. H. Chang, D. R. Dunphy, X. Cai, H. Meng, H. Zhang, B. Sun, X. Wang, J. Dong, S. Lin, M. Wang, Y.-P. Liao, C. J. Brinker, A. Nel, and T. Xia, "Surface interactions with compartmentalized cellular phosphates explains rare earth oxide nanoparticle hazard and provides opportunities for safer design," *ACS Nano*, vol. 8, no. 2, pp. 1771–1783, 2014.

[139] P. Zhang, Y. Ma, Z. Zhang, X. He, Z. Guo, R. Tai, Y. Ding, Y. Zhao, and Z. Chai, "Comparative toxicity of nanoparticulate/bulk Yb_2O_3 and $YbCl_3$ to cucumber

(Cucumis sativus).," *Environ. Sci. Technol.*, vol. 46, pp. 1834–1841, 2012.

[140] Y. Ma, X. He, P. Zhang, Z. Zhang, Z. Guo, R. Tai, Z. Xu, L. Zhang, Y. Ding, Y. Zhao, and Z. Chai, "Phytotoxicity and biotransformation of La_2O_3 nanoparticles in a terrestrial plant cucumber (Cucumis sativus).," *Nanotoxicology*, vol. 5, no. 4, pp. 743–753, 2011.

[141] S. Gayathri, O. S. N. Ghosh, A. K. Viswanath, P. Sudhakara, M. J. K. Reddy, and A. M. Shanmugharaj, "Synthesis of YF_3: Yb, Er upconverting nanofluorophores using chitosan and their cytotoxicity in MCF-7 cells," *Int. J. Biol. Macromol.*, vol. 72, pp. 1308–1312, 2015.

[142] J. C. Zhou, Z. L. Yang, W. Dong, R. J. Tang, L. D. Sun, and C. H. Yan, "Bioimaging and toxicity assessments of near-infrared upconversion luminescent $NaYF_4$:Yb, Tm nanocrystals," *Biomaterials*, vol. 32, no. 34, pp. 9059–9067, 2011.

[143] H. Hu, M. Yu, F. Li, Z. Chen, X. Gao, L. Xiong, and C. Huang, "Facile epoxidation strategy for producing amphiphilic up-converting rare-earth nanophosphors as biological labels," *Chem. Mater.*, vol. 20, no. 22, pp. 7003–7009, 2008.

[144] L. Cheng, K. Yang, M. Shao, X. Lu, and Z. Liu, "In vivo pharmacokinetics, long-term biodistribution and toxicology study of functionalized upconversion nanoparticles in mice," *Nanomedicine*, vol. 6, no. 8, pp. 1327–1340, 2011.

[145] K. Wang, J. Ma, M. He, G. Gao, H. Xu, J. Sang, Y. Wang, B. Zhao, and D. Cui, "Toxicity assessments of near-infrared upconversion luminescent LaF_3:Yb,Er in early development of zebrafish embryos," *Theranostics*, vol. 3, no. 4, pp. 258–266, 2013.

[146] L. Xiong, T. Yang, Y. Yang, C. Xu, and F. Li, "Long-term in vivo biodistribution imaging and toxicity of polyacrylic acid-coated upconversion nanophosphors," *Biomaterials*, vol. 31, no. 27, pp. 7078–7085, 2010.

[147] H.-T. Wong, M.-K. Tsang, C.-F. Chan, K.-L. Wong, B. Fei, and J. Hao, "In vitro cell imaging using multifunctional small sized $KGdF_4$:Yb^{3+},Er^{3+} upconverting nanoparticles synthesized by a one-pot solvothermal process," *Nanoscale*, vol. 5, no. 8, pp. 3465–3473, 2013.

[148] C. Li, Z. Quan, J. Yang, P. Yang, and J. Lin, "Highly uniform and monodisperse β-$NaYF_4$: Ln^{3+} (Ln= Eu, Tb, Yb/Er, and Yb/Tm) hexagonal microprism crystals: Hydrothermal synthesis and luminescent properties," *Inorg. Chem.*, vol. 46, no. 16, pp. 6329–6337, 2007.

[149] N. Bogdan, F. Vetrone, G. A. Ozin, and J. A. Capobianco, "Synthesis of ligand-free colloidally stable water dispersible brightly luminescent lanthanide-doped upconverting nanoparticles," *Nano Lett.*, vol. 11, no. 2, pp. 835–840, 2011.

[150] R. Di Corato, A. Quarta, P. Piacenza, A. Ragusa, A. Figuerola, R. Buonsanti, R. Cingolani, L. Manna, and T. Pellegrino, "Water solubilization of hydrophobic nanocrystals by means of poly(maleic anhydride-alt-1-octadecene)," *J. Mater. Chem.*, vol. 18, no. 17, pp. 1991–1996, 2008.

[151] B. K. D. Moulder, J.F., Stickle, W.F., Sobol, P.E., *Handbook of X-ray Photoelectron Spectroscopy*. Minnesota, USA: Physical Electronics USA, Inc., 1995.

[152] M. Ponikvar, V. Stibilj, and B. Žemva, "Daily dietary intake of fluoride by Slovenian Military based on analysis of total fluorine in total diet samples using fluoride ion

selective electrode," *Food Chem.*, vol. 103, no. 2, pp. 369–374, Jan. 2007.

[153] A. Greenwood, N.N., Earnshaw, *Chemistry of the elements*. Pergamon Press, 1984.

[154] G. S. Pawley, "Unit-cell refinement from powder diffraction scans," *J. Appl. Crystallogr.*, vol. 14, pp. 357–361, 1981.

[155] O. Plohl, B. Majaron, M. Ponikvar-Svet, D. Makovec, and D. Lisjak, "Influence of the synthesis parameters on the properties of $NaYF_4$:Yb^{3+},Tm^{3+} nanoparticles," *Acta Chim. Slov.*, vol. 62, pp. 789–795, 2015.

[156] N. Murshid and V. Kitaev, "Role of poly(vinylpyrrolidone) (PVP) and other sterically protecting polymers in selective stabilization of {111} and {100} facets in pentagonally twinned silver nanoparticles," *Chem. Commun.*, vol. 50, no. 10, pp. 1247–1249, 2014.

[157] J. C. Boyer, M. P. Manseau, J. I. Murray, and F. C. J. M. Van Veggel, "Surface modification of upconverting $NaYF_4$ nanoparticles with PEG-phosphate ligands for NIR (800 nm) biolabeling within the biological window," *Langmuir*, vol. 26, no. 2, pp. 1157–1164, 2010.

[158] D. Lisjak, O. Plohl, M. Ponikvar-Svet, and B. Majaron, "Dissolution of upconverting fluoride nanoparticles in aqueous suspensions," *RSC Adv.*, vol. 5, no. 35, pp. 27393–27397, 2015.

[159] D. Lisjak, O. Plohl, J. Vidmar, B. Majaron, and M. Ponikvar-Svet, "Dissolution mechanism of upconverting AYF_4:Yb,Tm (A = Na or K) nanoparticles in aqueous media," *Langmuir*, vol. 32, pp. 8222–8229, 2016.

[160] P. Chandrasekharan, D. Maity, C. X. Yong, K. H. Chuang, J. Ding, and S. S. Feng, "Vitamin E (d-alpha-tocopheryl-co-poly(ethylene glycol) 1000 succinate) micelles-superparamagnetic iron oxide nanoparticles for enhanced thermotherapy and MRI," *Biomaterials*, vol. 32, no. 24, pp. 5663–5672, 2011.

[161] J. E. Roberts, G. Zeng, M. K. Maron, M. Mach, I. Dwebi, and Y. Liu, "Measuring heterogeneous reaction rates with ATR-FTIR spectroscopy to evaluate chemical fates in an atmospheric environment: A physical chemistry and environmental chemistry laboratory experiment," *J. Chem. Educ.*, vol. 96, pp. 733–737, 2016.

[162] Y. Ma, Y. Zheng, K. Liu, G. Tian, Y. Tian, L. Xu, F. Yan, L. Huang, and L. Mei, "Nanoparticles of poly(lactide-co-glycolide)-d-a-tocopheryl polyethylene glycol 1000 succinate random copolymer for cancer treatment," *Nanoscale Res. Lett.*, vol. 5, no. 7, pp. 1161–1169, 2010.

[163] H. Sis and M. Birinci, "Effect of nonionic and ionic surfactants on zeta potential and dispersion properties of carbon black powders," *Colloids Surfaces A Physicochem. Eng. Asp.*, vol. 341, pp. 60–67, 2009.

[164] D. S. Nikam, S. V. Jadhav, V. M. Khot, R. S. Ningthoujam, C. K. Hong, S. S. Mali, and S. H. Pawar, "Colloidal stability of polyethylene glycol functionalized $Co_{0.5}Zn_{0.5}Fe_2O_4$ nanoparticles: Effect of pH, sample and salt concentration for hyperthermia application," *RSC Adv.*, vol. 4, no. 25, pp. 12662–12671, 2014.

[165] J. Wang, B. Su, H. Xing, Y. Yang, and Q. Ren, "Preparation and characterization of mono- and Di-d-α-tocopheryl polyethylene glycol 1000 succinate," *J. Appl. Polym. Sci.*, vol. 119, pp. 3026–3033, 2011.

[166] S. Mastour Tehrani, W. Lin, S. Rosenfeldt, G. Guerin, Y. Lu, Y. Liang, M.

Drechsler, S. Förster, and M. A. Winnik, "Hybrid microgels with confined needle-like lanthanide phosphate nanocrystals," *Chem. Mater.*, vol. 28, pp. 501–510, 2016.

[167] R. E. Thoma, G. M. Hebert, H. Insley, and C. F. Weaver, "Phase equilibria in the system sodium fluoride-yttrium fluoride," *Inorg. Chem.*, vol. 2, no. 5, pp. 1005–1012, 1963.

[168] E. A. Meulenkamp, "Size dependence of the dissolution of ZnO nanoparticles," *J. Phys. Chem. B*, vol. 102, no. 40, pp. 7764–7769, 1998.

[169] T. S. Peretyazhko, Q. Zhang, and V. L. Colvin, "Size-controlled dissolution of silver nanoparticles at neutral and acidic pH conditions: Kinetics and size changes," *Environ. Sci. Technol.*, vol. 48, no. 20, pp. 11954–11961, 2014.

[170] K. J. Laidler, "The development of the Arrhenius equation," *J. Chem. Educ.*, vol. 61, no. 6, pp. 494–498, 1984.

[171] M. Nyk, R. Kumar, T. Y. Ohulchanskyy, E. J. Bergey, and P. N. Prasad, "High contrast in vitro and in vivo photoluminescence bioimaging using near infrared to near infrared up-conversion in Tm^{3+} and Yb^{3+} doped fluoride nanophosphors," *Nano Lett.*, vol. 8, no. 11, pp. 3834–3838, 2008.

[172] L. S. Bingler and R. H. Byrne, "Phosphate complexation of gadolinium(III) in aqueous solution," *Polyhedron*, vol. 8, no. 10, pp. 1315–1320, 1989.

[173] X. Liu and R. H. Byrne, "Rare earth and yttrium phosphate solubilities in aqueous solution," *Geochim. Cosmochim. Acta*, vol. 61, no. 8, pp. 1625–1633, 1997.

[174] S. Basiruddin, A. Saha, N. Pradhan, and N. R. Jana, "Advances in coating chemistry in deriving soluble functional nanoparticle," *J. Phys. Chem. C*, vol. 114, no. 25, pp. 11009–11017, 2010.

[175] J. Li, X. Chang, X. Chen, Z. Gu, F. Zhao, Z. Chai, and Y. Zhao, "Toxicity of inorganic nanomaterials in biomedical imaging," *Biotechnol. Adv.*, vol. 32, no. 4, pp. 727–743, 2014.

[176] B. Sikora, K. Fronc, I. Kamińska, K. Koper, S. Szewczyk, B. Paterczyk, T. Wojciechowski, K. Sobczak, R. Minikayev, W. Paszkowicz, P. Stępień, and D. Elbaum, "Transport of $NaYF_4$:Er^{3+}, Yb^{3+} up-converting nanoparticles into HeLa cells," *Nanotechnology*, vol. 24, no. 23, p. 235702, 2013.

[177] A. W. Czura, "Energy production in a cell." pp. 1–6.

[178] E. V. Samsonova, A. V. Popov, A. S. Vanetsev, K. Keevend, K. Kaldvee, L. Puust, A. E. Baranchikov, A. V. Ryabova, S. G. Fedorenko, V. Kiisk, I. Sildos, J. Kikas, R. Steiner, V. B. Loschenov, and Y. V. Orlovskii, "Fluorescence quenching mechanism for water-dispersible Nd^{3+}:KYF_4 nanoparticles synthesized by microwave-hydrothermal technique," *J. Lumin.*, vol. 169, pp. 722–727, 2016.

Bibliography

Publications Related to the Thesis

Scientific Articles Related to the Thesis

D. Lisjak, O. Plohl, J. Vidmar, B. Majaron, and M. Ponikvar-Svet, "Dissolution mechanism of upconverting AYF_4:Yb,Tm (A = Na or K) nanoparticles in aqueous media," *Langmuir,* vol. 32, no. 32, pp. 8222-8229, 2016.

O. Plohl, B. Majaron, M. Ponikvar-Svet, D. Makovec and D. Lisjak, "Influence of the synthesis parameters on the properties of $NaYF_4$:Yb^{3+},Tm^{3+} nanoparticles," *Acta Chimica Slovenica,* vol. 62, no. 4, pp. 789-795, 2015.

D. Lisjak, O. Plohl, M. Ponikvar-Svet and B. Majaron, "Dissolution of upconverting fluoride nanoparticles in aqueous suspensions," *RSC Advances,* vol. 5, no. 35, pp. 27393-27397, 2015.

O. Plohl, M. Kraft, J. Kovač, B. Belec, M. Ponikvar-Svet, C. Wurth, D. Lisjak and U. Resch-Genger, "Tm^{3+} Luminescence Lifetime as Screening Parameter for the Longterm Stability of Upconversion Nanoparticles and Changes in Surface Chemistry," *submitted*.

Published Scientific Conference Contributions

O. Plohl, D. Lisjak, M. Ponikvar-Svet, S. Kralj, D. Makovec, "Synthesis and functionalization of α-$NaYF_4$ nanoparticles," in *Proceedings: part 1 of the 6th Jožef Stefan International Postgraduate School Students' Conference*, Ljubljana, Slovenia: Jožef Stefan International Postgradute School, 2014.

O. Plohl, D. Lisjak, D. Makovec, M. Drofenik, "Synthesis of LaF_3 nanoparticles," in *Proceedings: of the 5th Jožef Stefan International Postgraduate School Students' Conference*, Ljubljana, Slovenia: Jožef Stefan International Postgradute School, 2013.

Published Scientific Conference Contribution Abstracts

D. Lisjak, O. Plohl, B. Majaron, M. Ponikvar-Svet, "Effect of the composition of aqueous media on the dissolution of upconverting $NaYF_4$:Yb^{3+},Tm^{3+} nanoparticles," in *Conference book of the 1st Conference and Spring School on Properties, Design and Applications of Upconverting Nanomaterials, UPCON 2016*, Wroclaw, Poland: Institute of Low Temperature and Structure Research, Polish Academy of Sciences, 2016.

O. Plohl, M. Ponikvar-Svet, M. Kraft, U. Resch-Genger and D. Lisjak, "Effect of the dissolution of fluoride UCNPs on their optical properties," in *Conference book of the 1st Conference and Spring School on Properties, Design and Applications of Upconverting Nanomaterials, UPCON 2016*, Wroclaw, Poland: Institute of Low Temperature and Structure Research, Polish Academy of Sciences, 2016.

D. Lisjak, O. Plohl, B. Majaron, M. Ponikvar-Svet, "Dissolution kinetics of the upconverting AYF_4:Yb^{3+},Tm^{3+} (A = Na or K) nanoparticles in water," in *Proceedings book of the 2nd International Symposium of Nanoparticles/Nanomaterials and Applications*, Carapica, Portugal, 2016.

O. Plohl, B. Majaron, M. Ponikvar-Svet, D. Makovec and D. Lisjak, "Effect of surface chemistry on dissolution of $NaYF_4$:Yb,Tm upconverting nanoparticles in water," in *9th Young researchers' day*, Ljubljana, Slovenia: Jožef Stefan Institute, 2015.

D. Lisjak, O. Plohl, B. Majaron, M. Ponikvar-Svet, "Influence of chemical composition on the dissolution of AYF4:Yb,Tm (A = Na, K or Li) upconverting nanoparticles in water," in *ImagineNano 2014: bringing together Nanoscience & Nanotechnology*, Bilbao, Spain, 2015.

O. Plohl, M. Ponikvar-Svet, B. Majaron, D. Makovec and D. Lisjak "Effect of coatings on properties of fluorescent $NaYF_4$:Yb^{3+},Tm^{3+} nanoparticles," in *Proceedings of Slovenian Chemical Days*, Ljubljana, Slovenia: Slovensko kemijsko društvo, 2015.

O. Plohl, D. Lisjak, D. Makovec, "Incorporation of oxygen into LaF_3:Yb^{3+},Tm^{3+} and GdF_3:Yb^{3+},Tm^{3+} structures," in *8th Young researchers' day*, Ljubljana, Slovenia: Jožef Stefan Institute, 2014.

O. Plohl, D. Lisjak, M. Ponikvar-Svet, B. Majaron, A. Mertelj and D. Makovec, "Effect of synthesis on properties of β-$NaYF_4$:Yb^{3+},Tm^{3+} nanoparticles," in *Proceedings of Slovenian Chemical Days*, Maribor, Slovenia: Fakulteta za kemijo in kemijsko tehnologijo, 2014.

O. Plohl, D. Lisjak, D. Makovec and M. Drofenik "Hydrothermal synthesis of $NaYF_4$ nanoparticles," in *SLONANO 2013,* Ljubljana, Slovenia: Jožef Stefan Institute, 2013.

O. Plohl, D. Lisjak, D. Makovec and M. Drofenik, " Hydrothermal synthesis of LaF_3 nanoparticles," in *7th Young researchers' day*, Ljubljana, Slovenia: Jožef Stefan Institute, 2013.

O. Plohl, D. Lisjak, D. Makovec and M. Drofenik, "Hydrothermal synthesis of $NaYF_4$ nanoparticles," in *Proceedings of Slovenian Chemical Days*, Maribor, Slovenia: Fakulteta za kemijo in kemijsko tehnologijo, 2013.

Biography

I was born on the 2 September 1988 in Ptuj. After finishing the Gymnasium Franca Miklošiča Ljutomer in 2007 I decided to enroll to the Faculty of Chemistry and Chemical Technology (study programme Chemical Technology) at the University of Maribor. In 2008 I started receiving the Zois scholarship for talented students and as a student I was doing occasional work as a tutor for the younger students at the faculty. I was also involved in research work at the Department of Inorganic Chemistry. In 2010 I attended a summer school in Poznan (Poland, 14 days) in Measurement Science in Chemistry. I graduated in September 2012 with the diploma thesis entitled "Synthesis and characterization of CuNi nanoparticles with silica coating", which was also carried out at the Department of Inorganic Chemistry under the supervision of Asst. Prof. Irena Ban and Prof. Dr. Miha Drofenik. For diploma thesis I received the Henkel Award for the best diploma work. In October 2012 I started working as a young researcher at the Jožef Stefan Institute at the Department for Materials synthesis – K8. At the same time, I enrolled to the Nanosciences and Nanotechnologies postgraduate programme at the Jožef Stefan International Postgraduate School. My work at the department K8 at the Institute was mainly related to the synthesis, characterization and the dissolution study of fluoride upconverting nanoparticles. One part of the research was also possible protection of these nanoparticles from dissolution with different coatings for their potential use in biomedicine. During the PhD period I was also involved in the project COST Action CM1403: *The European upconversion network: From the design of photon-upconverting nanomaterials to (biomedical) application* that enabled my stay in Berlin at the Institute BAM in Germany to perform research work and optical measurements.